Novel image processing tools and techniques in cryo-electron microscopy

Inauguraldissertation
zur
Erlangung der Würde eines Doktors der Philosophie
vorgelegt der
Philosophisch-Naturwissenschaftlichen Fakultät
der Universität Basel

von

NIKHIL BIYANI

aus Indien

BASEL, 2017

Originaldokument gespeichert auf dem Dokumentenserver der Universität Basel
edoc.unibas.ch

Genehmigt von der Philosophisch-Naturwissenschaftlichen Fakultät
auf Antrag von

Prof. Dr. Henning Stahlberg
Prof. Dr. Volker Roth

Basel, 18.04.2017

Prof. Dr. Martin Spiess,
The Dean of Faculty

Dedicated to my mother,
Late Savita Biyani

ACKNOWLEDGMENTS

It is well said that big things cannot be accomplished alone. I, here at CINA, was lucky to have wonderful colleagues. First of all, I would like to express my sincere gratitude to my Ph.D. supervisor *Henning Stahlberg*. His full support to freely express my research interests resulted in a highly productive time. He believed in me, was always supportive and available for discussion. Thanks for giving me interesting projects and nurturing my talent throughout my stay. I would also like to thank my co-supervisor *Volker Roth* for the discussions and guidance.

My other colleagues were no different. I would first like to thank *Sebastian Scherer* who introduced me to CINA, helped to set up everything in the initial stages. We still have our 'once in a while' meetings: thanks for sponsoring them ;). The amazing and easy to understand programming setup developed by him along with *Bryant Gipson* and *Marcel Arheit* helped me to quickly complete targets. *Shirley Müller* critically evaluated the manuscripts I wrote and helped me write better "scientific texts". *Karen Bergmann* was always available to solve the administrative tasks. *Venkata Dandey* helped me to learn the the basics of microscopy, the Friday night movies with him were fun! *Julia Kowal* introduced me to the MloK1, 2D crystals and helped me push the final structures. *Mohamed Chami* helped in getting the images of Bacteriorhodopsin. I would also like to thank *Kenneth Goldie*, *Ariane Fecteau-LeFebvre* and *Daniel Caujolle-Bert* for maintaining the microscopes and the facilities. Me and *Kushal Sejwal* had great discussions not only about science but also related to the latest tech-news. *Mikhail Kudrashyev* (or Misha) gave me scientific insights as well as allowed me to live in his apartment after he went to Frankfurt. *Daniel Castano-Diez* was kind enough to give me advice, read my drafts whenever I approached him. I got insightful details on whatever I asked by the talented Mr. *Robert McLeod* and *Eric van Genderen*. *Max Clabbers* listened to all the crap I said ;). You are a champion! *Ricardo Righetto* answered all my EM related questions, helped me with the manuscripts and other software related questions. I would like to thank *Raphael Küng*, *Stefan Albiez*, *Inayatulla Mohammed*, *Ricardo Adaixo*, *Lena Muckenfuss*, *Jing Wang*, *Sergey Nazarov*, *Nicholas Taylor*, *Thorsten Blum* for using the Focus software even when it used to always crash! I would also like to thank *Jan Pieter Abrahams*, *Philippe Ringler* and *Thomas Braun* for the discussions.

The IT support at D-BBSE was exceptional and made my life easier. *Christian* helped me to set up and maintain my Redhat Linux machine. *Martin* was always available for any demand I had including cables, computers for workshop, setting up video and sound system during workshop. *Kenneth* helped to setup the macOS servers, *John* helped in maintenance and to fix network issues.

I would also like to thank my family especially my father, *Suresh Biyani* and my elder brother *Neeraj Biyani* for completely supporting me to pursue my dreams. My stay in Switzerland would not have been the same without the lovely friends.

Lastly, I would like to thank my wife *Shama*: You are a wonderful women, I can't think what I would have been without you!

TABLE OF CONTENTS

Abbreviations

2D	two-dimensional
3D	three-dimensional
aa	amino acid
AFM	atomic force microscopy
C12E8	polyoxyethylene(8)-dodecyl ether
C8E4	polyoxyethylene(4)-octyl ether
CCD	charge coupled device
CHAPS	3-[(3-cholamidopropyl) dimethyl-ammonio]-1-propanesulfonate
CMOS	complementary metal-oxide semiconductor
CMCs	critical micelle concentrations
CNBD	cyclic nucleotide binding domain
CPU	central processing unit
cryo-EM	cryo-electron microscopy
CTF	contrast transfer function
DDM	n-dodecyl-β-D-maltopyranoside
DED	direct electron detector
DFT	discrete Fourier transform
DHPC	1,2-diheptanoyl-sn-glycero-3-phosphocholine
DM	n-decyl-β-D-maltopyranoside
DQE	detective quantum efficiency
EM	electron microscopy
EMDB	electron microscopy data bank
FEG	field emission gun
FFT	fast Fourier transform
FOM	figure-of-merit
FT	Fourier transformation
GPU	graphical processing unit
GUI	graphical user interface
HTG	n-heptyl-β-D-thioglucopyranoside
LDAO	N,N-dimethyl-dodecylamine N-oxide
LMNG	lauryl maltose neopentyl glycol
LPR	lipid-to-protein (w:w) ratio
MRC	MRC file format
NM	n-nonyl-β-D-maltopyranoside
NMR	nuclear magnetic resonance

OG	n-octyl-β-D-glucopyranoside
OTG	n-octyl-β-D-thioglucopyranoside
PCO	projective constraints optimization
PDB	prtein data bank
SNR	signal-to-noise ratio
TEM	transmission electron microscopy
TMD	transmembrane domains
TX100	Triton X-100
VSD	voltage sensor domain

List of Tables

List of Figures

PART I

INTRODUCTION

CHAPTER 1

INTRODUCTION TO IMAGE PROCESSING IN CRYO-EM

1.1 Introduction

Structural biology involves determination of the three-dimensional arrangement of biological structures, mainly proteins and nucleic acids, and how changes in this arrangement change their functionality [Banaszak, 2000]. Our human eyes are capable of, at best, identifying millimeter sized objects, while the biological entities are often much smaller than that: Human cells range from millimeters to micrometers; structures such as membranes, vesicles, viruses are micrometer to nanometer sized. The biological functionality of these structures can only be determined by knowing the Angstrom sized atomic details in them. Consequently, techniques such as light microscopy, scanning electron microscopy, transmission electron microscopy, X-ray crystallography and NMR spectroscopy have been developed that help in resolving these three dimensional structures (Figure 1.1).

In X-ray crystallography, diffraction patterns of two-dimensional or three-dimensional crystals of protein are recorded using X-rays [Smyth and Martin, 2000]. Crystallization of proteins is rather difficult and can take several years to produce a good preparation [Terwilliger et al., 2009]. Although X-ray crystallography achieves atomic resolution, the quality of final reconstruction highly depends on the quality of crystals and it is difficult to reconstruct proteins that do not form well ordered crystals. NMR spectroscopy uses strong magnetic field probed with radio waves to determine the distances between nearby atoms [Ilari and Savino, 2008]. Typically, as larger proteins have overlapping spectra, NMR Spectroscopy can be used to determine the atomic locations in small proteins. Recent studies show that with some tricks, large structures can also be solved by NMR spectroscopy [Quinn and Polenova, 2017]. In transmission electron microscopy, electron density images are produced by interaction of an electron beam that passes through the ultra-thin target specimen [Frank, 2006]. Transmission electron microscopy can be used to study both large structures like cellular organelles or large macromolecular complexes and relatively small objects like membrane proteins. It also requires small amounts of specimen, which is an advantage in comparison to both crystallography and NMR spectroscopy. Cryo-electron microscopy (cryo-EM) is a branch of transmission electron microscopy that uses biological samples at cryogenic temperatures [Dubochet, 2012; Dubochet and McDowall, 1981]. Cryo-EM provides a stable environment to the specimen thus allowing more electron dose to pass through before damaging the specimen, the phenomenon called as radiation damage. Once the atomic resolution details are resolved, they can be matched to the corresponding atoms using software packages [Adams et al., 2010; Emsley et al., 2010] to generate the atomic model of the desired structure.

This work is focused on cryo-EM: the background of image processing is discussed in section 1.2, followed by the techniques to obtain a three dimensional reconstruction in section 1.3. The recent advancements that lead to the boost of high resolution structure determination using cryo-EM is discussed in section 1.4. Finally the chapter is concluded by the discussion of aims and scope of this thesis in section 1.5.

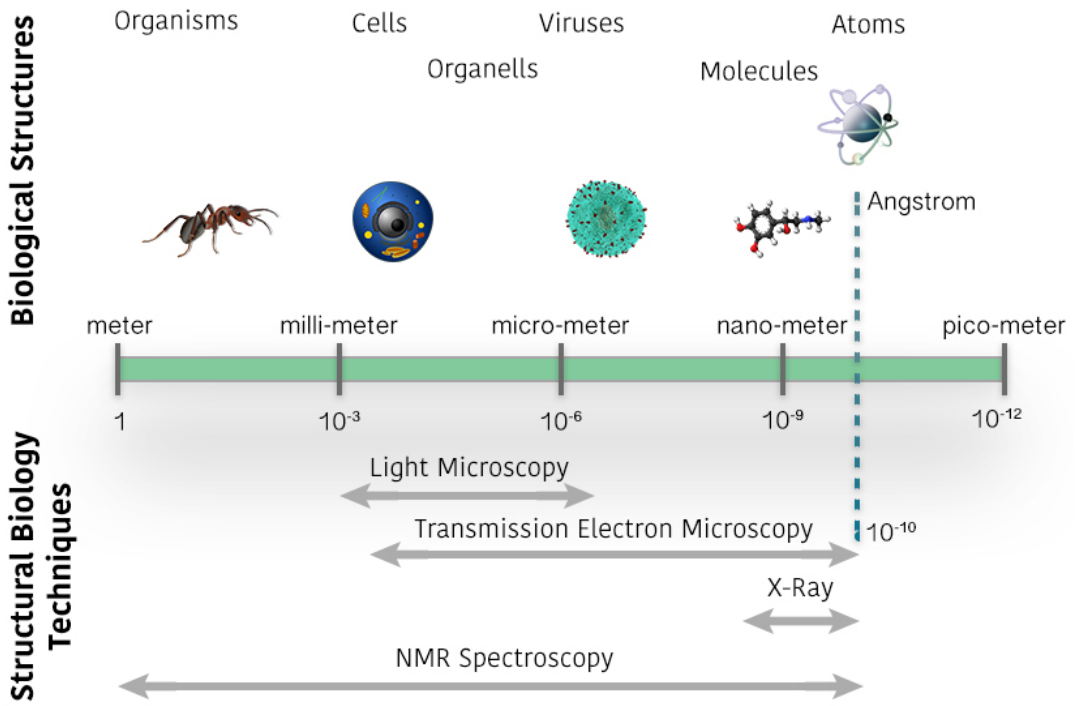

FIGURE 1.1. **Techniques in structural biology and their application range:** Techniques involved in structural biology aims at identifying sub millimeter structural details of biological entities.

1.2 Background

Processing cryo-EM images is one of the most challenging problems in image processing and deals with issues such as low signal-to-noise ratio and contrast transfer function. To understand these issues we first describe the process involved in the image formation in section 1.2.1, followed by the explanation of contrast transfer function and the role of defocus in section 1.2.2. Furthermore, the common characteristics of such images are discussed in section 1.2.3.

1.2.1 Image formation in TEM

The incident beam of electrons interacts with the sample in different ways. Of these the ones that are important for the image formation in TEM include: (i) electrons that pass through the sample without any interaction, known as unscattered beam, (ii) electrons that scatter elastically and get transmitted through the sample with its energy intact, or (iii) electrons that scatter inelastically transferring some energy to the interacted atoms. The resultant transmitted electrons are focused by the objective lens and imaged on the image plane. It is the interference of the unscattered electrons and the elastically scattered electrons passed through the sample that produces contrast

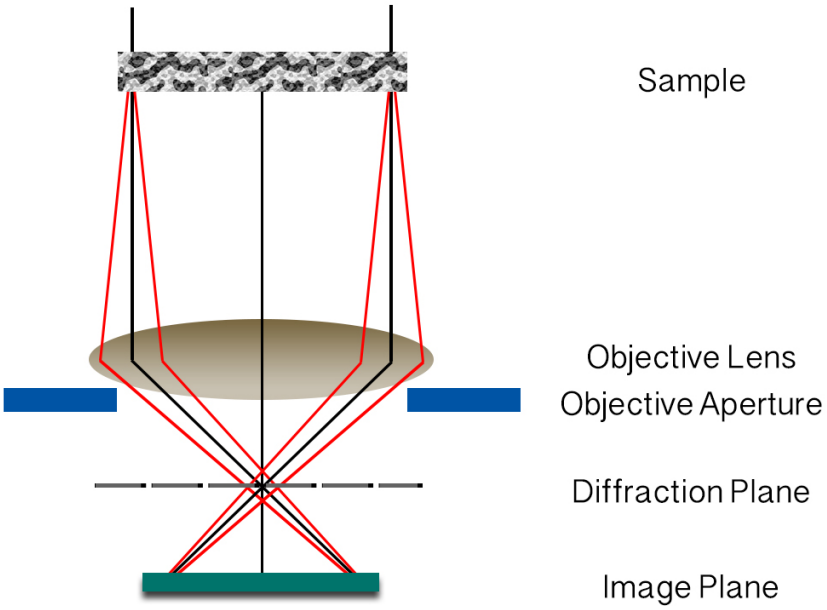

FIGURE 1.2. **Image formation in TEM:** Image formation is based on the interference of elastically scattered and transmitted electron beam (shown in red) with the unscattered electron beam (shown in black) at the image plane.

in the image (Figure 1.2). The inelastically scattered electrons contribute to the noise in the images [Frank, 2006; Rose, 2008].

Electrons that interact with the sample are deflected from their original path. The aperture of the objective lens can be adjusted such that the electrons with greater deflection are avoided from the interference and thus improving the contrast. However, the highly deflected electrons generates high resolution information such as precise atomic arrangement details. Therefore, there is a trade-off between the choice of high resolution and contrast; to obtain high resolution details one needs to sacrifice the contrast in the images.

1.2.2 Contrast transfer function and defocus

The electrons transmitted after interaction with the sample are focused on the image plane. The detector at the image plane is only able to detect the resultant of amplitudes after constructive or destructive interference. Consequently, the contrast at the image plane is modulated by the phase difference that the scattered electrons have with the unscattered electrons [Frank, 2006; Wade, 1992]. This contrast transfer can be positive (in the case of constructive interference) as well as negative (in the case of destructive interference) ranging between [-1, 1]. This effects each pixel in real space to be multiplied by a point spread function. In Fourier space, where the frequencies have a contrast transfer of zero leads to loss of data; the frequencies with negative contrast leads

to the condition where black pixels appear white and the white pixels appear black. This effect can also be visualized as the application of a complicated band-pass filter to the original data. For a two-dimensional case, this phenomenon leads to a concentric circular patters called as Thon rings [Thon, 1966].

Mathematically, in Fourier space the contrast transfer function (CTF) can be modeled by the following equation:

$$CTF(k) = A * cos(\Phi(k)) - \sqrt{1 - A^2} * sin(\Phi(k)) \tag{1.1}$$

where A is the amplitude contrast fraction and $\Phi(k)$ is given by following equation:

$$\Phi(k) = -z\lambda k^2/2 + C_s\lambda^3 k^4/4 \tag{1.2}$$

Here, k is the spatial frequency, λ is the relativistic wavelength of the electron wave, z is the defocus of the objective lens (using the convention that underfocus is positive and overfocus is negative), and C_s is the spherical aberration of the objective lens. Plots representing this equation for different defocus values is shown in Figure 1.3.

As stated in equation 1.1, CTF depends on the defocus of the objective lens. Figure 1.3 represents the CTF curves at low defocus (-100nm), mid-range defocus (-1000nm) and high defocus (-5000nm). It can be noted that: (i) at high absolute values of defocus, the number of zero crossing increase, but the contrast at the low frequencies is high; (ii) at low absolute values of defocus, the number of zero crossings decrease, but the contrast at the low frequencies is low. Thus an image at low defocus provides high resolution details such as atomic arrangement and an image at high defocus provides low resolution features such as the overall shape and size of the target structure. Consequently, one needs to vary the defocus in a set of images collected to see both the low and high resolution details.

1.2.3 Characteristics of a cryo-EM image

Cryo-EM images (or micrographs) are projection images that represent electron density of the recorded specimen in two-dimensions. Depending on the technique used these images can be constituted of projection of different views of the sample (single particle reconstruction, helical image reconstruction), contain projection of a regular arrangement of the proteins (2D electron crystallography) or depict a projection of a part of a cell (electron tomography). The goal is usually to combine these images and generate a three-dimensional reconstruction of the target object, therefore, different views of the specimen need to be captured and the method that acquires this depends on the cryo-EM technique employed. Cryo-EM images are also modulated by contrast transfer function (CTF) as explained in section 1.2.2.

Cryo-EM images are noisy, i.e., the signal-to-noise ratio (SNR) in cryo-EM images is relatively low. One of the major reasons being the limited electron dose; biological samples are radiation sensitive and more dose leads to the so called radiation damage that destroys the features of the

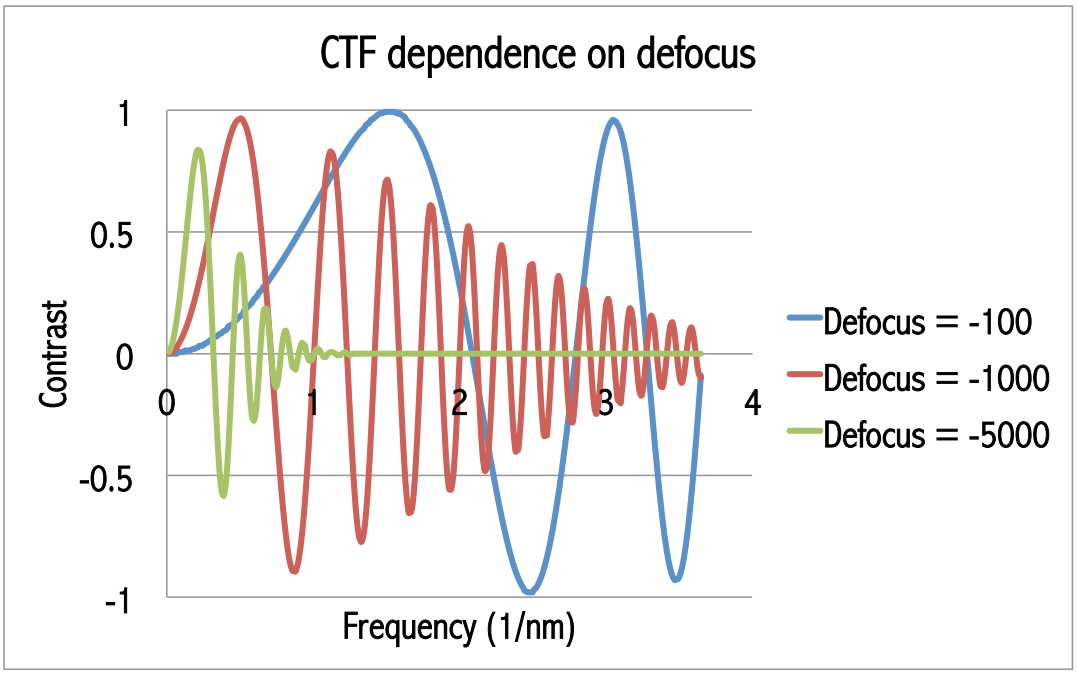

FIGURE 1.3. **Dependence of CTF on the defocus:** CTF depends on the defocus of the objective lens as stated in equation 1.1. Various CTF curves plotted at defocus values of -100 nm, -1000 nm and -5000 nm are provided in this figure. The values are calculated with $\lambda = 1.9866pm$, $c_s = 2$. Higher absolute defocus value leads to higher contrast in the low frequency region simulatneously diminishing it in the high frequency region. Similarly, the low absolute defocus value leads to lower constast in the low resolution region, but improves the contrast in the high frequency region.

sample. Although using samples at cryogenic temperatures adds a protective layer, the SNR is still quite low and needs further improvement. Thus, any technique in cryo-EM aims at employing methods that increase the signal in the images, discussed in detail in section 1.3.

1.3 Techniques for reconstruction

Techniques employed in cryo-EM depend on the type of biological sample and resolution target. In general, all of these techniques deal with solving three major challenges: (i) generation of three-dimensional reconstruction using two-dimensional projection images, (ii) improvement of the signal in the images and (iii) implementation of CTF correction schemes. A comparison of the requirements of the various techniques is done in Table 1.1 and are briefly described in following sections.

1.3.1 Single particle reconstruction

Single particle reconstruction relies on combining many particles that cover the whole orientation space (or views) of the target object [Frank, 1975]. The sample is placed on the grid embedded in vitrified ice. The placed sample should have: (i) all different views of the object; (ii) limited number of conformational changes. Grids are then imaged using TEM, making sure that the images contain many particles associated with each view. The number of particles required depends on the noise present in them: more noise would mean that more particles are required. In case there are multiple conformations, each of these should have sufficient views as well. If the target object is symmetric, for example a virus, then the number of views required is reduced depending of the order of symmetry.

The image processing in single particle reconstruction begins with detecting the locations of the particles in the images, also known as "particle picking". The defocus for these particles is calculated and followed by CTF correction. The particles are then grouped depending on the view they represent, commonly known as "2D classification". All particles in a group are aligned to each other and all these aligned particles are averaged to produce so called "class averages". With averaging the randomly distributed noise reduces and the signal intensifies. A three-dimensional model, or "initial model", is produced using these class averages with an initial guess of the Euler angles that describe their orientation in three-dimensions. Projections of the initial model are then used to iteratively correct the assigned Euler angles improving the model in each iteration. The stable solution after the Euler angles stop changing over iterations, provides the final reconstruction [Doerr, 2015].

The popularity of single-particle reconstructions have increased in the last decade owing to an easier sample preparation and recent developments such as maximum-likelihood [Lyumkis et al., 2013; Scheres et al., 2005; Sigworth, 1998] and Bayesian methods [Jaitly et al., 2010; Scheres, 2012] for reconstruction. Nearly, 77% of the maps deposited in EMDB involve single particle reconstructions (Figure 1.4). Atomic resolution beyond 2Å has been reached by using this technique [Merk et al., 2016].

1.3.2 Helical reconstruction

Some biological structures, such as filaments and microtubules, occur with sub-units forming a helical arrangement. Multiple views can be found in a single image and thus requires relatively fewer images for a high-resolution reconstruction. The helical symmetry of the particles allows to exploit the Fourier-Bessel formalism for the three-dimensional reconstruction [Lepault, 1985]. The single-particle based approach for helical reconstruction [Egelman, 2007] starts with segmenting a helix into single-particles followed by CTF correction, alignment of particles and initial model generation as in the single-particle reconstruction. An additional step to apply the helical symmetry to the obtained three-dimensional model is employed. Determination of the helical symmetry is a tricky process that involves optimization of parameters such as rotation angle

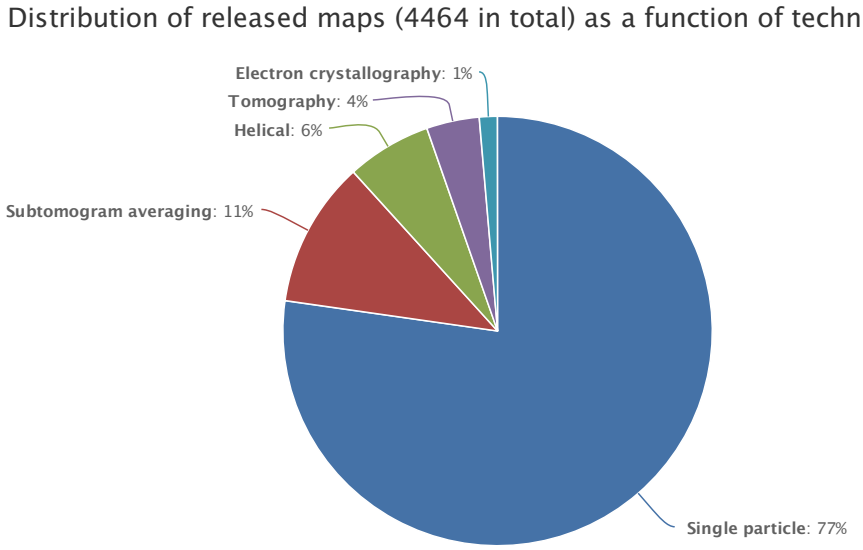

FIGURE 1.4. **The amount of structures as a function of the technique used:** The number of structures deposited in the central Electron Microscopy Data Bank (EMDB) show that single-particle has been used the most, followed by subtomogram averaging and helical image reconstruction. (Source: https://www.ebi.ac.uk/pdbe/emdb/ Accessed on: January 26, 2017)

and the helical rise. With correct values of the helical symmetry parameters very high resolution structures can be obtained using this technique.

1.3.3 2D electron crystallography

Regular thin sheet like arrangements, called 2D crystals, are used for reconstruction in 2D electron crystallography (also referred as 2D crystallography). Some membrane proteins, such as purple membrane [Henderson et al., 1986], naturally occur as 2D crystals. Other proteins can be arranged in this form by solublizing them in detergent and lipid with a particular lipid-to-protein ratio [Sonoda et al., 2011], commonly known as 2D crystallization. The data collection involves imaging the crystal in non-tilted and tilted positions.

The processing uses the fact that the imaged object is present in a regular arrangement and sharp diffraction spots are observed in the Fourier space. The first step to the processing is calculation of the Fourier transform of each image. This is followed by lattice and defocus determination. The tilt geometry can be determined using the lattice parameters and the defocus gradient. If there are crystal distortions, they can be corrected using the unbending procedure [Henderson et al., 1986]. The CTF is corrected and the final unit cell of the crystal, known as final map, is produced [Arheit et al., 2013]. Once the final map is calculated from all the

images, they can be merged using the tilt geometries to produce a first three-dimensional reconstruction [Gipson et al., 2007a]. The tilt geometries can later be iteratively refined using a low resolution model of the current reconstruction. The new geometry improves the reconstruction. This technique is discussed in detail in Chapter 2.

1.3.4 Electron tomography and sub-tomogram averaging

In electron tomography, the entities imaged are structures embedded in the cell which provides them a native environment. The three-dimensional information is encoded by distributing the electron dose over multiple tilt angles of the same area of sample. One such collection of images is called a tomogram. The tomogram can be used to obtain low resolution information of the constituents in the imaged part of cell. High-resolution reconstructions of particular parts of the tomogram can be obtained by imaging and combining many tomograms that contain the target structure. This procedure is known as sub-tomogram averaging and involves alignment and averaging of the target regions in the cell [Förster and Hegerl, 2007]. Recent works have attained high resolution maps by using sub-tomogram averaging [Schur et al., 2016].

1.4 Resolution revolution

The number of structures solved using electron microscopy have exponentially increased in the last decade. This is so called “Resolution Revolution” in cryo-EM [Kühlbrandt, 2014a,b; Veesler et al., 2013]. This change has been made possible by advancements in hardware, such as direct electron detectors, coupled with algorithmic improvements in image processing. These advancements are briefly discussed in the sections below.

1.4.1 Direct electron detectors

Traditionally, the images were acquired either using photographic films or using charge-coupled device (CCD) cameras. The process using photographic films produced high resolution data, but at the cost that it was slow and could not be automated as the film had to be first developed followed by digitization using scanning. CCDs, on the other hand, provided a way to conveniently automate the imaging process. CCDs convert the incoming electrons to light using a scintillator. This intermediate conversion to light yielded images that had very low signal to noise ratio and thus was a bottleneck in attaining high resolution [Faruqi and Subramaniam, 2000].

A new type of complementary metal-oxide-semiconductor (CMOS) based detectors were introduced in the last decade. These detectors being radiation hardened could directly sense the electrons, helping to improve the signal-to-noise ratio by many folds [Ruskin et al., 2013]. Along with the better SNR, these detectors offer high read-out speed. This allows to record a sequence of images (called as movies or image stacks or stacks) in one exposure . These individual images in the stacks helps (i) to reduce motion effects [Glaeser et al., 2011], and (ii) to carefully adjust

Single particle	Helical	2D crystallography	Tomography
Target Objects Limited number of conformations existing in multiple identical copies	**Target Objects** Structures that occur in helical shape	**Target Objects** Structures that can be arranged as 2D crystals	**Target Objects** Large cellular complexes that are to be studied in-situ.
Examples Complexes, Viruses	**Examples** Filaments, Microtubules	**Examples** Membrane proteins	**Examples** Organelles
3D information Images that capture different orientations of the target object	**3D information** Helical symmetry and different orientations of the target object	**3D information** Images of tilted and non-titled crystals	**3D information** Tilt series of the sample
Resolution Depends on orientations available, number of particles, homogeneity Range: 1.8-15Å	**Resolution** Depends on order of helical arrangement Range: 3.3-10Å	**Resolution** Depends on crystal quality Range: 1.9-25Å	**Resolution** Depends on number of tomograms that can be merged together Range: 3.9-50Å

TABLE 1.1. **Comparison of reconstruction methods in cryo-EM:** Techniques in cryo-EM depend on the type of the object under consideration and the resolution targeted. This table gives some target objects with examples for each of these techniques along with how data is collected and the typical resolution range that can be achieved.

the dose such that both high resolution and low resolution features are visible in the final image [Zhang, 2016]. This relies on the concept that the initial images in the stack had less radiation damage and in turn more high resolution details [Baker et al., 2010].

1.4.2 Algorithmic improvements

Algorithms that utilize the advancements in hardware have been simultaneously developed. These include generic drift correction algorithms such as Zorro [McLeod et al., 2016], MotionCorr [Li et al., 2013], MotionCor2 [Zheng et al., 2016] and Unblur [Grant and Grigorieff, 2015]. Drift correction involves reduction in the effects of drift that might have emerged while recording due to factors such as beam induced sample movements. The drift correction can either be performed on the individual images (or frames) using frame-level translations [Li et al., 2013] or parts of the images can be drift corrected separately. These parts can be as small as particles [Scheres, 2014], or can be large regions of the image [Zheng et al., 2016]. Apart from that, there

have been advancements in the single particle reconstruction technique which include multi-reference alignment [Lyumkis et al., 2013; Scheres, 2012] and Bayesian approaches [Scheres, 2012]. Software packages that use GPUs to speed-up the processing have also been developed [Kimanius et al., 2016; Zhang, 2016].

1.5 Aim and scope of thesis

The aim of this thesis is to contribute towards the development of tools and techniques that assist and improve the image processing tasks in cryo-EM. Specifically, these improvements can be divided in two categories: (i) development of tools that assist in image processing with new direct-electron detectors (discussed in Part II), and (ii) algorithmic improvements to achieve high-resolution in 2D electron crystallography (discussed in Part III).

The software resources in cryo-EM have to deal with stacks of hundreds of "8k" images. To process this amount of data, a fast and efficient software tool is required. For this, a performance oriented C++ toolkit named *EMKIT* was developed (discussed in Chapter 3). This toolkit can be used to accomplish fast basic operations using in-built classes and methods. Furthermore, complex features can be conveniently built using the toolkit.

After the advent of DEDs the amount of data that comes out of the microscopes has drastically increased. Today, there exists a handful of software which can automate the data collection process on microscopes. Target spots on the grid are selected and the microscope automatically records images on these spots. With some tricks the microscopes can now yield a new image every minute. This allows obtaining more data in the limited microscope-time. But it is quite important that this data can be processed in real time to get an idea if the recording is running as expected. *Focus* was designed to accomplish this task in a user friendly environment (further details in Chapter 4).

One of the classical methods in electron microscopy is 2D electron crystallography (detailed in Chapter 2). Obtaining highly-ordered 2D crystals is difficult and time-consuming. However, 2D crystals diffracting to only 10-12Å can be prepared relatively conveniently in most cases. There is a need to develop image processing algorithms allowing to generate high resolution 3D structure from cryo-EM images of badly ordered crystals. Apart from that, while recording tilted 2D crystals, there is a limitation to the possible extent of tilt. This limitation arises due to considerations such as sample movement, increase in thickness of sample with tilt and varying defocus. The achievable tilt angle is typically 60°. This would mean that in 3D Fourier space, the slices with tilt angle beyond this would be missing. This region in Fourier space turns out to be conical in shape and hence this problem in 2D electron crystallography is known as the "problem of missing cone". In real space, this makes the densities look elongated in the vertical direction. Apart from the missing cone, data can also be missing in other regions, depending on the tilt sampling.

New methods have been developed which can tackle the problems stated above to some extent including (i) movie-mode unbending, which performs frame-wise unbending in the recorded movie frames (Chapter 5); (ii) refinement over sub-tiles of the frames in order to locally refine the crystal tilt geometry within different tile locations on the images (Chapter 5); (iii) a projective constraint optimisation refinement for approximating the Fourier data in the region of missing cone (Chapter 6). All of these methods were applied to MloK1 membrane protein. MloK1, a cyclic nucleotide-modulated potassium channel from *Mesorhizobium loti*, is a homologue of human HCN (Hyperpolarization-activated Cyclic Nucleotide-gated) channels important for signal transduction and pacemaking. MloK1 in the presence of lipids forms micrometer-large 2D crystals diffracting only up to ~10Å. Using newly developed methods, we determined the three-dimensional (3D) map of full-length MloK1 in the presence of cAMP at the resolution of ~4.5Å (further details in Chapter 7).

CHAPTER 2

3D RECONSTRUCTION OF TWO DIMENSIONAL CRYSTALS

The following chapter has been published as:

3D reconstruction of two-dimensional crystals.
Henning Stahlberg, *Nikhil Biyani* and Andreas Engel.

in

Archives of Biochemistry and Biophysics
September 2015. Volume: *581:68-77*

Contribution:
Analysis of the problem of missing cone.

Abstract

Electron crystallography of two-dimensional (2D) crystals determines the structure of membrane proteins in the lipid bilayer by imaging with cryo-electron microscopy and image processing. Membrane proteins can be packed in regular 2D arrays by their reconstitution in the presence of lipids at low lipid to protein weight-to-weight ratio. The crystal quality depends on the protein purity and homogeneity, its stability, and on the crystallization conditions. A 2D crystal presents the membrane protein in a functional and fully lipidated state. Electron crystallography determines the 3D structure even of small membrane proteins up to atomic resolution, but 3D density maps have a better resolution in the membrane plane than in the vertical direction. This problem can be partly eliminated by applying an iterative algorithm that exploits additional known constraints about the 2D crystal. 2D electron crystallography is particularly attractive for the structural analysis of membrane proteins that are too small for single particle analyses and too unstable to form 3D crystals. With the recent introduction of direct electron detector cameras, the routine determination of the atomic 3D structure of membrane-embedded membrane proteins is in reach.

Keywords:
2D crystallization; 3D reconstruction; Electron crystallography; Lipid; Membrane protein; Missing cone

2.1 Introduction

Four decades ago Richard Henderson and Nigel Unwin produced the first three-dimensional (3D) density map of a membrane protein using electron crystallography [Henderson and Unwin, 1975]. They exploited the native arrangement of bacteriorhodopsin (bR) in highly-ordered two-dimensional (2D) protein-lipid crystals that allowed images and diffraction patterns to be recorded at low electron dose and high resolution information from beam sensitive biological sample to be extracted for the first time. Their concise article not only provided the first insight into the fold of a membrane protein but also a lucid description of electron crystallography and 3D reconstruction still valid today. After this early breakthrough it took more than a decade until the bR structure was solved [Henderson et al., 1990]. Keeping the bR arrays at liquid nitrogen or even liquid helium temperature was key to reaching atomic resolution. Yoshi Fujiyoshi developed a helium-cooled stage that allowed the bR structure to be resolved to 3 Å resolution, revealing the structure of the hydrophilic loops [Kimura et al., 1997]. Because bR resides in its native environment, the lipids bilayer, its functional cycle could be assessed and light-induced conformational changes measured [Subramaniam and Henderson, 2000].

Advances in the growth of highly-ordered 2D crystals, in sample preparation and in instrumentation led to the first structure of a human membrane channel, the Aquaporin-1 (AQP1) [Murata et al., 2000] and a few years later to the so far best resolved structure of a membrane protein by electron crystallography [Gonen et al., 2005]. The remarkable features of this AQP0 structure concern not the protein alone, but also how it interacts with the ring of lipids surrounding it. In parallel, the structure of the acetylcholine receptor arranged in highly-ordered tubular crystals was solved and conformational changes leading to channel opening were mapped [Miyazawa et al., 2003; Unwin, 2005; Unwin and Fujiyoshi, 2012].

Cryo-electron microscopy (cryo-EM) has gained a significant momentum as a unique method to acquire the 3D structure of large structures by electron tomography, providing insight into cellular structures at the nanometer scale [Lučić et al., 2013]. Single particle cryo-electron microscopy approaches have produced atomic structures and conformational changes of large complexes. The introduction of direct electron detector (DED) cameras for electron microscopy had an enormous impact on the possibilities of single particle cryo-EM: within few months, the structure of several protein complexes as small as 150 kDa were solved to 3-4 Å resolution, including solubilized membrane proteins [Kühlbrandt, 2014b].

Nevertheless, several reasons advocate the application of 2D crystallization and electron crystallography to solve the structure of membrane proteins. The first is the fact that reconstitution brings the membrane protein back into its native environment - the lipid bilayer with its matching hydrophobic core and lateral pressure [Marsh, 1996, 2007; Rosenbusch, 2001]. As lipids are known to modulate the function of membrane proteins, 2D crystals have a bonus for the study of structure-functional relationships, in particular for assessing possible protein-lipid interactions [Jeckelmann et al., 2011]. Next, many membrane proteins are smaller than what can

be currently investigated by single particle methods. Moreover, although membrane proteins need to be solubilized in some detergent for purification, reconstitution necessarily removes detergents that actually might not be suitable for 3D crystallization. Because electrons interact differently with matter than X-rays, information about charged residues can be obtained [Mitsuoka et al., 1999]. Although mostly applied to the study of 2D crystals of membrane proteins, 2D crystals of soluble proteins have shown to be attractive as well [Schultz et al., 2009]. Finally, automation in data collection, the striking advantages of DED cameras for image (or movie) acquisition [Scherer et al., 2014b], and the progress in single particle data processing of 2D crystal images [Scherer et al., 2014a] will all help to greatly improve electron crystallography, making it an efficient method primarily for studying the structure of membrane proteins in the lipid membrane.

Here, we briefly summarize the process of 2D crystallization and discuss the methodology of sample preparation, data acquisition and processing in depth.

2.2 2D crystallization

The membrane protein of interest needs to be expressed and purified to obtain a highly pure, stable and homogeneous sample. The detergent is the key to success, and sometimes incompatible with 3D crystallization protocols. Table 2.1 shows detergents that have been used for solubilization and 2D crystallization of membrane proteins. Frequently used detergents exhibit an alkyl chain and sugar head group; short alkyl chains (e.g., C8) leading to high (>1 mM) critical micelle concentrations (CMCs). Although advantageous for the growth of 3D crystals because of their small micelle dimensions, such detergents do not mimic properties of the bilayer and tend to destabilize the structure of membrane proteins. As illustrated in Figure 2.1, detergents bearing longer alkyl chains (e.g., C12) are in general well-suited to keep a membrane protein in solution [Sonoda et al., 2011], but they exhibit large micelles and low CMCs (<1 mM). Because detergents are eliminated during reconstitution, 2D crystallization offers a larger freedom of choice for the detergent than 3D crystallization.

A ternary mixture of purified membrane proteins, lipids and detergents has the capacity to assemble into a lipid bilayer packed with integrated membrane proteins upon removal of the detergent [Jap et al., 1992; Kühlbrandt, 1992, 2003; Schmidt-Krey, 2007; Stokes et al., 2010]. When the detergent concentration drops below the CMC, detergent molecules from mixed micelles transfer into the buffer solution and solubilized constituents assemble to minimize exposure of their hydrophobic surfaces to the aqueous environment. The detergent concentration can be lowered below the CMC by dilution [Rémigy et al., 2003], dialysis of the detergent, [Kühlbrandt, 2003] or by its absorption by Biobeads [Rigaud et al., 1997] or cyclodextrin [Signorell et al., 2007]. This process opens possibilities to crystallize the membrane protein within the bilayer simply by reducing the amount of lipids, thereby increasing the protein packing density. Although experimentally rather simple, reconstitution depends on complex molecular interactions

Name	CMC (mM)	M_r	Aggregation number
HTG	~29	294.4	~27
OG	18-20	292.4	27-100
OTG	~9	308.4	-
C8E4	~8	306.5	~82
CHAPS	~8	614.9	~10
DM	~1.8	482.6	~69
LDAO	1-2	229.4	~76
TX100	0.15-0.25	647*	75-165
DDM	0.17	510.6	78-149
C12E8	0.09	538.8	90-120
DHPC	-	453.5	-
LMNG	~0.01	1005.2	-

TABLE 2.1. **Detergents used for solubilization of membrane proteins and 2D crystallization:** Abbreviations: n-heptyl-β-D-thioglucopyranoside (HTG); n-octyl-β-D-glucopyranoside (OG); n-octyl-β-D-thioglucopyranoside (OTG); polyoxyethylene(4)-octyl ether (C8E4); 3-[(3-cholamidopropyl) dimethyl-ammonio]-1-propanesulfonate (CHAPS); n-decyl-β-D-maltopyranoside (DM); N,N-dimethyl-dodecylamine N-oxide (LDAO); Triton X-100 (TX100); n-dodecyl-β-D-maltopyranoside (DDM); polyoxyethylene(8)-dodecyl ether (C12E8); 1,2-diheptanoyl-sn-glycero-3-phosphocholine (DHPC); lauryl maltose neopentyl glycol (LMNG).
*Average molecular mass. Listed physico-chemical properties are according to Anatrace (www.anatrace.com).

between protein and lipid, protein and detergent, as well as lipid and detergent in the aqueous environment. For a protein that has never been subjected to 2D crystallization, these interactions are difficult to predict, making screens with different constituents indispensable. The balance between the binding constants governing interactions in this ternary mixture is decisive. Lipids need to have a stronger affinity for the protein than for the detergent that keeps the lipids in solution. Otherwise, lipids assemble to bilayers that subsequently cannot integrate the membrane protein that is forced to aggregate during further detergent removal. If proteins but not lipids release detergents first, proteins aggregate and become incompetent for membrane reconstitution during subsequent bilayer formation. Lipids have a profound influence on the crystallization process as documented by early experiments with porin OmpF [Engel et al., 1992].

The protein's stability dictates the choice of the detergent. A primary goal of initial reconstitution experiments is the identification of a suitable lipid mixture, which is achieved at high (~2) lipid-to-protein ratios (LPR; weight-to-weight (w:w)), and is usually executed over a pH range that depends on the properties of the membrane protein (e.g., its pI). Given that appropriate detergent and lipid combinations are identified, screens then concentrate on variation of the LPR

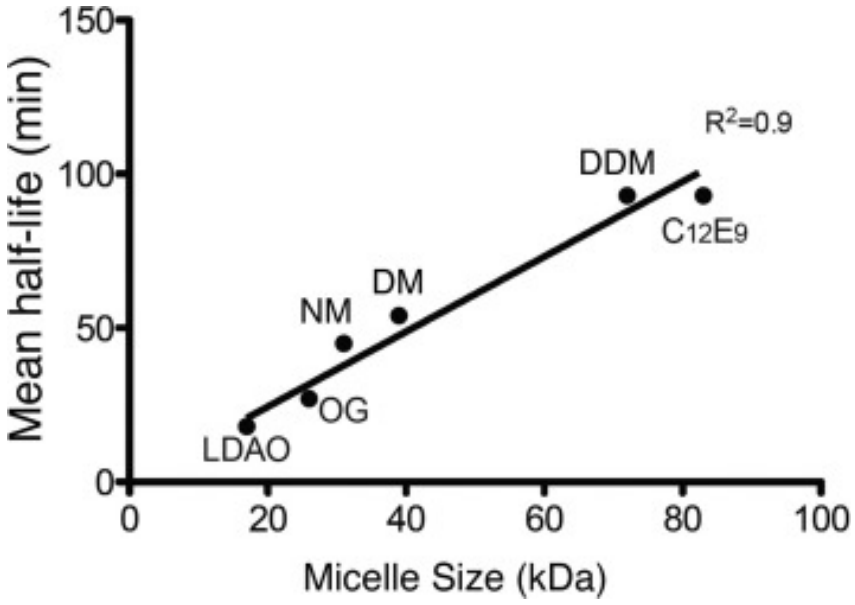

FIGURE 2.1. **Unfolding rates vs. micelle size:** The mean unfolding rates of the bacterial transporters correlate linearly with the micelle size of the detergents (adapted from [Sonoda et al., 2011]). Abbreviations: n-octyl-β-D-glucopyranoside (OG); n-nonyl-β-D-maltopyranoside (NM); n-decyl-β-D-maltopyranoside (DM); n-dodecyl-β-D-maltopyranoside (DDM); N,N-dimethyl-dodecylamine N-oxide (LDAO); polyoxyethylene(9)-dodecyl ether (C12E9).

to achieve optimal packing of the membrane protein, and on pH and salts to tune the protein's charge and the buffer's ionic strength to promote crystallization. Multivalent ions need to be explored for specific ionic interactions that may improve the packing order (e.g., magnesium and ammonium ferric citrate [Abeyrathne et al., 2010]).

Detergent removal kinetics is critical. Fast detergent removal promotes the membrane protein to interact with lipids and enhance its stability whereas slow detergent removal facilitates crystalline packing of the membrane protein. Dialysis, the most frequently used method for detergent removal, exhibits a rate that is given by the CMC of the detergent. High CMC detergents dialyze faster than low CMC detergents, typically in a few hours [Engel et al., 1992; Vink et al., 2007]. Dialysis with high-quality dialysis membranes that are chosen with a cutoff at a relatively high molecular weight allows removing detergent micelles entirely, while detergent-solubilized membrane proteins remain in solution. This then allows the removal of detergent independently of the CMC, so that also low-CMC detergents can be efficiently removed by dialysis [Jeckelmann et al., 2011]. Large ordered protein arrays of a specific protein can form within hours [Engel et al., 1992], whereas the same protein would assemble into disordered proteoliposomes upon fast dilution [Dolder et al., 1996]. Reconstitutions are generally performed at temperatures above the phase transition temperature of the used lipid. Elevated temperatures (e.g., 30-40 °C) were shown to improve crystalline order [Kühlbrandt, 1992] most probably by increasing the mobility

of the membrane proteins within lipid bilayers. Temperature increase needs to be adjusted to the detergent removal rate: to avoid protein aggregation, the membrane protein should be stabilized by major interactions with the lipids before the temperature is increased.

Injecting ternary mixtures, which are comprised of detergent, solubilized membrane protein and solubilized lipid into the sub-phase of a lipid monolayer has proven to force the lipid-protein mixture to assemble into large densely packed regions and 2D crystals upon removal of the detergent by Biobeads [Dietrich et al., 2009; Lebeau et al., 2001; Levy et al., 2001].

2.3 Data acquisition

2.3.1 Sample preparation

The preparation of 2D crystals for high-resolution imaging or electron diffraction is critical for preserving the crystal order and flatness of the fragile crystals [Abeyrathne et al., 2010; Hite et al., 2010; Schmidt-Krey and Rubinstein, 2011]. Sugar-embedding aims to preserve the protein crystals during dehydration [Henderson and Unwin, 1975]. While glucose was initially used, other embedding solutions were later employed. Trehalose preserved the native structure of bacteriorhodopsin in 2D crystals best [Hirai et al., 1999]. Sugar embedding is carried out at room temperature, and the sample is cooled in the microscope. Alternatively, the grid is plunged into liquid ethane after blotting and transferred at low temperature into the microscope to maintain the sample in a fully hydrated state. Trehalose is mainly used as embedding material in this case. Special molybdenum grids allow excellent flatness to be reached [Kimura et al., 1997]. Such grids and the carbon film sandwich method not only ensure optimal crystal flatness but also reduce sample movements during irradiation with the electron beam [Gyobu et al., 2004]. Samples exhibiting protrusion reaching out of the membrane can sometimes be distorted by the double carbon-film “sandwich” method. Such crystals are better preserved by spreading them in buffer solution on fenestrated carbon film (e.g., Quantifoil, www.quantifoil.com) grids, which are vitrified by plunge-freezing in liquid ethane [Abeyrathne et al., 2010]. Figure 2.2 summarizes the currently used sample preparation methods for electron crystallography.

2.3.2 Imaging and diffraction at low temperature

Flat and properly hydrated crystals are kept at liquid nitrogen (or even helium) temperature in the microscope to prevent sample dehydration in the vacuum and to reduce the structural decay due to beam-induced damage during data acquisition. For 2D crystal preparations that do not contain vitrified pure water but surround the 2D crystals in semi-dried sugar, liquid helium cooled crystals exhibit better beam resistance than liquid nitrogen cooled crystals [Fujiyoshi, 1998, 2011]. Nevertheless, the latter cooling method is generally used for practical reasons. Coherent axial bright-field imaging provides sufficient contrast to identify crystals at low magnification and to record images or diffraction patterns at minimum recording dose [Abeyrathne et al., 2010;

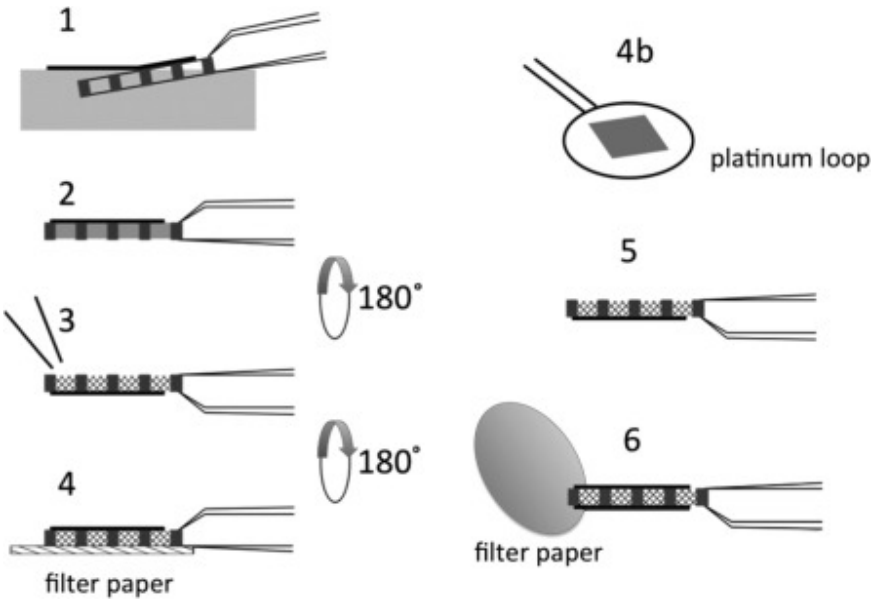

FIGURE 2.2. **2D crystal preparation strategies:** Carbon film floated on trehalose solution (1) is picked up with a molybdenum grid (2). The 2D crystal solution is added to the back-side of the grid (3), and the grid is then layered onto filter paper to resorb the surplus of sugar solution (4), followed by partial air-drying and manual plunging into liquid nitrogen to prevent full dehydration. Alternatively, a second carbon layer can be placed with the help of a platinum loop (4b) onto the back-side of the grid (5), thereby forming a carbon sandwich (6). This sandwich is blotted from the edge until semi-dry, followed by plunging into liquid nitrogen (adapted from [Hite et al., 2010]). An alternative 2D crystal preparation method consists of conventional plunge-freezing of a free-standing buffer layer of sample in the holes of a fenestrated carbon film (not shown).

Hite et al., 2010]. Field-emission electron guns (FEGs) are used for recording images that carry high-resolution phase information. High-end modern cryo-electron microscopes provide sufficient stability and optical properties to achieve a resolution of 2 Å. If size, order, and flatness of the prepared 2D crystals suffice, electron diffraction provides access to high-resolution intensity (amplitude) information.

Data acquisition strategies for obtaining 3D information are similar for imaging and diffraction (Figure 2.3). Micrographs and diffraction patterns of crystalline layers need to be recorded under different projection angles. Sample drift and sample vibrations do not affect electron diffraction patterns, but can strongly reduce resolution when recording real-space images with longer exposure times. Therefore, the highest resolution structures so far obtained by electron crystallography were all calculated from electron diffraction patterns [Gonen et al., 2005; Mitsuoka et al., 1999; Tani et al., 2009].

Traditionally, electron micrographs have been recorded on photographic film, and digitized using sophisticated scanners for subsequent digital image processing. Immediate availability

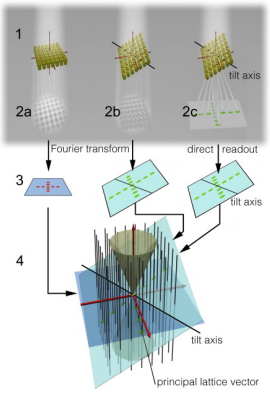

FIGURE 2.3. **Principle of 3D electron crystallography:** The electron microscope projects the structural information of tilted or un-tilted 2D crystals (1) onto the detector. Data are recorded either as real-space images (2a, 2b) or in form of electron diffraction patterns $I(h,k)$ (2c). Fourier transforms (FT) of the images correspond to diffraction patterns (3), but they consist of complex values $A(h,k)$, $\Phi(h,k)$ and therefore include amplitude and phase information. The square root of diffraction intensities, $\sqrt{I(h,k)}$, correspond to the amplitude $A(h,k)$ alone. These diffraction patterns allow values to be extracted for reflections (h,k), which are separated by noise between them. The inverse transform FT^{-1} of the thus measured values $A(h,k)$, $\Phi(h,k)$ is the projected density of a single unit cell. To obtain 3D information, projections or diffraction patterns of tilted 2D crystals are required. In 3D reciprocal space, the FT of a projection is a central section (4). The image of the untilted crystal provides information for the untilted central section (blue), whereas the image of the tilted crystal provides information for the tilted central section (light blue). Because the 2D crystal consists of a single layer, its 3D FT is a continuous complex function along z^*, the lattice line (indicated by vertical black lines at positions (h,k) in (4)). Each projection comprises a set of complex values $A(h,k,z^*)$, $\Phi(h,k,z^*)$, which upon merging the data from all projections define the lattice lines. This is indicated by green dots for reflections $(h,0)$ and $(0,k)$ in 2c, 3 and 4). While images provide high quality phase information, the amplitude information is limited by the CTF. If the crystal quality allows electron diffraction patterns to be acquired, diffraction is the method of choice to gather amplitude information, as it typically reaches higher resolution than Fourier transformed images. To fill the entire reciprocal space, 2D crystals would need to be tilted to 90°, which is experimentally not possible. Therefore, electron crystallography samples the 3D FT of the protein (also called the molecular transform) only up to the experimentally accessible maximum tilt angle, typically up to 60°. This cone of missing information (light brown in 4) results in a reduced resolution of the 3D maps perpendicular to the membrane plane. Angle Ψ between the principal lattice vector and the tilt axis (defined by angle ξ), and the tilt angle θ determine z^* for all reflections (h,k). Tilt parameters (Ψ,ξ,θ) vary continuously as does z^*, allowing the continuous function to be measured. However, lattice lines are sparsely sampled for large (h,k) and oversampled for small (h,k).

of digital images for microscope control and data processing made charge coupled device (CCD) cameras popular in all fields of electron microscopy [Faruqi and Subramaniam, 2000]. CCD cameras or also scintillator-covered complementary metal-oxide semiconductor (CMOS) cameras (TVIPS, www.tvips.com) are suitable recording devices for electron diffraction patterns, as these provide a relatively good resistivity towards the electron beam and allow recording the diffraction patterns with high dynamic range.

Electron diffraction data collection involves an instrument setup step, followed by cycles of crystal search at lowest possible dose and pattern acquisition. Electron diffraction demonstrated the possibility to acquire structural information from 2D crystals at better than 2Å resolution. However, for this, the crystals must be excellently ordered, sufficiently large (≥1 μm), and prepared by methods that keep them flat and preserve their crystallinity. Because no phase information is available, crystal defects cannot be computationally corrected, and difficulties with multilayered crystals or twinned crystals have to be considered. Although electron diffraction has initially been complemented with phase information from images, several recent high-resolution structures have been solved from electron diffraction data alone using molecular replacement [Gonen et al., 2005; Tani et al., 2009].

For recording real-space images of 2D crystals, CCD cameras are inferior to photographic film. The main reason for this is the indirect electron detection mechanism used in CCD cameras: electrons are converted into photons of light before being detected, which leads to an inferior point spread function and detective quantum efficiency (DQE) compared to film [Faruqi and Subramaniam, 2000]. Crystals that were either not sufficiently well ordered or too small in diameter were therefore in the past analyzed by recording images of photographic film, which was then digitized before computer processing.

The introduction of direct electron detection (DED) devices in cryo-electron microscopy at the end of 2013 led to a "resolution revolution" [Grigorieff, 2013; Kühlbrandt, 2014b]. These radiation-hardened and back-thinned CMOS cameras allow direct recording of the electron beam, which then leads to dramatic DQE and modulation transfer improvements. Consequently, the signal-to-noise ratio (SNR) of images recorded by such devices has much improved, in particular when single electron counting is applied. Furthermore, the low dark noise and high read-out speed of such detectors allows dose-fractionated 'movies' to be recorded [Li et al., 2013], which permits the detection and computational correction for electron beam induced drift - a breakthrough that makes the acquisition of atomic resolution images of tilted 2D crystals possible, even at high tilt.

2.4 Data analysis

2.4.1 Preprocessing of images

Figure 2.4 illustrates the data acquisition pipeline. Movies acquired by DEDs make the correction of sample movements possible [Li et al., 2013]. Images are recorded as stacks of 20-30 subframes

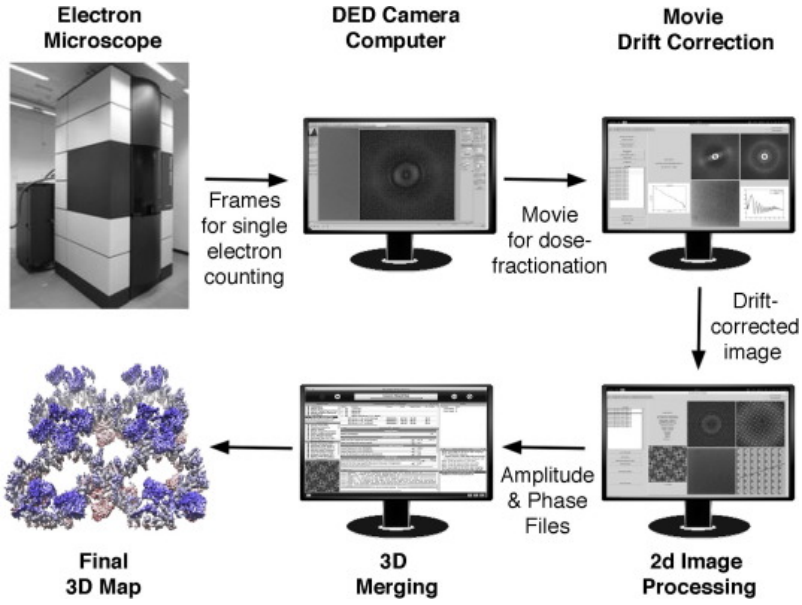

FIGURE 2.4. **The data collection pipeline:** From top left: manually identified 2D crystals are imaged with a direct electron detector camera in electron counting mode. Recorded dose-fractionated image stacks are drift corrected. The corrected and averaged stacks are channeled into the 2D image processing program, where crystal distortions are unbent and a final amplitude and phase file is produced. This together with files from other images are merged into a 3D dataset, from which the final map is calculated. These tasks can be automated [Scherer et al., 2014b].

that allow the motion to be quantified by cross correlation (CC) and corrected. Thon rings [Thon, 1966] produced by motion-corrected images recorded by an FEG instrument can be detected to a resolution of a better than 3.0 Å, indicating strong information transfer of the microscope out to such resolution. This allows to determine the amount of defocus and astigmatism of the electron microscope to better than a few nm precision. This provokes a change in the contrast transfer function (CTF) correction protocol, which previously was refined and applied after computationally unbending the crystal images. Instead, CTF correction can now be applied as a preprocessing step. Although different schemes are available for CTF correction of images from tilted crystals [Fernández et al., 2006; Henderson et al., 1990], these approximations fail to correct the CTF at atomic scale resolution [Mariani et al., 2011; Philippsen et al., 2007]. Because drift correction has produced images with such outstanding resolution only recently, the full correction of optical artifacts has not been addressed, and the stripe correction approach [Fernández et al., 2006] is still used in electron crystallography.

2.4.2 2D processing of images

As Figure 2.3 illustrates, the processing steps aim to extract amplitude and phase of the Fourier orders that define the projection of the tilted 2D crystal. Phases of diffraction peaks are obtained from the Fourier transform (FT) of the CTF corrected image. Ideally, the FT of the image of a perfect 2D crystal would exhibit for each diffraction peak (h,k) a single complex number, which corresponds to the amplitude A and phase Φ of the molecular transform (the 3D Fourier transform of the unit cell) sampled at the particular spatial frequency $(h \cdot |a^*|, k \cdot |b^*|)$, where $a^* = 1/a$, $b^* = 1/b$ represent the reciprocal crystal lattice vectors. In addition, the tilt geometry (tilt angle θ, tilt axis ξ, and the angle Ψ between the principal lattice vector and the tilt axis) needs to be determined to calculate for each spatial frequency its vertical height in reciprocal space, z^*.

2.4.2.1 Determining the tilt geometry

An initial approximation of the tilt geometry can be obtained by measuring the local defocus via Thon ring fitting in sub-regions of the images, and fitting a tilted plane through the determined field of height values. The defocus values are assumed to define the crystal plane, which is fitted with measurable accuracy. This method is fairly accurate for small tilts. For higher sample tilts, however, this defocus-gradient based approach is sensitive to small variations in magnification, which then can lead to a wrong calculation of the tilt geometry. For higher tilt angles (i.e., $\geq 15^\circ$), the tilt geometry can more reliably be refined by analyzing the distortion of the crystal lattice vectors from those of a hypothetical, non-tilted 2D crystal. The elongations of the reciprocal lattice vectors in one direction allow a precise measurement of the tilt axis and magnitude of tilt angle. The mathematical calculation of the tilt geometry from the measured lattice distortions thereby involves solving a quadratic equation that has two possible solutions, and both solutions in addition have an unknown sign for the tilt angle. From these four possible tilt geometry solutions, the one that is closest to the measurements from evaluation of the defocus gradient is usually the correct solution.

2.4.2.2 Lattice indexing

The reciprocal lattice of the 2D crystal is defined by two reciprocal basis vectors $a^*(x,y)$ and $b^*(x,y)$. These can be manually defined with an indexing tool such as provided by the 2dx software, or can be automatically determined. For the latter, an algorithm implemented in 2dx_image will de-noise and smoothen the power spectrum of a recorded image, and subject this to a peak search. For each identified lattice peak, a copy of the pre-processed pattern is then centered onto that peak, and a linear sum of all these re-centered patterns is calculated. This leads to a power spectrum pattern that shows a full set of diffraction peaks without systematic absences and usually full occupancy of low-resolution spots. Two different algorithms can then be used to

find one or several 2D crystal lattice patterns in the peaks in this power spectrum [Zeng et al., 2007]: The algorithm "getlattice" will determine the most frequently occurring difference vector among the identified peaks, which is interpreted as the first lattice vector "a^*". The second, most frequently occurring difference vector that is linearly independent from "a^*" is then taken as "b^*". The alternative algorithm "findlattice" will instead calculate a hypothetical lattice vector pair "a^*, b^*", based on the known real-space crystal dimensions and the magnification and pixel size of the image. This lattice vector pair "a^*, b^*" is then in-plane rotated over 360° in small steps, and any lattice distortion due to the known tilt geometry is applied. This set of calculated hypothetical lattice vectors is then compared with the peaks found in the processed power spectrum, and the one with the best agreement is accepted as reciprocal lattice "a^*, b^*". Any remaining reflection spots that cannot be assigned to the found lattice "a^*, b^*", are then used to find a possible second reciprocal lattice "$a2^*$, $b2^*$". Such a second lattice is often present in 2D crystal images, if the 2D crystals were of vesicular or tubular nature and were flattened onto the support film during grid preparation. In such cases, recorded images usually show two independent lattices of similar intensity, one of which belongs to one 2D crystal on the grid, and the other belongs to a second 2D crystal lying on top or below the first 2D crystal. For crystals without screw axis, the two identified crystal lattices usually have an opposite hand, i.e., one crystal lies up-side down on the other one.

2.4.2.3 Crystal symmetry

2D crystals are planar arrangement of biological objects. The crystal lattice is defined by the lattice vectors "a^*, b^*", and linear shifts by integer multiples of these vectors translate one crystal unit cell into the next one. The unit cells of a 2D crystal often have an internal symmetry. Geometric considerations show that only 17 different forms of 2D crystal types are possible for biological proteins. Besides the trivial non-crystal in p1 form, these higher-order 2D crystal symmetries have 2, 3, 4, or 6-fold in-plane symmetry, and are called p2, p3, p4, or p6 form. In addition, the unit cell of a 2D crystal can show a screw-axis symmetry, where a copy of one protein complex is found up-side down adjacent to the original one. This screw-axis copy can be at different locations and in different directions within the unit cell, leading to the remaining crystallographic symmetries p12, p121, c12, p222, p2221, p22121, c222, p422, p4212, p312, p321, and p622. No other crystallographic symmetry is possible for a single layer 2D crystal. A projection image of a non-tilted 2D crystal will usually allow the crystal form to be determined. Such a 2D projection image after image processing can further be improved by applying the identified symmetry. Images of tilted 2D crystals, however, generally do not show any symmetry, and cannot be symmetrized in two dimensions. Only after 3D merging, the final 3D map can be symmetrized, to further improve the SNR of the final map.

2.4.2.4 Crystal unbending

2D crystals are more fragile than 3D crystals that exhibit orders of magnitude more crystal contacts than 2D crystals. Hence sample preparation is extremely critical: bent carbon films will bend the 2D crystal, as would nanometer-sized carbon fragments do that can be produced by unintended carbon sputtering during film production. Lattice distortions also arise during adsorption of the crystal to the carbon film, when wrinkles may form. Moreover, 2D crystals may start growing from different nucleation sites leading to mosaic, fragmented crystals. Therefore, different strategies have been developed to extract the structural information from images of such crystals. First, the Fourier-filtered image of a crystal with small distortions is calculated, which provides a low-resolution approximation of the projection map of the crystal. The cross-correlation (cc) function of the unprocessed image with such a first average containing typically 5 x 5 unit cells exhibits clear maxima at unit cell positions. Difference vectors between the ideal fitted crystal lattice and the effective unit cell positions reveal lattice distortions and allow the coherently ordered parts of the crystal to be identified for subsequent processing. Small shifts can be corrected by lattice unbending, leading to an impressive improvement of the diffraction peak sharpness and their SNR. This improved crystal image can be Fourier filtered and iteratively used to refine the unbending process. The final unbent image is Fourier transformed to assemble a list of $A(h,k)$, $\Phi(h,k)$ measured at the positions of the lattice reflections and $z^*(h,k)$ calculated from the tilt geometry. The duplets $A(h,k)$, $\Phi(h,k)$ represent the FT of the projection map that displays the morphology of the unit cell (Figure 2.5).

2.4.2.5 The limitations of crystal unbending

In projections of 2D crystals that suffer from out-of-plane bending, lattice unbending would improve peak sharpness, but would also lead to an averaging of crystal fragments that have different tilt geometries, thereby reducing the resolution of the result. If the 2D crystals suffer from stronger lattice distortions and are imaged under sample tilt, then the projection image will show the different unit cells of the crystals from different directions, even in the absence of out-of-plane tilt. In these cases, image processing with a crystallographic unbending approach will unavoidably lead to resolution loss. Simple translation of image fragments would not solve the bending problem [Scherer et al., 2014a]. Taken together, lattice unbending can improve the data quality only for images of non-tilted 2D crystals, or for images of tilted crystals that exhibit small distortions only. Progress in single particle processing suggests that this approach should lead to significant resolution improvements also for images of fragmented 2D crystals.

2.4.2.6 Single particle processing of 2D crystal images

A single particle approach for 2D crystals consists of windowing the available 2D crystal images into stacks of small “single particle” images. Here, each such image would show one or several

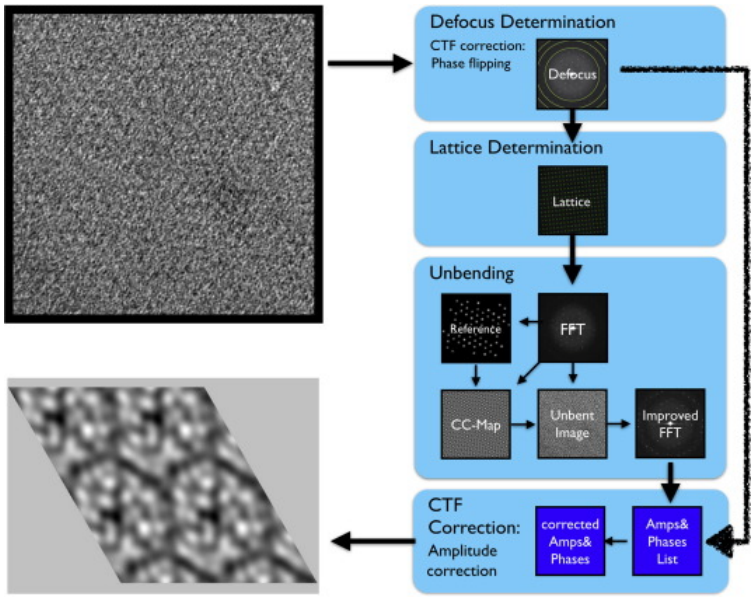

FIGURE 2.5. **The image processing workflow:** 2D crystal images are first analyzed for the microscope's contrast transfer function (CTF), for which the defocus is the most influential parameter. For images of tilted 2D crystals, the varying defocus across the tilted crystal plane complicates CTF correction [Fernández et al., 2006; Philippsen et al., 2007]. If the tilted crystal is non-flat or strongly disturbed by crystal lattice defects, a partial CTF correction by "phase flipping" is applied, which largely eliminates delocalization effects of the information in the image. As next step, the crystal lattice is determined. If the crystal is sufficiently flat crystal defects in the projected image are then "unbent", otherwise a single particle approach needs to be applied [Scherer et al., 2014a]. The final map is Fourier transformed, and values for $A(h,k)$ and $\Phi(h,k)$ are measured. These are then corrected for the remaining effects of the CTF, which in the here-described case consists of amplitude correction. The final list of corrected $A(h,k)$ and $\Phi(h,k)$ values can be used to synthesize the projection image of one unit cell. This list of values is later used during the 3D merging process.

(e.g., 3 x 3) unit cells of the 2D crystal. In contrast to conventional single particle cryo-electron microscopy algorithms, where the particles in the images are surrounded by vitrified (darker) water, however, here the windowed images contain continuous 2D crystal image, from edge to edge. In addition, the contrast difference between a membrane protein and the surrounding lipidic membrane is minimal, and membrane proteins in 2D crystals are densely packed. Projection images of tilted 2D crystals will in addition usually show the individual membrane proteins in strong overlap, whereby the image of one unit cell is overlapped by the projection image of the adjacent unit cells. And those neighboring unit cells may be in slightly deviating orientation, if the crystal was badly ordered. 2D crystals can also only be imaged up to a sample tilt angle of usually <60°, due to geometric and instrument constraints. The available particle dataset

is therefore covering a strongly non-evenly distributed angle range, with the tilt angle range from 60° to 90° being fully non-sampled. This is called the "problem of the missing cone" as the non-sampled region forms a cone-shape in reciprocal space (Figure 2.3, panel 4).

All this makes the application of conventional "single particle cryo-EM" image processing approaches, such as using EMAN2 [Tang et al., 2007] or RELION [Scheres, 2012] to a windowed 2D crystal "single particle" dataset very challenging. Particles cannot easily be "centered", the tilt angles are unevenly distributed, and the "noise" around the central particles is not Gaussian, but originates from very similar but displaced additional copies of the central particle, and is therefore "evil". A maximum likelihood based single particle approach was developed for only 2D projection images of non-tilted images in the 2dx package, which for badly ordered 2D crystals showed significant resolution improvements [Zeng et al., 2007]. A simple 3D single particle approach was implemented in the 2dx package, which applies cross-correlational maximization and weighted back-projection. This approach evaluates agreement between adjacent lattice unit cells to verify or refine the determined x,y positions, defocus, and tilt geometries for the single particles, which significantly increases the stability of the algorithm. However, novel algorithms such as a Bayesian maximum likelihood approach, Fourier space gridding, multi-volume maximum likelihood classification, or "Gold Standard" resolution estimation for limiting the reference volume during iterative refinements to eliminate reference bias [Scheres, 2012], have not yet been implemented for 2D crystal images.

2.4.2.7 2D processing of diffraction patterns

While high-quality phase information of the Fourier orders can be extracted from images of 2D crystals, amplitude information is more difficult to retrieve from images than from diffraction patterns. This is the result of the contrast transfer function of the electron microscope, which introduces drastic changes to the amplitudes that cannot be corrected in regions of the CTF zero crossings, whereas the phase shifts of π in every second Thon ring can be accurately corrected. In addition, imaging of highly tilted 2D crystals will unavoidably lead to some areas of the crystals being imaged at extreme defocus values, at which the envelope function of the CTF is less optimal: image stripes recorded at close to focus suffer from minimal contrast, and image stripes recorded at high defocus suffer from resolution loss. Finally, if the images of the sample vibrate even faster than dose-fractionated movie data collection can resolve, further resolution loss will occur. Such high-frequency sample vibration, however, can be avoided if the microscope is not suffering from technical problems such as uncontrolled local charging or mechanical vibrations.

All these problems do not affect electron diffraction, which is insensitive to sample movements and largely insensitive to variations in sample height in the microscope (the correspondence to defocus). Therefore, availability of diffraction data from large and highly ordered 2D crystals is advantageous. Moreover, in spite of the enormous progress in image acquisition, electron diffraction patterns still carry the highest resolution information.

Indexing of diffraction peaks follows the same principles as discussed for images, but needs to take into account that the central beam (0. order) is not necessarily in the center of the recorded pattern. An additional step deals with the treatment of the beam stop. Diffraction peaks are integrated over circular regions centered on lattice positions, and corrected for the background evaluated over identically centered ring-shaped regions. The Friedel symmetry of diffraction patterns gives a quality score that allows the radii of central spot and background ring to be optimized. Lattice vectors provide the tilt geometry, i.e., the z^* values so that for each diffraction pattern the merging result is a list of $\sqrt{I(h,k)}$, $z^*(h,k)$ duplets.

The package IPLT offers features to automate these steps and efficiently process hundreds of diffraction patterns with minimal manual interventions [Schenk et al., 2013].

2.5 Merging 2D data into the 3D molecular transform

All images and diffraction patterns represent central sections through the molecular transform, which is the 3D Fourier transform of the unit cell (Figure 2.3). Hence the $A(h,k)$, $\Phi(h,k)$, $z^*(h,k)$ triplets need to be combined, which requires alignment of each map to a common phase origin. It is advantageous to start the merging process from projections of untilted 2D crystals, building up the 3D data set by successively integrating the information from projections recorded at increasing tilt angles. As Figure 2.3 indicates, the molecular transform is randomly sampled along continuous lattice lines. The thickness of the 2D crystal predicts how fast $A(h,k)$ and $\Phi(h,k)$ are expected to vary versus $z^*(h,k)$. Taking this into account, the phase origin of each new central section to be added can be adjusted based on $\Phi(h,k)$ values of already merged sections with similar $z^*(h,k)$. This laborious process is difficult when data are sparse, in particular for high tilt angles. Figure 2.3 also illustrates the uneven sampling of the molecular transform in electron crystallography: low resolution lattice lines are oversampled but only up to small z^*, whereas high resolution lattice lines can comprise $A(h,k)$, $\Phi(h,k)$ duplets at z^* values corresponding to a few Å resolution, but are sparsely sampled.

As the merging step only deals with $A(h,k)$, $\Phi(h,k)$ duplets at z^* values, problems from varying magnifications do not affect electron crystallography: at this stage, any information about pixel size or magnification is no longer present, so that any variations in magnification between data collection sessions or from using different electron microscopes, or also arising from anisotropic magnification in different directions as sometimes observed on certain electron microscopes, do not affect electron crystallography processing.

Once all available sets of $A(h,k,z^*)$, $\Phi(h,k,z^*)$ duplets arising from different images are brought to the same phase origin, data are scaled to a common contrast level, and combined into one large dataset. For all of the $A(h,k,z^*)$, $\Phi(h,k,z^*)$ duplets, a background amplitude value $B(h,k,z^*)$ is also available, which was measured around the corresponding reflection. The SNR of that reflection is therefore $A(h,k,z^*)/B(h,k,z^*)$, which translates into a figure-of-merit

value $FOM(h,k,z^*)$ for each reflection. This is then used in a FOM-weighted least-squares approximation to fit linear combinations of sinc-functions through the $A(h,k,z^*)$, $\Phi(h,k,z^*)$ duplet values for each lattice line along z^*. Since the original $A(h,k,z^*)$, $\Phi(h,k,z^*)$ duplets were placed at random z^* positions along the lattice lines, the availability of fitted sinc-interpolated lattice lines allows to produce calculated $A(h,k,l)$, $\Phi(h,k,l)$ duplets along the lattice lines at regular intervals $c^* = 1/c$, whereby a,b,c are the real-space dimensions of the 2D crystal unit cell. With this information, a full 3D dataset of $A(h,k,l)$, $\Phi(h,k,l)$ is obtained, whereby for each reflection a figure-of-merit value $FOM(h,k,l)$ is also calculated, now based on the reliability of the lattice line fit.

The lattice-line fitted 3D dataset can be used as reference for further cycles of iterative refinement, in order to improve for the individual projection maps the assignments of phase origins, or the tilt geometry (i.e., $z^*(h,k)$), or the beam tilt (leading to a phase gradient over the reciprocal space, which is subtracted prior to 3D merging [Henderson et al., 1986]), or to attempt a better determination of the defocus for more accurate CTF correction.

Careful scaling of intensities for each pattern is critical for merging diffraction data sets to reduce the spread of intensity values along lattice lines. After merging and scaling all diffraction patterns, parameters of each pattern are cyclically refined, to improve intensity scale factors as well as assigned sample tilt geometries (i.e., z^*). Finally, the more reliable amplitudes from diffraction experiments and the phases from processed real-space images can be combined. If homologous structures are available, molecular replacement (MR) commonly used in X-ray crystallography can be applied to obtain structure phases and to determine the final model only from electron diffraction data.

Finally, the most likely 3D map for the protein can be calculated by Fourier inversion of the FOM-weighted amplitudes $A(h,k,l)$ with phases $\Phi(h,k,l)$. 2D and 3D processing are all integrated in the 2dx software (http://2dx.org).

2.6 The missing cone problem

2D crystals can only be imaged or subjected to electron diffraction up to a sample tilt angle of approximately 60 degrees. In addition, images and diffraction patterns of 2D crystals that are not forming a perfectly flat plane or that required stronger unbending will show more resolution degradation at higher tilt angles. Finally, when exposing a carbon-adsorbed 2D crystal sample to an electron beam, in the majority of cases, the sample will show a drum-head like movement in the direction perpendicular to the carbon film, which strongly degrades the resolution in images, if the sample is tilted. This drum-head movement can be reduced but usually not eliminated, when a symmetrical carbon sandwich construction for the specimen is used [Gyobu et al., 2004]. Dose-fractionated “movie mode” image data collection and also recording data in electron diffraction mode can reduce or even eliminate the latter problem. Nevertheless, when analyzing electron

crystallography data in Fourier space, data are generally missing entirely in a cone covering the tilt angle from 60° to 90°, and even before that, data have much lower resolution in the wider cone from 30° tilt angle and higher, due to the resolution losses mentioned above.

This phenomenon is generally referred to as the "missing cone" problem in electron crystallography, as illustrated in Figure 2.3, panel 4. In real space, this makes densities being elongated and smeared out in the vertical direction. Thus, the resolution of final volume is expected to be better in the x and y direction, than in the z direction.

Gipson et al. [Gipson et al., 2011] developed a method called Projective Constraints Optimization (PCO), which can be used to reconstruct the missing amplitudes and phases in the missing cone in the Fourier domain. The PCO method relies on iteratively applying known quantities of the electron density map as constraints in real and Fourier space [Agard and Stroud, 1982]. Here, several constraints were implemented, exploiting the fact that the densities in real space are non-negative, symmetric (if applicable), and membrane slab bounded, and in reciprocal space were bounded by a known resolution range and described by a certain scattering profile. Gipson et al. applied these constraints in each iteration only in small fractional steps, during which the current values were partly retained and partly modified according to the constraints. At a later stage in the algorithm, the horizontal slab-foundation constraint was replaced by a shrink-wrap constraint, where the low-pass filtered and thresholded density itself was used as masking constraint.

In each iteration, this algorithm is able to recover information in the previously unknown missing cone region, by creating amplitude and phase information for a few reciprocal pixels covering 1/D into the missing cone, where D is the characteristic size of the compact support. Iterative application of this algorithm converges to one of several possible stable solutions. A swarm optimization algorithm was then used to find the best, "globally optimal" solution, which is defined by the solution with the least required corrections in each iteration. Gipson et al. were able to show that this algorithm allows to largely compensate for the effect of the missing cone, if a sufficiently large dataset of high SNR is available.

In addition to reconstructing the data in the vertical direction, the PCO algorithm also allows to convert the measurements from the non-uniformly sampled reciprocal space to the uniformly spaced real space, without involving the traditional lattice line fitting, which uses sinc interpolation. PCO thus offers the advantage of using raw data directly as constraints during the iterative PCO algorithm, which avoids the repeated interpolation errors that sinc fitting would give.

2.7 Quality assessments

For 2D crystal images, the ratio between the amplitude $A(h,k)$ of a diffraction spot compared with that of its surrounding $B(h,k)$ can be quantified by so-called IQ values, which are defined

as the ratio $7 * B(h,k)/A(h,k)$ [Henderson et al., 1986], whereby the amplitude is calculated as that above background. A spot with the label $IQ = 1$ therefore has an amplitude of at least 7 times that of its average background. A spot with $IQ = 2$ has an amplitude of at least 3.5 times its background, etc. A spot with $IQ = 8$ has an amplitude smaller than the background, and a spot with $IQ = 9$ is defined as one where the amplitude is negative, so that the overall amplitude is even below background value at that location. Inspecting the distribution of IQ values for an evaluated calculated Fourier transform of an image allows a first estimation of the resolution of a 2D crystal images. It also allows progress in crystal distortion unbending to be monitored, as long as no strong reference bias is introduced.

Reference bias is a significant problem also for 2D crystal image processing: If the unbending reference contains high-resolution details, be it right or wrong, and the unbending algorithm is allowed to freely shift close image patches onto the predicted location as soon as the signal shows maximal correlation with the reference, then the risk is high that the unbending aligns the noise patterns in the images onto the crystal lattice, instead of the protein images themselves. The 2D crystal unbending algorithm therefore should be applied carefully, in order to not suffer from reference bias. Iterative re-unbending of already unbent images, or unbending with liberal unbending parameters and a high-resolution reference are pitfalls that should be avoided.

For projection maps of precisely non-tilted 2D crystals of a symmetry group that shows a higher symmetry, accurate and reliable resolution estimation can be obtained by comparing the reflections with their symmetry-related counterparts, by calculating so-called phase residuals in resolution ranges. This allows to precisely quantify the reliability of different resolution ranges for single images of strictly non-tilted crystals. This, however, only gives a reliable answer, if the reference used for unbending was not symmetrized before.

For images of tilted 2D crystals, the projection image usually does not show any symmetry. Here, the resolution of an evaluated $A(h,k,z^*)$, $\Phi(h,k,z^*)$ duplet can only be determined after 3D merging, at which point a resolution-dependent phase residual for that image or for the entire 3D dataset can be calculated.

Iterative re-unbending of the images, using the latest 3D reconstruction as reference, as implemented in the 2dx package, bears the risk to introduce artificial reference bias to the initial unbending step, after which IQ statistics and phase residuals may appear wonderful, but only reflect the self-consistency of the algorithm and not the true structure. Care should therefore be put into an unbending approach that does not introduce any reference bias, but produces a Gaussian-distributed result. In that case, application of a negative temperature factor to invert the Gaussian falloff can always be applied, as long as no artifacts are present.

The later steps of 3D merging deal with the $A(h,k,z^*)$, $\Phi(h,k,z^*)$ duplet datasets with their $FOM(h,k,z^*)$ weights. The FOM weights for each Fourier reflection allow more reliable iterative refinement of parameters such as the phase origin or the sample tilt or beam tilt, so that reference bias is less of a risk.

2.8 Conclusions

Electron crystallography of 2D crystals determines the structure of membrane proteins in the lipid bilayer by imaging with cryo-electron microscopy and image processing. Growing well-ordered 2D crystals of membrane proteins is an often difficult and time-consuming task. However, the success rate for obtaining 2D crystals from a protein preparation is better than for obtaining 3D crystals. In addition, a 2D crystal presents the membrane protein in an active and fully lipidated state, where the protein can easily be exposed to different environmental conditions such as different buffers or addition of ligands.

Electron crystallography can determine the 3D structure also of small membrane proteins. Resulting reconstructions have a better resolution in the membrane plane than in the vertical direction. This problem can be partly eliminated by applying an iterative algorithm that exploits additional known constraints about the 2D crystal, such as for example its vertical boundary within a horizontal slab. With the recent introduction of direct electron detector cameras, the routine determination of the atomic 3D structure of a membrane-embedded membrane protein is in reach. For these reasons, we are convinced that electron crystallography in its niche will continue providing important biological insight for the understanding of the function of membrane proteins in lipid membranes.

PART II

ASSISTING IMAGE PROCESSING IN CRYO-EM

CHAPTER 3

EMKIT: A MULTIDIMENSIONAL C++ TOOLKIT FOR CRYO-ELECTRON MICROSCOPY

The following chapter is a manuscript in preparation:

***EMKIT*: A multidimensional C++ toolkit for cryo-electron microscopy**
Nikhil Biyani and Henning Stahlberg.

Contribution:
Software design and development of the toolkit.

Abstract

The resolution revolution in cryo-electron microscopy is a combined effort of hardware developments such as direct electron detectors and boost in algorithms and software resources. But there are many more challenging problems to be solved and would require development of software resources in cryo-EM. Fast processing of stacks with hundreds of "8k" images is required and thus performance has to be kept at topmost priority. In this chapter, we introduce EMKIT, a fast and efficient library built using C++ STL with C++11 standards. EMKIT adds a multidimensional concept to STL, features data structures and methods commonly used in cryo-electron microscopy and can be used by developers to build complex features conveniently.

Keywords:
Image Processing, Toolkit, Cryoelectron Microscopy, Multidimensional C++ STL

3.1 Introduction

Processing cryo-electron microscopy images is one of the most challenging problems in the field of image processing [Doerr, 2015; Fernández, 2008; Herman and Frank, 2014; Sigworth, 2016]. The recorded images in general have low signal to noise ratio, are modulated by a contrast transfer function and suffer from sample movements. Additionally, as the target object is three dimensional an appropriate strategy has to be devised for its generation from recorded 2D data [Herman and Frank, 2014; Stahlberg et al., 2015]. Fourier transformation of images play an important role in the whole image processing pipeline. Reduction of noise via low pass filters or merging 2D data via central projection theorem to generate 3D volumes are the few cases where Fourier transformation is indispensable.

This decade has featured Direct Electron Detectors (DEDs), which can directly sense and count the electrons unlike the previous detectors that were based on light detection. With the advent of these devices, the signal to noise ratio of the images recorded from electron microscopes has drastically increased. Furthermore, these detectors are so fast that instead of one, a sequence of images can be recorded in a single exposure. This helps in reducing the motion effects that arise during recording and makes the resultant images look sharp. These hardware advancements when topped with the advancements in image processing algorithms like maximum likelihood methods, movie mode corrections has lead to the resolution revolution in the field of electron microscopy [Frank, 2017; Kühlbrandt, 2014a].

The advancements that we see today mark the beginning, there are many more to be followed [Frank, 2017; Rossmann et al., 2011; Wang, 2015]. Many new software resources in cryo-EM are to be developed in the near future. They would have to deal with stacks containing hundreds of "8k" images. To process this amount of data, a fast and efficient software program is a must. In some cases the complicated image processing operations on the stacks of images would have to be finished in real time, so that the users can get an update of quality of image while recording it. This brings the need of a toolkit/library which can be used by developers to have fast basic operations and build their features on top.

Numerous packages like SPARX [Hohn et al., 2007], IMOD [Kremer et al., 1996], FREALIGN [Grigorieff, 2016], RELION [Scheres, 2012], SPIDER [Leith et al., 2012], XMIPP [de la Rosa-Trevín et al., 2013] provide the functionality to carry out most of the operations that typically occur in the image processing pipeline. Most of these software provide pre-compiled executables or functions to perform a particular operation. These functions can be clubbed in python or shell scripts to produce user defined workflows. But, in most cases, the internal data structure is not exposed which results in the reduction of flexibility. Processing tasks in electron microscopy are computationally heavy and thus a better control over the data structures and memory management is required. We here introduce EMKIT, a ready to use, fast and optimized toolkit written in C++. EMKIT implements common data structures and methods used in the field of cryo-EM including multidimensional real and Fourier objects. Complex objects and methods can

be built using the data structures available. This toolkit is an extension of commonly used C++ standard template library (STL) for the developers in cryo-electron microscopy.

3.2 Programming environment

Electron Microscopy processing tasks are computationally heavy and performance has to kept at utmost priority while programming. In object oriented programming, abstractions such as polymorphism, virtual functions and function pointers come at added performance cost. Templates in C++ allow to use these abstractions with no added performance cost at runtime; the downside being that compile time increases drastically which is not a major concern in the current scope. Using templates, specific objects can be passed on to the functions as template parameters that can be deduced while compilation and produces no runtime overheads. Memory management for memory heavy tasks in electron microscopy can be easily done using C++. Thus C++ proves to be a superlative choice as the programming language.

The C++ standard template library (STL) is a set of many general purpose C++ templated classes and functions that implement commonly used data structures such as lists, vectors, stacks and algorithms such as searching and sorting techniques. STL is divided in three major components: (i) containers that store the data, (ii) iterators that allow to access the data in a specific manner and (iii) algorithms that use containers via iterators and implement the commonly used algorithms. EMKIT is built on the same principles used by STL. Additional multidimensional containers (discussed in next section) and their associated iterators are designed that can be used to represent almost any arbitrary data structure in cryo-EM. Moreover, algorithms like Fourier transformation occur as templated methods and can operate on any of these multidimensional containers.

EMKIT uses all the features that C++ introduced with its C++11 standards and brought many performance and productivity benefits to the existing STL. Performance improvements include (i) introduction of move semantics that can move an object from one location on memory to another without creating temporary objects and, (ii) template metaprogramming that allows to specialize templates with particular characteristics. C++11 standards have also made it easy to write code in C++ with the introduction of range based for loops, lambda expressions, auto keyword, smart pointers and many more such features. Using C++11 standards would thus enable the programmers to quickly write easy-to-understand code.

3.3 Multidimensional functionality

Cryo-EM often deals with multidimensional data, for instance, electron density maps, atomic models, Fourier volumes. STL does not provide any containers or iterators that can deal with multidimensional data that typically occur in cryo-EM. EMKIT fills this gap by introducing three different multidimensional container classes: (i) Tensor class that stores data in regular

multidimensional grid, (ii) Sparse tensor class that uses a hashmap to store only the sparse indices in a multidimensional grid, and (iii) Table class that can store multidimensional data in tabular form. Additionally, a Tensor iterator class is introduced that can help to linearly iterate through the indices in any tensor. Multidimensional indices are represented using the Index class. The following sections briefly describe these classes.

3.3.1 Index class

Indices are the basic elements that introduce multidimensionality to measures such as coordinates, distance, frequencies. Index class in EMKIT is a templated class which stores a set of integer values of a particular dimension (or rank).

```
template <int rank> class Index;
```

Index class can be constructed either using a single integer value which initializes all the indices to that value or using an initializer list that assigns the indices to the elements in the list.

```
Index<3> id = Index<3>(0); // Initialize all the indices by 0
Index<3> id = {1,2,4}; // equivalent to an index of (1,2,3)
```

Index class has assignment operators, element access methods, comparison operators, arithmetic operators, scaling operators and stream extraction operator in-built. Index class additionally implements a 'contains' method which checks if the provided index is contained in the current index or, in other words, the provided index is smaller than the current index. This method proves to be useful when index is used as a size of the volume or grid and any arbitrary index is bounded within this size.

3.3.2 Tensor class

Tensor class is a multidimensional representation that stores data in a regular grid and is templated on the data type it stores, its rank and the storage order.

```
template<typename DataType, int rank, StorageOrder order> class Tensor;
```

Any type that implements comparator and arithmetic operators can be used as the data type of the tensor. Data can be stored in both row major and column major formats; former has elements of rows in contiguous memory and the later contains elements of columns in contiguous memory. The row and column notations does not make much sense in multidimensional scenario and in that case the memory location of an element is given by following equations:

$$offset_{row-major}(i,j) = \sum_{i=1}^{r}(\prod_{j=i+1}^{r} N_j)n_i \tag{3.1}$$

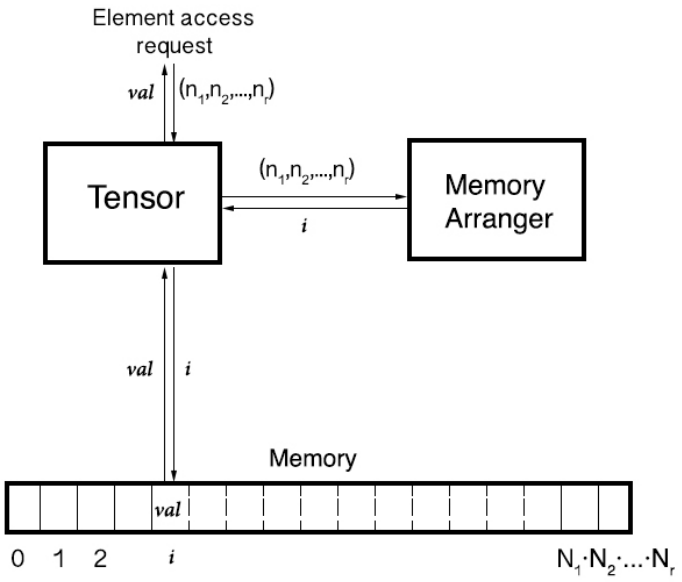

FIGURE 3.1. **Memory arrangement in the Tensor class:** Tensor class stores data in a contiguous memory and uses the memory arranger class to identify the linear offset in memory from the multidimensional index. This offset depends on the storage order of the tensor. Any operation that requires element access from tensor class goes through this memory arranger to first identify the offset and then value can be fetched from the identified location.

$$offset_{column-major}(i,j) = \sum_{i=1}^{r}(\prod_{j=1}^{i-1} N_j)n_i \tag{3.2}$$

where r provides the rank of the index, n_i and N_i are the index and size at i^{th} dimension respectively. The equations (3.1, 3.2) provide offset in memory for row major and column major storage orders.

An instance of tensor is created by defining its range (the maximum allowed index) and origin. Internally, tensor class stores the data in a contiguous memory using a STL vector. The multidimensional index that is associated with each of these contiguous memory locations depends on the storage order (Figure 3.1). Arithmetic operators, assignment operators, comparison operators and stream operators are all implemented for this class. Tensor class also provides methods to get a slice: i^{th} slice is a tensor with a rank smaller by one and is a subset of all the elements contained over the most significant index being i. Smaller sections of the tensor class can be accessed using the 'section' method. In electron microscopy, tensor class objects are useful to represent data structures such as electron density maps, image stacks, stack of stacks, set of particles, etc.

3.3.3 Tensor iterator

Tensor iterator implements all requirement of a STL random access bidirectional iterator and provides the capability to traverse the indices in a linear way. Range based for loops can be conveniently written using this iterator. The iteration starts with the lowest index and at every increment the least significant coordinate is increased by 1, or in other words, each increment yields the next element stored in memory. For row major tensors, the row index is increased by 1 and for column major tensors column index is increased by 1. The same holds true for every decrement in a similar way. Thus all the indices can be sequentially traversed bidirectionally from front or reverse. At any point, the current index can be found by calling the 'index' property of the iterator and the value can be accessed by calling the 'value' property.

```
for(auto pixel : image) {
   pixel.index // Provides the index of the pixel
   pixel.value // Provides the value at the pixel
}
```

3.3.4 Sparse tensor class

Sparse representation, when applied appropriately, can prove to drastically reduce the memory consumption and in turn can increase the performance tremendously. Many data structures in electron microscopy like masks, diffraction images have sparsely populated multidimensional data and can use the sparse representation. EMKIT incorporates this through the sparse tensor class which is templated over data type and rank. Every sparse data point is stored in a hashmap with keys containing indices that are mapped to corresponding values of the data type specified. Any instance of sparse tensor class can be initialized by providing its range and a default value. Sparse tensor class provides assignment operators, arithmetic operators and scaling operators. Using this class one can store an "8k" binary mask (which would usually take 256MB space) to a maximum space of 32KB.

3.3.5 Table class

Tables occur in reflection files that provide the amplitude and phase on different miller indices, or in an atomic coordinate file that provides a list of coordinates mapped to the details of atom at that location. These type of structures can be conveniently handled by the Table class provided by EMKIT. Any table class object can be initialized by providing the columns count and optionally a row count. The number of rows and columns can be changed during runtime. The data is internally stored as a vector containing vectors of string (`vector<vector<string>>`). This allows to conveniently access the data in all those formats that can be converted from string. Tables can be directly read from a file using the 'read_table' function and can be written to file using

the 'write_table' function. This class provides manipulations like changing a column, reducing a column, sorting by a column, etc. The following code snippet demonstrates some of these functions:

```
Table table = read_table(``XXXX.pdb'');
// Set the fourth column to zeros
table.set_column(4, vector<double>(table.rows(), 0.0));
// Sort using column 2, considering it has int values
table.sort<int>(2);
table.write_table(``XXXX_modified.pdb'');
```

3.4 Adaptation to electron microscopy

Direct use of the multidimensional classes introduced in the previous section can sometimes be cumbersome for cryo-EM operations. For this reason convenience classes and typedefs adapted for use in electron microscopy are implemented in EMKIT and are discussed in the sections below.

3.4.1 Real and complex objects

The objects that exist in electron microscopy can be subdivided into two major categories: Objects like density maps, particles, stacks of images, etc. that store real valued data and object like Fourier images that store complex values at various indices. Tensor and Sparse tensor classes introduced can handle both types of data. A real object is defined using template specialization of a tensor with column major storage order:

```
template<typename ValueType, int rank>
using RealObject = Tensor<ValueType, rank, COLUMN_MAJOR>;
```

Complex objects are template specializations that hold complex values in a tensor using column major storage order:

```
template<typename ValueType, int rank>
using ComplexObject = Tensor<Complex<ValueType>, rank, COLUMN_MAJOR>;
```

Some algorithms operate on real objects and others on complex object; classes 'is_real_valued' and 'is_complex_valued' that define the type traits of the objects are implemented. Each of these classes have a boolean constant field 'value' that would return the result if a class is real or complex valued.

3.4.2 Complex-half-object

Discrete Fourier transformation (DFT) is an integral part of processing in electron microscopy. DFT and inverse-DFT are lossless transformations, i.e., DFT followed by inverse-DFT outputs the same signal. Furthermore, the DFT of a real valued function is conjugate symmetric, i.e., $F(-x) = F^*(x)$, where $F(x)$ represents the Fourier transform and $F^*(x)$ represents its conjugate. This way only half of the Fourier space should be physically stored and the rest can be calculated using this property; enabling to reduce the memory requirements to half without the loss of any functionality. Complex half object class provided with EMKIT can conveniently handle the creation of these types of objects. Although only half of the space is stored, yet user requests accessing values spanning over the complete space is handled; the values not stored are calculated during runtime.

Complex-half-object class is derived from the Tensor class and is templated over data type and rank:

```
template<typename DataType, int rank>
class ComplexHalfObject :
public Tensor<Complex<DataType>, rank, COLUMN_MAJOR>
```

Instances of the class can be created using the logical size of the corresponding real space. Methods to access the values at various Miller indices, fetch the maximum and minimum miller index are provided with the class.

3.5 Convenience methods

EMKIT offers easy to use templated methods that using the multidimensional objects help to carry out typical operations in cryo-EM. Most of these methods are made as generic as possible, thus providing a flexibility. Fourier transformation, object conversions, file input/output, statistics calculations and Fourier filtering are programmed and discussed in the following sections.

3.5.1 Fourier Transformation

Algorithms like 3D reconstruction using central projection theorem, Fourier filtering and cross correlation in electron microscopy rely on transformation of generated electron density maps to Fourier spaces and vice-a-versa, commonly known as forward and inverse Fourier transformation. These multidimensional transformations involves delicate handling of issues such as choice of origin, size of Fourier space and generation of half spaces using conjugate symmetry. EMKIT with its function 'fourier_transform' handles these issues and provides a convenient way to transform between spaces. A real object after forward FFT is converted to complex-half-object and a complex-half-object after inverse FFT is converted to real object. The direction of transformation

(forward or inverse) is automatically detected using the type of input and output provided. The following example illustrates this:

```
RealObject<double, 3> real;
ComplexHalfObject<double, 3> complex;
fourier_transform(real, complex); // Performs forward FFT
fourier_transform(complex, real); // Performs inverse FFT
```

FFTW, a freely available fast Fourier transformation (FFT) library for most platforms, is used to carry out these operations. FFTW plan objects store data that FFTW needs to compute the FFT. These plans are data independent and once created it can be used to carry out the transformation between the input and output arrays multiple times. EMKIT exploits this functionality using a store for plans. Applicability of existing plans in the store is first checked before creating new ones.

3.5.2 Object Conversions

Conversion of objects with different origins, storage order, data types is made easy with the 'convert' method that comes with EMKIT. This method accepts input in the form of a tensor object, analyses the type of output tensor object and converts it by automatically calling required methods. This makes the conversion between objects such as complex-half Fourier object and real object even more flexible. The example below shows the conversions from a column major tensor to a row major one:

```
Tensor<double, 2, COLUMN_MAJOR> cmTensor;
Tensor<double, 2, ROW_MAJOR> rmTensor;
// ...
// Initialization of cmTensor and other operations
// ...
convert(cmTensor, rmTensor); // Convert the storage order of the tensor
```

3.5.3 File Input/Output

Reading and writing files is one of the most frequently used operation. In electron microscopy, MRC file format has become a standard to store the electron densities and their Fourier transforms. The data is stored in binary format with the first 1024 bytes of file containing the metadata including grid size, cell size, etc [Cheng et al., 2015]. Over the years the header representation in the MRC files have changed and other formats like CCP4 MAP have emerged. EMKIT supports reading and writing data in various MRC file formats as well as MAP file format using the generic 'read' and 'write' methods. These functions can also read and write reflection files containing miller indices, phase, amplitude information in columns. File format can be automatically de-

duced using the extension from the file name or can be manually specified. The 'read' function is templated and can read all object types described in the section above:

```
template<typename ObjectType>
bool read(std::string file, std::string format, ObjectType& obj)
```

Similarly the'write' function supports writing the objects in various file formats:

```
template<typename ObjectType>
bool write(std::string file, std::string format, const ObjectType& obj)
```

This implementation ensures that any type of file can be flexibly read to any type of object and similarly any type of object can be written to various file formats. The conversion of objects is internally done. Some examples showing this flexibility are provided below:

```
RealObject<double, 3> input;
read(''protein.mrc'', input); // Reads data in mrc format
write(''protein.map'', input); // Writes data in map format
```

3.5.4 Statistics calculation

EMKIT provides methods to calculate statistical measures such as minimum, maximum, standard deviation, squared sum, minimum element, etc. of a multidimensional object. As in the STL algorithms header function, these functions can be employed to any tensor through its iterator. A begin and an end position of the iterator is specified and the measures are calculated using all the elements that lie in the specified range. Following examples illustrate some of these functions:

```
min_value(image.begin(), image.end()); // Min value in the image
min_index(image.begin(), image.end()); // Index where the min value occur
standard_deviation(image.begin(), image.end()) // Standard deviation of the image
```

3.5.5 Fourier filtering

Fourier filtering involves removal of certain frequencies from the Fourier space that lie below or above a certain threshold; low-pass filter removes selected high frequencies, high-pass filter removes selected low frequencies based on a threshold value and a band-pass filter involves two thresholds combining both low-pass and high-pass filters. This can be achieved using many algorithms, for example, Gaussian, Butterworth, top-hat, etc. EMKIT implements Gaussian and top-hat filtering algorithms using 'low_pass', 'high_pass' and the 'band_pass' methods. These methods can be employed on any complex object.

3.6 Availability

EMKIT is an open source library protected with MIT license. The source code can be downloaded from the website: http://c-cina.github.io/emkit/. EMKIT additionally depends on the FFTW library that can be download from: http://www.fftw.org/download.html. The library is easy to use as most of the source code is available in header only files. The library comes along with many examples explaining the usage of various components.

3.7 Conclusion

A library was designed and implemented in C++ using STL concepts: containers, iterators and methods. The library expands STL and supports multidimensionality using the Tensor and its associated classes. This multidimensionality helps to represent commonly used objects in cryo-EM including real spaces, complex half spaces, etc. Furthermore, methods such as file input/output, Fourier transformation using FFTW library, object converters, statistical calculation using iterators and Fourier filtering are implemented. Future work includes optimization of the toolkit for high performance computing including parallelization using C++11 threads, MPI and CUDA.

CHAPTER 4

FOCUS: THE INTERFACE BETWEEN DATA COLLECTION AND DATA PROCESSING IN CRYO-EM

The following chapter has been published as:

Focus: The interface between data collection and data processing in cryo-EM
Nikhil Biyani, Ricardo D. Righetto, Robert McLeod, Daniel Caujolle-Bert, Daniel Castano-Diez, Kenneth N. Goldie and Henning Stahlberg.

in

Journal of Structural Biology.
May 2017. Volume: *198(2):124-133*

Contribution:
Conceptualization, design and programming of the interface and funtionalities.

Abstract

We present a new software package called Focus that interfaces cryo-transmission electron microscopy (cryo-EM) data collection with computer image processing. Focus creates a user-friendly environment to import and manage data recorded by direct electron detectors and perform elemental image processing tasks in a high-throughput manner, while new data is being acquired at the microscope. It provides the functionality required to remotely monitor the progress of data collection and data processing, which is essential now that automation in cryo-EM allows a steady flow of images of single particles, two-dimensional crystals, or electron tomography data to be recorded in overnight sessions. The rapid detection of any errors that may occur greatly increases the productivity of recording sessions at the electron microscope.

Keywords:
Cryo-EM, High throughput image processing, Automated data collection, Drift correction

4.1 Introduction

Cryo-electron microscopy (cryo-EM) and cryo-electron tomography are employed in structural biology to determine the structure of vitrified biological samples, such as isolated proteins and protein complexes, two-dimensional (2D) protein/lipid crystals, or larger biological objects such as bacteria and nanocrystals. Until the development of direct electron detector cameras (DED) for electron microscopy, the resolution achieved in most cases was in the 5 - 30Å range, with few exceptions [Gonen et al., 2005]. Unlike detectors that convert the electron signal to light via a scintillator, DEDs have radiation-hardened metal oxide semiconductor sensors that can be directly illuminated with the high-voltage primary electron beam. This architecture greatly reduces the point-spread function of the electron signal and results in superior detector quantum efficiency, enhanced readout speed and an excellent signal-to-noise ratio (SNR). The resolution required to count single electron events is achieved. Furthermore, the low read-out noise of DEDs makes it possible to record electron dose-fractionated multi-frame exposures, known as image stacks or movies. This means that movement of the sample during imaging can be corrected by software, as discussed further below. Averaging the aligned motion-corrected frames after they have been weighted by a dose-dependent B-factor to account for damage to the proteins by the electron beam, results in images that have superior resolution and a better SNR [Rawson et al., 2016]. Together with improved image processing algorithms, such as maximum-likelihood [Lyumkis et al., 2013; Sigworth, 1998] and Bayesian [Scheres, 2012] methods, this has led to a resolution revolution in cryo-EM [Kühlbrandt, 2014b] with the result that atomic models of the imaged biological structures can quite often be built [Kühlbrandt, 2014b; Liu et al., 2016; Merk et al., 2016; Yu et al., 2016].

The Gatan K2 Summit DED camera was the first to offer three recording modes. In the first mode, the linear mode, the energy deposited in the DED sensor by passing electrons is integrated over the entire exposure time. In the second mode, termed electron counting, single electron events are individually detected and counted. Finally, in the super-resolution mode, the camera driver registers the impact location of individual electrons on the detector with sub-pixel accuracy during the electron counting step, resulting in final images of twice the pixel resolution than the hard chip of the DED detector. Image data are ideally recorded in super-resolution mode as multi-frame exposures of each region of interest. Use of the super-resolution algorithm means that the “4 k” chip (3838 × 3710 pixels) of a K2 Summit DED records “8 k” frames (7676 × 7420 pixels). Subsequently downsampling these frames to “4 k” by cropping in Fourier space, results in 4 k images with a SNR significantly superior to the SNR of 4 k images directly recorded in the “4 k” counting mode, due to the effect of anti-aliasing (see also [Ruskin et al., 2013]).

When multi-frame exposures are recorded using a DED, the total dose given to a region of interest is fractionated, allowing the images in the stack to be aligned by post-processing to eliminate specimen movement originating from physical drift of the specimen stage, electronic drift in the imaging system of the microscope, or physical movement of the sample under the

electron irradiation. Several software packages are available to correct specimen motion, including Zorro [McLeod et al., 2016], MotionCor2 [Zheng et al., 2016], Unblur [Grant and Grigorieff, 2015], alignparts_lmbfgs [Rubinstein and Brubaker, 2015], MotionCorr [Li et al., 2013], and SerialEM [Mastronarde, 2005]. Among them, Zorro, MotionCor2 and alignparts_lmbfgs perform both whole-frame and local drift-correction. In most cases, additional local drift-correction significantly improves the quality of the output image, but also increases the computational costs considerably. Optimally, the microscope operator should be able to view drift-corrected and averaged images directly on the camera computer during the microscopy session. Thus, the development of software tools that can achieve whole-frame 'on the fly' drift correction has gained interest [Fernandez-Leiro and Scheres, 2016; Li et al., 2015; Noble and Stagg, 2015]. Local-drift correction cannot (yet) be computed during data collection on a conventional DED camera driver, due to limitations in computing speed.

Once image stacks have been corrected for drift, they can be processed further using a reconstruction software package such as RELION [Scheres, 2012], FREALIGN [Grigorieff, 2007], CryoSPARC [Punjani et al., 2017], IMAGIC [van Heel et al., 2012] or EMAN2 [Ludtke, 2016; Tang et al., 2007] for single particles, IHRSR [Egelman, 2007] or Spring [Desfosses et al., 2014] for helical proteins, Dynamo [Castaño-Díez et al., 2012], PEET [Nicastro et al., 2006] or Jsubtomo [Huiskonen et al., 2010] for sub-tomogram averaging, or 2dx [Gipson et al., 2007a,b] for 2D electron crystallography. Further, software packages like Scipion [de la Rosa-Trevín et al., 2016] and Appion [Lander et al., 2009] aim at unifying the software available for single particle reconstructions, by allowing the output from one package to be used as the input for another in a transparent and manageable way.

As large data sets need to be recorded and processed, software packages such as SerialEM [Mastronarde, 2005], Leginon [Suloway et al., 2005], UCSF-Tomography [Zheng et al., 2007], Tom Toolbox [Nickell et al., 2005], EPU (Thermo Fisher Co.), Latitude in Digital Micrograph (Gatan Co.), or EMMenu (TVIPS, Germany), have been developed to extend or assist automated data collection at the microscope. In combination or alone (package dependent), they allow the automatic identification of specimen locations of interest and the collection of stacks of images or electron tomography tilt series comprised of stacks at each tilt angle based on initial manual input. This has greatly increased the output of electron microscopes, allowing them to record data for several days without interruption. However, because such sessions run day and night without the physical presence of an operator, a large number of unsuitable low quality images might be recorded for several hours, greatly reducing the productivity of the session. Ideally, the operator should be able to remotely monitor automated image acquisition and intervene from afar, if necessary. Software packages such as Leginon [Suloway et al., 2005] in combination with Appion [Lander et al., 2009], offer the possibility to remotely monitor some aspects of data acquisition. Here, we present an image-processing package called Focus that interfaces between cryo-EM data collection and data processing. Focus integrates software resources to

create a user-friendly environment optimized to carry out electron microscopy image analysis tasks in a high-throughput manner, and runs several jobs in parallel on a batch-queue processor to achieve this. It can be used to remotely monitor image acquisition and aims at real-time drift correction. Statistics calculated for the recorded and processed images are summarized in a "Project Library" for user inspection and data pruning, and uploaded to a web server when Focus is set to remotely monitor image acquisition. Focus simplifies the execution of tasks, such as "Motion Correction" with various software (Zorro, Unblur, MotionCor2) or "CTF determination". It can be run in four different modes: "Drift correction only"; "Single particle", which implements particle picking and exports data in a format compatible with RELION; "2D electron crystallography", which implements fully automated 2D crystal image processing directly within Focus; "electron tomography", which offers drift-correction for dose-fractionated electron tomographs with consideration of incremental dose accumulation and re-arrangement of recorded data from the so-called "Hagen Scheme" [Hagen et al., 2017] to "tilt-angle sorted" data. Additional functions and scripts can easily be added and integrated into the pipeline, by adding or editing C-shell or Python scripts, and by editing existing text files that define the set of available scripts or parameters. This allows to easily add scripts that call other third-party programs, as long as they can be reached via the command-line.

4.2 Implementation

4.2.1 Graphical User Interface

The Focus graphical user interface (GUI) was developed using C++ (C++11 standards) and its user interface is based on Qt5.x. The creation of a user-friendly platform was of utmost priority. The workflow and controls are sectioned into various panels accessible via the top navigation bar (Figure 4.1). These panels allow the user to perform processing tasks (in parallel if desired), manage images, view results and change settings. Graphical entities, such as icons, are used wherever possible. Processing tasks are accomplished either by precompiled executables or by python and shell scripts. Focus provides easy interaction to these executables and scripts (Figure 4.2) via a combination of (i) parameter files and form containers that receive the input and pass it on to the required place, (ii) scripts that call external executables such as MotionCor2, (iii) a log container and progress bar to monitor the processing, and (iv) result containers that show the output values and the images produced. Images can be inspected using a full-screen image browser.

4.2.2 Project structure

In Focus, a dedicated project folder is created on disk for each research project using the Project Wizard, and assigned one of the following modes: (i) drift correction only, (ii) 2D electron crystallography, (iii) single particle, or (iv) electron tomography. When a new project is initialized,

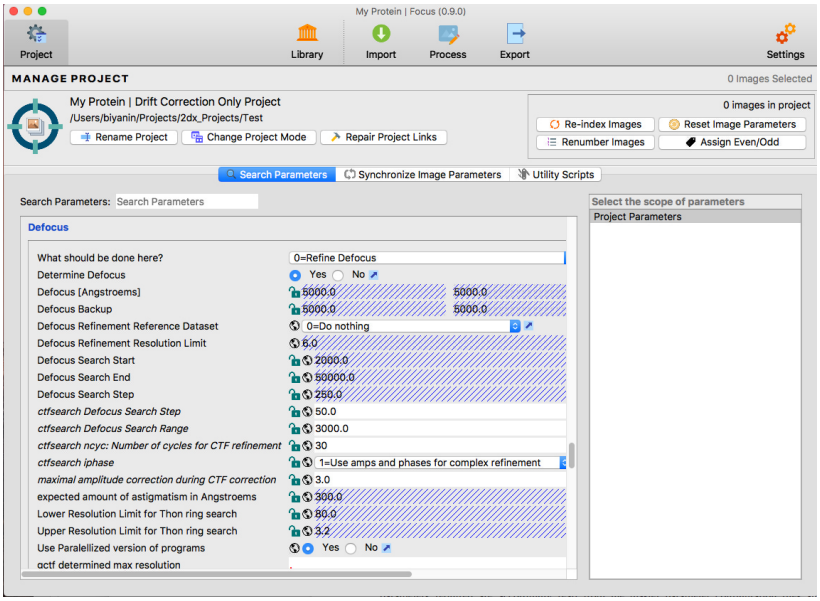

FIGURE 4.1. **Screenshot of the GUI:** Focus' GUI has controls divided into different panels. These panels are responsible to do all kinds of interaction with the software.

global parameters are established from a master parameter configuration file and stored in a project-level parameter file within this uppermost project folder (Figure 4.3).

Each project contains groups of images encapsulated on-disk as subdirectories. Each image-group folder contains a unique subfolder for every image and its associated metadata. This image-oriented subfolder organization allows Focus to interface with other image processing packages. Before data are exported for use in a different follow-up processing environment, the export function in Focus reorganizes them into the arrangement required by the target package. For example, if the target package is RELION, the data will be reorganized so that all aligned averages and a metadata STAR file are in a single subfolder. On the other hand, if the target package is IMOD [Kremer et al., 1996], the electron tomography data will be reorganized so that there is one MRC stack for each specimen location, containing the entire tilt series ordered by tilt angle, irrespective of the recording order (e.g., if they were acquired using the Hagen scheme [Hagen et al., 2017]; Section 4.4.4).

4.2.3 Scripts - the processing units

The processing functionalities provided by Focus are programmed in scripts that are responsible for specific tasks. The choice of available scripts offered to the user depends on the mode that Focus is operated in. Each script calls a few executables and fetches parameters associated with the project or the image as required. Depending on its scope, a script can run on the image level or the project level. Image-level scripts read and write image-level parameters (e.g., defocus for the image) and the work directory is the directory where the image is stored (Figure 4.3).

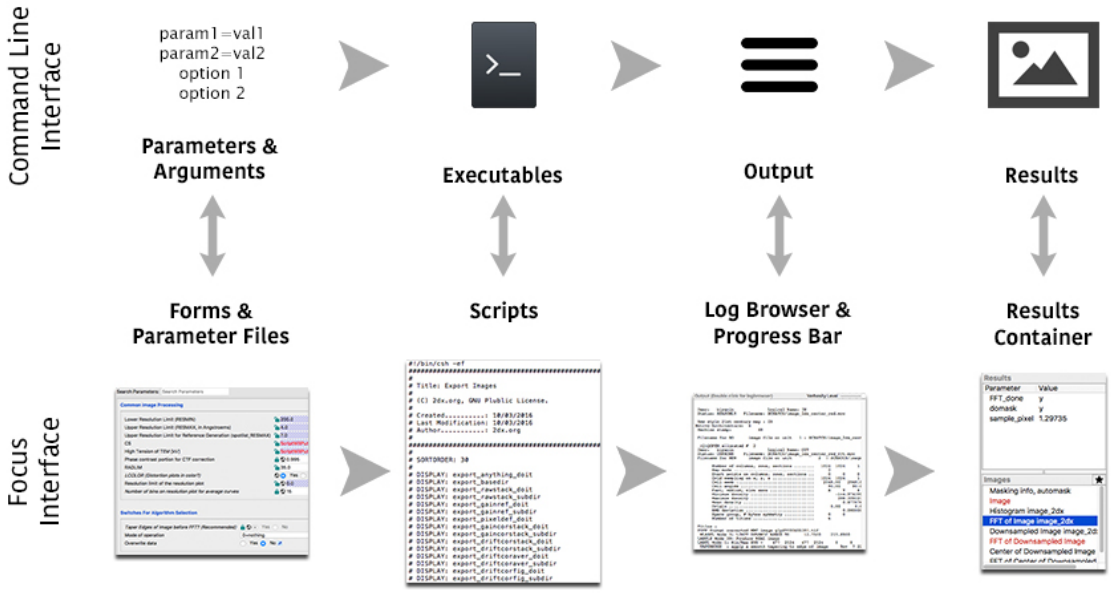

FIGURE 4.2. **The Focus Interface:** Focus provides a convenient interface to set parameters and arguments using forms and parameter files, run executables using scripts, check output using a log browser, and list important results using the results container.

Project-level scripts read and write project-level data (e.g., the binning method selected, or the defocus search range) and the work directory is a sub-folder of the uppermost project directory.

Unavailable user-defined tasks can be incorporated by creating new scripts. These have to be written in C shell (csh) and begin with a set of commented lines (starting with #) defining the properties such as title, manual for the script, parameters to use and parameters to display; existing templates give specific details. Afterwards, the required task, e.g., calling other executables or scripts, can be programmed in csh format. The parameters to be used, defined at the beginning of the script, are automatically read from the configuration files before the script is executed. Once placed in the appropriate folder (located in the installation directory subfolder "scripts"), new scripts immediately have read and write access to all images and parameters from the Focus database, appear in the GUI together with all other scripts in the folder, and can be run to process recorded image data.

4.2.4 Data processing pipeline

An overview of the workflow generally employed to prepare and process cryo-EM images or image stacks is shown in Figure 4.4. Focus provides an interface that allows many of these steps

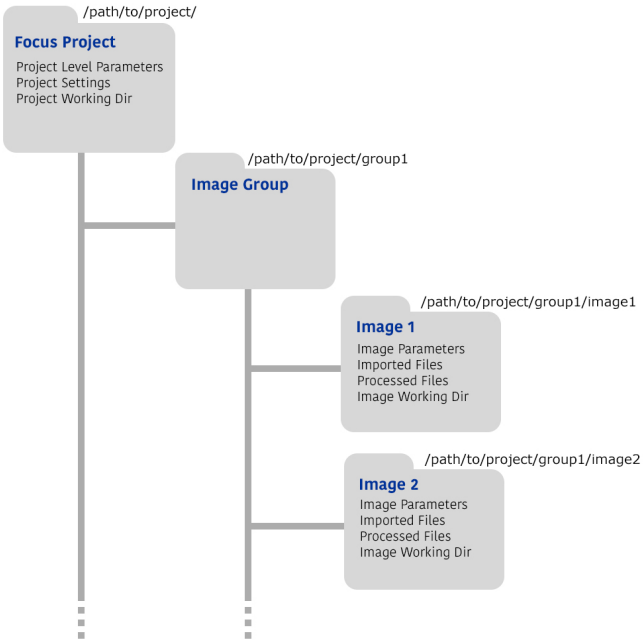

FIGURE 4.3. **Project Directory Structure:** Each Focus project resides in a separate directory on disk. This directory contains all project-level parameters and settings, and serves as the working directory for all project-level scripts. Images are divided into groups, and each group is a subdirectory of the project directory. Individual images are stored as subdirectories of the image group directories. The image subdirectories contain configuration files related to the image, raw files and processed files.

(Figure 4.4, gray box) to be linked in an automated pipeline. Functionalities such as image stack decompression and gain reference multiplication, Fourier cropping, drift correction, and CTF calculation are implemented in Focus scripts. In several cases, options allow users to choose which algorithmic strategy should be applied, e.g., which drift-correction software to use. Users can also easily implement external or their own software packages to execute a particular step (Figure 4.4), allowing considerable flexibility in the pipeline choice. For example, Fourier cropping can be performed using Focus' program fFourierCrop, IMOD's program newstack [Kremer et al., 1996] or FREALIGN's program resample_mp [Grigorieff, 2016]. Focus' fFourierCrop specifies a target pixel size, so that single particle data recorded at different magnifications or using different electron microscopes is scaled to the same pixel sampling via Fourier cropping or Fourier padding. Drift correction can be made using Zorro [McLeod et al., 2016], MotionCor2 [Zheng et al., 2016] or Unblur[Grant and Grigorieff, 2015]. CTF measurement and CTF resolution estimation can be obtained using the gCTF [Zhang, 2016]. Additional custom pipelines can be created by choosing the steps to perform and any additional scripts supplied by the user. For the latter shell or Python scripts analogous to existing scripts need to be created. When dropped into the

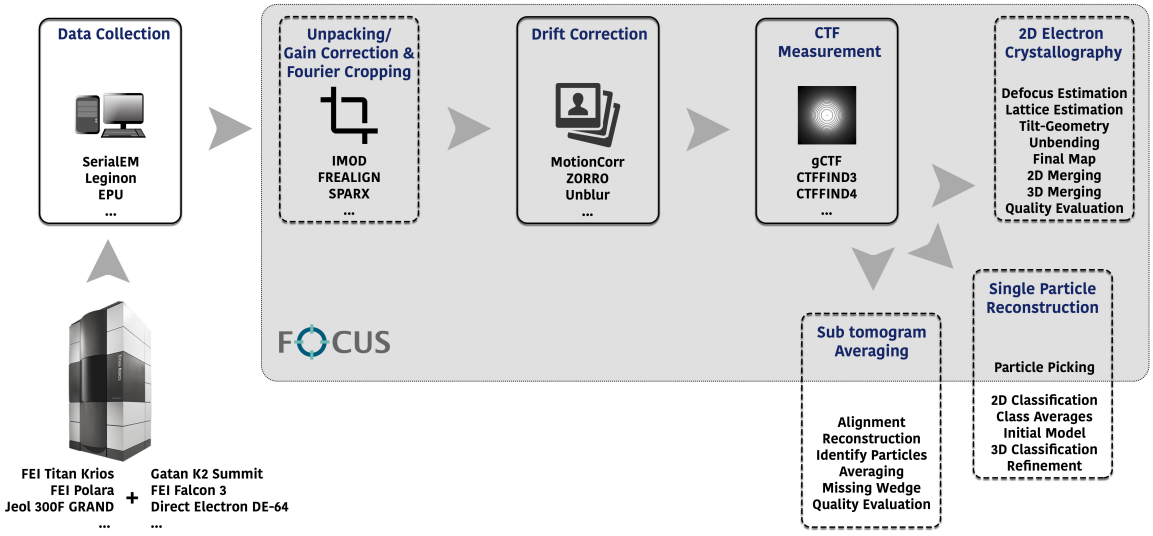

FIGURE 4.4. **Cryo-EM workflow and areas where Focus can currently be used:** A typical cryo-EM workflow involves the collection of data via automation software such as SerialEM, Leginon or EPU, followed by unpacking (if files were compressed), gain correction (if required), Fourier cropping (optional), drift correction of the collected image stacks and CTF correction using software utilities like gCTF. Afterwards, the workflow diverges depending on the nature of the project and the reconstruction method required. Focus can be used to carry out the steps indicated by the gray panel: including drift correction, CTF measurement, the whole 2D electron crystallography processing pipeline and particle picking for single particle analysis via gAutomatch (Unpublished: URL http://www.mrc-lmb.cam.ac.uk/kzhang/Gautomatch/). It currently provides an interface to the software packages indicated. Scripts for other processing can be added by users, and unique need-based workflows can be created.

appropriate folder location they will then have read and write access to all parameters from the Focus database and can be used to process recorded image data.

4.3 Features

4.3.1 Import Tool

The import procedure involves copying raw data files into the project directory, assigning and determining a set of parameters for each image, and optionally running one or several scripts for each image during or after import. This process is handled by the Import Tool (Figure 4.5). The tool can be configured to automatically fetch newly recorded stacks throughout the microscopy session from a network-mounted storage location. A delay timer can be set to ensure that half-written files are not copied; when Focus detects that the microscope has saved a new stack, the

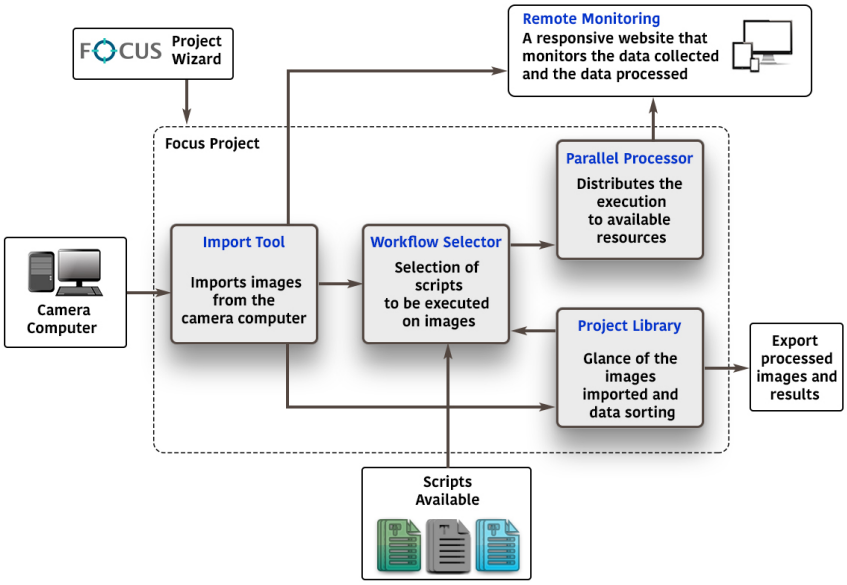

FIGURE 4.5. **Focus workflow:** (i) A project is created using the Project Wizard. (ii) Recorded images are imported to the project using the Import Tool. (iii) Processing workflows are created using the Workflow Selector and the scripts available. (iv) Images are processed using the Parallel Processor, which executes the selected workflow on all of the available resources and creates a log table. An overview of all imported images is provided by the Project Library. Data is continuously uploaded to a server so that the status of data collection and image processing can be viewed remotely. The processed images and results can be exported for further processing.

Import Tool waits for a specified safe time before copying. An option allows files to be deleted from the camera computer after import.

Using the tool, image data can be imported as dark-subtracted and gain-corrected images, or as dark-subtracted images only (in this case a separate gain reference file should be provided). Optionally, combinations of raw image stacks, and drift-corrected stacks, and drift-corrected and averaged 2D images, can be imported simultaneously.

The Import Tool allows a choice of scripts to be run on the imported data during import, which results in sequential processing of the data. This is required, e.g., if the incremental electron dose on the sample has to be computed for consecutively recorded image stacks within the same dose-fractionated tomography tilt series. The Import Tool also allows a choice of scripts to be submitted to the parallel batch queue for processing after import. This would apply, e.g., to computationally-intensive tasks such as motion correction and the subsequent steps. The batch-queue enables parallel processing, as discussed in the next section.

4.3.2 Parallel Batch-Queue Processor

The batch-queue processor allows images to be processed in parallel in a high-throughput manner. An image along with the processing workflow (a set of scripts) defines a batch. Processing batches are added to the processor queue in the order in which they are issued and processed with the policy of 'first come first served', i.e., the oldest batch is processed first. Alternatively, batches can be added to the top of the processing queue if the user wants to see the result for the most recently recorded image as soon as possible.

Processing batches can be submitted by the Import Tool so that a set of tasks such as unpacking, Fourier cropping, drift correction, CTF fitting, particle picking, and so on, are carried out on each freshly imported image. Processing batches can also be submitted manually from the Project Library (Section 4.3.3) by selecting a number of images and launching specific tasks for all of them. This is required, e.g., if already imported and processed images need to be processed again with different parameter settings. The processing order of scheduled tasks can be changed manually, if necessary.

The scripts that define a workflow can be selected from all scripts available at the image level. These scripts are divided into different categories; "Prepare Stack", "Drift Correct", "Calculate Statistics", etc. The selected scripts are executed in a specific order that cannot be changed manually. This order is defined by the processing logic that a workflow should observe. For example, the CTF is estimated on the drift-corrected image stack, thus the script cannot be run before drift correction. All calculated values are stored in the image-level parameter file.

Batches can be concurrently dispatched to the resources available on the system. If this setting is used, different processors are internally created and each processor is supplied with a different batch. These processors run in parallel. When a processor starts to run the scripts from its batch and processes a particular image it is marked as 'busy', and only becomes available again when all the scripts from the batch have been run. A log table that can be sorted by the processor id, image id, or the log time is maintained, allowing the processing progress to be monitored and any errors to be detected.

4.3.3 Project Library

The Project Library provides a summary of all images. These are listed in a tree structure according to the image group they belong to, with one image per horizontal line (Figure 4.6). Image statistics are shown in columns like in an Excel sheet; users can manually choose which parameters are displayed. The Project Library also displays a set of preview images for a selected image (a selected row in the table). These appear as thumbnails on the right of the table (Figure 4.6) and enlarge to full-screen display upon 'double-clicking'. The small PNG preview files employed are efficiently displayed when the user manually scrolls down over a large number of images. Different sets are available, depending on the mode in which Focus is run and the options selected (Appendix A, Table A.1). For example, the "Drift Overview" displays the 2D

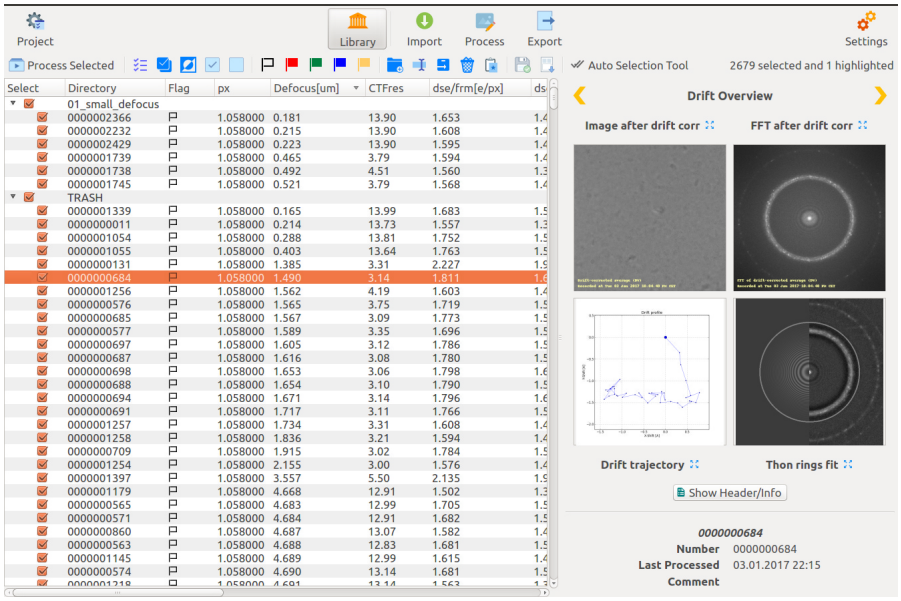

FIGURE 4.6. **Screenshot of the Project Library:** The Project Library provides an overview of all imported images and their image statistics (imaging and calculated). The interface allows the images to be sorted according to various parameters, such as defocus value, drift, etc. It can be used to manage images using colored flags and to divide them into specific image groups. Various views that allow the quality of an image to be assessed are provided. The "Drift Overview" shown provides four views: Image after drift correction, FFT after drift correction, drift trajectory and Thon rings fit. The thumbnails are for the image highlighted in the table and enlarge to full screen when selected (double mouse-click).

projected image stack and its FFT after drift correction, a drift trajectory plot, and the Thon ring fit (Figure 4.6).

A typical data collection session on a cryo-EM instrument results in thousands of image stacks, which Focus' Project Library can be used to organize and manage in different ways. Images can be sorted according to each column of the library table and, thereby, ranked by specific parameters such as mean pixel value, defocus, CTF resolution fit, amount of drift in the stack, or iciness of the sample. Sorting the Project Library in this way, allows a subset of images (image folders) to be selected based on specific image parameters (e.g., all images with too high defocus) by mouse-dragging, and moved to a different 'image group' folder (e.g., the TRASH folder) with one additional click. As TRASH is also ranked as an image group, trashed image folders are not permanently deleted and can be moved to other groups at any time. An unlimited number of image groups can be created. Image folders can also be flagged with specific colors, and sorted according to their flags; five different flag options are provided. The Project Library allows scripts chosen by the user to be launched on a subset of images selected by mouse, flag or group. This option is required, e.g., if some images need to be processed again with different

settings for drift-correction or CTF fitting.

4.3.4 Remote monitoring via a Web Server

The Focus software package can be used to continuously monitor image acquisition and microscope performance from afar during automated data collection. This remote, around-the-clock control allows performance errors to be detected and corrected during the recording session, saving valuable microscopy time.

When used in this way, Focus is configured to continuously push certain numerical parameters to a web server, decode the uploaded data and display them graphically for specific time intervals, e.g., the last 3 hours of data collection or longer time periods, allowing changes over time to be visualized (Appendix A, Figure A.1). The parameters include the mean pixel count of each stack (i.e., the average grey value), sample drift during stack acquisition (movie-mode recording), fitted amount of defocus, resolution of the CTF fit, and iciness. For example, decay of the mean pixel count over time is indicative of a drifting energy filter slit position or loss of beam alignment during the electron microscopy session, defocus values in an unexpected range correlate to problems in the focusing routine of the microscope, high drift could mean that there are problems with the sample temperature or mechanical instability of the specimen or microscope, and a high iciness value (i.e., the ratio of the intensity in the resolution band between 3.5 and 3.9 Å and between 80 and 30 Å, which gives a good estimate of the ice crystal content of the vitreous specimen) could indicate a slight warming of the sample (devitrification) or prevent the operator from running extended data collection sessions on insufficiently vitrified specimens. In addition, for the last recorded image, the website displays the 2D projected image stack and its FFT before and after drift correction, as well as the drift profile plot, and the CTF Thon ring fit. A blurred version of the image is shown, so that confidentiality is maintained if a webserver is openly accessible; the user still has sufficient information to remotely monitor and detect any problems in the data collection session. More than one microscope can be simultaneously monitored.

A configurable source code for the web server, written in HTML, CSS, Javascript, PHP and based on Bootstrap 3, is provided as part of the Focus source code. The website is responsive to screen size, and can thus be conveniently viewed on smaller mobile phone screens. The website also includes a JSON manifest profile that allows it to be added as a standalone application on Android and iOS platforms using Google Chrome and Safari's "Add to home-screen" feature.

4.3.5 Fast MRC viewer: fViewer

The MRC file format is most frequently employed to store electron densities in the field of electron microscopy. MRC files are binary files that store data in a three dimensional (3D) grid of voxels, each with a value corresponding to the electron density. The metadata are contained in the first 1024 bytes of the file and include properties like the size of the grid, cell size, etc. [Cheng et al., 2015]. Images with ~8,000 pixels in a single dimension stored in the MRC format take some time

to read. The fViewer implemented in Focus was specifically designed to read and display this type of large file. It reads the data in parallel threads, which greatly decreases the time required. For example, it takes ~250 milliseconds to read and display a 3838 x 3710 pixel image on a standard MacBook Pro laptop with 4 cores, making visual inspection of the images very time-efficient.

fViewer provides various display options or functions, e.g., to scale the displayed image and zoom in or out. The contrast can easily be adjusted using keyboard shortcuts. For real images, a selection-based FFT is provided so that the Fourier transform of a selected image region or the whole image can be quickly inspected. For Fourier images, the defocus-dependent Thon rings can be displayed as overlays, and the resolution at a particular voxel can be checked. Other additional features depend on the project mode (Appendix A, Table A.2). For example, particles picked for single particle projects can be viewed.

4.4 Application-specific workflows

The workflows, scripts, and visualization tools available within Focus depend on the image processing tasks required, i.e., on the Project Mode selected, as described below and summarized in Figure 4.4.

4.4.1 Mode: Drift Correction Only

This basic workflow includes unpacking, if the raw images are compressed TIFF files, optional gain correction using IMOD [Kremer et al., 1996], optional Fourier cropping using IMOD, FREALIGN [Grigorieff, 2016] or internal program fFourierCrop, and drift correction using Zorro [McLeod et al., 2016], MotionCor2 [Zheng et al., 2016] or Unblur [Grant and Grigorieff, 2015].

4.4.2 Mode: 2D Crystals

Focus includes the scripts and programs previously available within the 2dx software package [Gipson et al., 2007a,b]. Processing images of 2D crystals is computationally cheaper than single particle analysis and reconstruction, and can be done during data collection in a highly automated manner. The complete pipeline of 2D electron crystallography processing scripts, including lattice determination, spot selection, and final map generation, can be executed without user intervention. The final map and other processing data are displayed for each image if the Project Library is set to show the “Processing Overview” (Appendix A, Table A.1). When launched in 2D electron crystallography mode, Focus also allows the processed 2D crystal images to be merged and a 3D reconstruction to be generated.

4.4.3 Mode: Single Particle

The scripts and visualization tools offered by Focus in the “Single Particle" mode interface manual or automated data collection on a cryo-EM instrument with subsequent single particle data processing on remote computer clusters, which is generally carried out using RELION [Scheres, 2012], FREALIGN [Grigorieff, 2016], EMAN2 [Ludtke, 2016; Tang et al., 2007] at present. A typical workflow in this mode consists of: the “Drift Correction Only” workflow plus CTF estimation, detecting particle locations, followed by submission of image statistics to the web server.

As detailed in Section 4.3.3, data are presented in the Project Library with parameter sets that enable efficient data pruning; images with extreme grey values (too bright due to broken carbon film or too dark due to highly thick sample), defocus, iciness, or drift can be efficiently recognized and removed from the image group folder. With the help of the EXPORT function in Focus, the remaining images can be reorganized and transferred together with appropriately formatted metadata for subsequent single particle processing on a different computer.

4.4.4 Mode: Electron Tomography

In “Electron Tomography” mode, Focus offers a set of scripts to deal with recorded tomography tilt series. Tomograms can be acquired following the sequential tilt angle scheme (starting at one tilt angle, and incrementally progressing towards the final tilt angle) or the Hagen scheme [Hagen et al., 2017] (starting with non-tilted images, and incrementally progressing to higher tilts while alternating positive and negative tilt angles). At each tilt angle, image data can be recorded as a dose-fractionated image stack. This means that, e.g., a tilt series covering 121 tilt angles from -60° to +60° in 1° steps recorded from one specific specimen region using the Hagen scheme, would consist of 120 dose-fractionated stacks, ordered in the sequence 0°, 1°, -1°, -2°, +2°, +3°, -3°, -4°, and so on. Further, as electron doses vary in a $1/cos(angle)$ scheme to compensate for different sample thickness at different tilt angles, the number of frames per dose-fractionated stack varies. Focus is designed to recognize the specimen identity number or name, and the tilt angle, if this is encoded in the file name. Imported image stacks acquired from the same specimen location are imported to their own specific image group. Focus can then unpack recorded image stacks, evaluate the number of frames and calculate the per-frame and total electron doses for each, while other tilt angle stacks are being acquired and imported. Afterwards, the image stacks are submitted to the batch queue for drift-correction, taking into account the prior dose on the sample before each frame in the stack was recorded. The prior and momentary electron doses experienced by the sample are needed for appropriate electron-dose dependent B-factor resolution filtering during drift-correction [Grant and Grigorieff, 2015]. For each tilt angle, drift-corrected and B-factor filtered frames are then averaged into one 2D image.

In this mode, the export function in Focus allows the drift-corrected and averaged image files to be reorganized according to tilt angle, and combined in one MRC image stack, in which

each frame corresponds to one tilt position, ordered by tilt angle. In the example above, image stacks recorded at angles 0°, 1°, -1°, -2°, +2°, +3°, -3°, -4°, …, would be exported as one MRC file containing frames ordered by the angles -60°, -59°, -58°,…, 0°, …, +59°, +60°.

4.5 Software speed performance

To assess the speed and performance, Focus was installed on an Ubuntu PC equipped with 24 cores, resulting in 48 threads, 256 GB of RAM, a fast PCIe SSD for scratch data, and 70 TB of hard-drive disks under RAID5 management. The machine additionally had 2 Nvidia GeForce GTX 1080 GPU cards installed, each having 8 GB of video memory. It was situated next to the data collection PC of the microscope. Data were collected on an FEI Titan Krios equipped with a Gatan Imaging Filter (GIF) and a Gatan K2 Summit direct electron detector, using SerialEM [Mastronarde, 2005] version 3.6. Recorded image stacks were saved as dark-subtracted LZV-compressed TIFF files that contain integer electron counts, accompanied by two separate files that store the pixel defect list as a text file and a gain reference image as floating point values. With this setting, SerialEM recorded one dose-fractionated image stack and saved it as a compressed TIFF file containing 80 frames at super resolution (8k mode), every 65 seconds.

The images were imported into Focus during data collection. Images were automatically fed to the parallel batch queue processor, and processed using the following pipeline: Stack unpacking using IMOD's clip [Kremer et al., 1996], Fourier cropping of 8k frames to 4k frames using FREALIGN's resample_mp [Grigorieff, 2016], drift correction using MotionCor2 [Zheng et al., 2016], CTF measurement using gCTF [Zhang, 2016], particle picking using gAutomatch (Unpublished: URL http://www.mrc-lmb.cam.ac.uk/kzhang/Gautomatch/), calculation of various image statistics, and publication of these on the web server. The batch queue was set to process ten jobs in parallel. Under these conditions, the processing was always ahead of the recording speed, i.e., unpacking, Fourier-cropping, drift-correction, CTF measurement, and particle picking took on average less than 65 seconds. Producing dark-subtracted compressed TIFF files allows the data to be saved in a very compact, disk-space saving manner, even though unpacking and gain-correcting the TIFF files introduces an additional step to the workflow. As some of the chosen programs run on CPUs and some on GPUs, the load was divided between them, which meant that more tasks could be completed within a given time. The status of data collection and processing was continuously uploaded to the website: http://status.c-cina.unibas.ch/ (Appendix A, Figure A.1), allowing the user to monitor the microscopy session and take action if required.

4.6 Discussion

Focus integrates software resources to create a user-friendly environment that allows the tasks and processes of electron microscopy data processing to be carried out in a high-throughput manner. It features tools such as a parallel batch-queue processor that can be used for high-

throughput processing, a configurable website for remote monitoring, and a project library that can summarize image statistics and provide several overviews of the image. Focus implements ready-to-use scripts with easy parameter handling, and can be customized with additional scripts as required. When Focus is supported by the appropriate hardware, the image processing speed is faster than the recording speed.

Focus can be installed on a Linux or macOS system, and can run and complete image processing tasks in parallel to image acquisition. The overview of the images provided by the project library is continuously updated, and the performance of the recording session can be monitored using time series of mean intensity values, drift, defocus and resolution on a web server (Appendix A, Figure A.1). During or after the data collection session, images can be organized or moved to a TRASH folder (data pruning), and remaining images can be exported to another hard drive or network location together with the processing results in the form of customizable metadata files, such as for example STAR files prepared for subsequent processing, e.g., with RELION [Scheres, 2012] for single particle datasets.

Often, processing parameters need to be determined and optimized using a small set of high-quality images before they are applied to the rest of the dataset. Focus supports this type of operation, as images can easily be divided into groups, for which specific tasks can be run again by submission to the batch queue. For instance, parameters like particle diameter, box size, cross-correlation cutoff, have to be optimized when particles are 'picked' for single particle projects. In this case, one could sort the acquired images by parameters such as defocus, to select a set of images, for which particle picking is then launched again with specific optimized parameters, which then could also be used as default values for subsequently imported images.

Focus for macOS (10.10 or higher) and Linux (Ubuntu/Fedora/Redhat) can be downloaded from the website: http://www.focus-em.org. The source code is available under the Gnu Public License (GPL) at Github: http://www.github.com/C-CINA/focus.

PART III

HIGH RESOLUTION 2D ELECTRON CRYSTALLOGRAPHY

CHAPTER 5

IMAGE PROCESSING TECHNIQUES FOR HIGH RESOLUTION 2D ELECTRON CRYSTALLOGRAPHY

The following chapter is a part of the submitted manuscript:

Image processing techniques for high-resolution structure determination from badly ordered 2D crystals
*Nikhil Biyani**, Sebastian Scherer*, Ricardo Righetto, Julia Kowal, Mohamed Chami and Henning Stahlberg.
* *equal contribution*

in

Journal of Structural Biology.

Contribution:
Development of some algorithms and adaptation to the user-friendly environment; image processing of the dataset, final map generation

Abstract

2D electron crystallography can be used to study small membrane proteins in their native environment. Obtaining highly-ordered 2D crystals is difficult and time-consuming. However, 2D crystals diffracting to only 10-12 Å can be prepared relatively conveniently in most cases. We have therefore developed image processing algorithms allowing to generate a high resolution 3D structure from cryo-EM images of badly ordered crystals. These include movie-mode unbending, that corrects for crystal imperfections and locally-varying beam-induced sample deformations, while preventing over-fitting and computationally optimizing the electron dose used for each resolution range individually; refinement over sub-tiles of the frames in order to locally refine the crystal tilt geometry and electron beam tilt within different tile locations on the images; analysis of various CTF correction schemes to improve amplitudes and phases. We applied the new procedure to a three-dimensional (3D) dataset consisting of ~400 images of the voltage-gated ion-channel MloK1 crystallized in 2D. The 3D density map and its quality measurements improved significantly. The refined map shows more distinct densities than the 3D reconstruction obtained by classical crystal unbending and is easier to interpret.

Keywords:
Direct electron detector; Gatan K2 Summit; Movie-mode processing; Dose-fractionation; Membrane proteins; Electron crystallography; Tiled image processing; CTF correction

5.1 Introduction

Direct electron detectors (DEDs) equipped with a radiation-hardened complementary metal-oxide-semiconductor (CMOS) sensor [Bammes et al., 2012; Glaeser et al., 2011; Milazzo et al., 2011] tremendously increase the signal-to-noise ratio (SNR) of cryo-electron microscopy images. Instead of converting incoming electrons into light via a scintillator, these new devices detect them directly, which significantly reduces detector background noise. Beside the superior detector quantum efficiency (DQE) of DEDs [Ruskin et al., 2013], this new generation of detectors feature an enhanced sensor readout frequency. This makes it possible to perform counting of single electrons, resulting in recording of images with minimal dark background signal. This along with the fast readout speed allows to record image frames within exposure times that are short enough to prevent physical drift of the specimen stage. Consequently, movies of the sample can be recorded while it is continuously exposed to the electron beam. Algorithms like Zorro [McLeod et al., 2016], MotionCor2 [Zheng et al., 2016] efficiently measure and correct for translational offsets between dose-fractionated movie-frames recorded on DEDs. The impact of sample movements such as those caused by specimen stage-drift, can thereby be strongly reduced, which increases the efficiency of data acquisition significantly. These new hardware and software developments have led to several recent breakthroughs in high-resolution cryo-EM 3D structure determinations that reach and surpass atomic resolution [Liu et al., 2016; Merk et al., 2016; Yu et al., 2016]. Thus, cryo-EM has become a powerful and fast method for atomic-resolution protein structure determination.

2D electron crystallography is a branch of cryo-EM that is used to determine the electron density maps by imaging 2D crystals of desired biological structures [Stahlberg et al., 2015]. 2D electron crystallography is advantageous as: (i) the hydrophobic core is contained in the lipid bilayer providing a more native environment to the membrane proteins, (ii) it can be used to study proteins that are small in size, and (iii) the image processing is quite automated [Scherer et al., 2014b]. Creation of homogeneous sample with high crystallinity becomes quite important to generate high resolution structures in 2D electron crystallography. Obtaining highly ordered crystals is tedious and time consuming which involves testing stability in various detergents along with varying conditions. However, 2D crystals diffracting to only 10-12 Å can be prepared relatively conveniently in most cases.

Besides sample quality, beam-induced specimen movement further reduces the crystalline order, especially when the images of highly tilted 2D crystal samples are to be recorded [Glaeser et al., 2011]. The behavior of the sample under the electron beam was investigated in multiple studies [Bai et al., 2013; Brilot et al., 2012; Campbell et al., 2012; Glaeser et al., 2011; Veesler et al., 2013]. By analyzing virus or ribosome particles during the exposure, these studies reported locally correlated movements that differ among the particles of an image. It is commonly believed that these local movements are due to irreversible deformations of the ice layer and also the sample, caused by the electron beam [Brilot et al., 2012]. The amount of beam-induced motion

depends on the microscope settings and the properties of the sample and grid. For 2D crystals, Glaeser et al. proposed firmly attaching the crystals to an appropriate strong and conductive support in order to overcome beam-induced sample movements [Glaeser et al., 2011]. However, such treatment may not be optimal for membrane proteins that show structural alterations when adsorbed to carbon film. A more general approach is to allow the 2D crystal membrane to move under the beam, and then computationally retrieve the structural data from recorded movies. Here, algorithms accounting for universal motion of all movie-frames, e.g., caused by stage drift, cannot correct for spatially varying beam-induced motion as they neglect locally varying movements within the frames. An image processing approach that locally treats sub-regions of a 2D crystal sample in each movie frame is needed.

Another resolution-limiting factor is electron beam-induced radiation damage. A high cumulative electron dose destroys fine structural details, whereas a low cumulative electron dose preserves the high-resolution information but reduces the SNR of the recorded image. Before detectors capable of movie-mode imaging were available, the full electron dose was captured within one single image and the EM operator had to carefully choose the electron dose depending on the target resolution. In 2010, before the advent of DEDs, Baker et al. recorded dose-fractionated image series of crystals and analyzed the resolution dependent vanishing of computed diffraction spots. Their findings suggest to record dose-fractionated image series of the sample and add these frames together using resolution-dependent frequency filters, in order to optimally exploit each image frequency at its maximal SNR [Baker et al., 2010].

The fact that a 2D crystal contains many regularly arranged identical copies of the same protein, allows electron crystallography to improve the SNR by using Fourier-filtering methods. Processing individual micrographs of 2D crystals generally involves the following six steps [Arheit et al., 2013]: (i) Defocus and (ii) tilt-geometry estimation, (iii) lattice determination, (iv) correcting for crystal imperfections, termed unbending, (v) Fourier extraction of amplitude and phase values from computed reflections, (vi) Contrast transfer function (CTF) correction and (vii) generating a projection map of one unit cell at higher SNR. So far, this procedure was applied to the drift-corrected average gained from a movie-mode exposure of a 2D crystal and thus did not account for locally varying beam-induced sample movements. Additionally, the CTF determination and correction is done after the unbending procedure. With the images obtained from new detectors, Thon rings up to 3 Å can be correctly identified. GCTF [Zhang, 2016] can quickly and precisely calculate the CTF and defocus on GPUs. This creates a possibility to correct the CTF as a preprocessing step before the unbending procedure.

In this study we developed image processing algorithms and techniques allowing to generate a high resolution 3D structure from cryo-EM images of badly ordered crystals. These include: (i) movie-mode unbending that corrects for locally varying beam-induced sample deformations and computationally optimize the electron dose for each frequency, along with reducing the risk of overfitting the data at low SNR, (ii) tiled image processing, by dividing it into sub-images called

tiles, minimizes the artifacts that arise due to the use of same tilt angle for the whole image, and (iii) analysis of various CTF correction schemes for 2D-electron crystallography with the aim of increasing resolution. The new procedures are implemented as additional scripts in Focus (Chapter 4) and are available for download at www.2dx.org or www.focus-em.org. We present the application of the new techniques to an experimental dose-fractionated membrane protein dataset recorded on a FEI Titan Krios equipped with a Gatan K2 summit detector, which yielded an improved 3D reconstruction of the ion-channel MloK1.

5.2 Theory

5.2.1 Tilt geometry definition in 2D electron crystallography

The tilt geometry of a 2D crystal is in electron crystallography parameterized with the variables $TLTAXIS$ and $TLTANG$. The MRC image convention has the first point of the image in the lower left corner indexed as $[0,0]$, with the X-axis pointing right and the Y-axis pointing up. $TLTAXIS$ defines the orientation of the sample tilt axis, measured from the horizontal X-axis (pointing right in the image) to the tilt axis with positive values meaning counter-clockwise. $TLTAXIS$ is defined as between -89.99999° (pointing almost down) and +90.0° (pointing straight upwards). $TLTANG$ defines the tilt angle of the specimen, and can take any value between -89.999 and +89.999°. If the $TLTAXIS$ is horizontal and underfocus in the image gets stronger further up in the image (i.e., at locations with higher y coordinates), then $TLTANG$ is positive.

In electron crystallography, the tilt geometry from the point of view of the 2D crystal is defined by the parameters $TAXA$ and $TANGL$. $TAXA$ is the relative rotation of the unit cell of the given 2D crystal in 3D Fourier space, and $TANG$L is equal to $TLTANG$, but its sign alters depending on the orientation of the crystal on the tilted specimen plane, or the handedness of the assigned lattice vectors [Arheit et al., 2013]. These parameters $TAXA$ and $TANGL$ are only relevant for 3D merging in electron crystallography, and are not further discussed here.

Other software packages such as SPIDER [Leith et al., 2012], FREALIGN [Grigorieff, 2016; Leith et al., 2012], EMAN2 [Ludtke et al., 2009] or RELION [Scheres, 2012] define the tilt geometry differently. The relationship between the electron crystallography tilt geometry adopted in the 2dx and MRC packages, and the SPIDER convention of Euler angles adopted in many single particle reconstruction packages, is the following:

$$\psi = 270.0^\circ - TLTAXIS \tag{5.1}$$

$$\Theta = TANGL \tag{5.2}$$

$$\Phi = 90.0^\circ - TAXA \tag{5.3}$$

5.2.2 Tiled image processing

Imperfect crystals contains in-plane as well as out of plane distortions. The unbending procedures can correct, at best, the in-plane distortions and are not able to capture out-of-plane distortions that occur in the crystal. These distortions, especially in tilted images, can lead to wrong densities and in turn become a hindrance to the achievement of high resolution structures. Due to these distortions, the tilt geometry, beam tilts and defocus may differ in different parts of the image. The changes in tilt geometry and defocus are more serious; beam tilts are only of concern when targeting a resolution better than 3 Å.

To minimize these effects, the image is subdivided into smaller parts called tiles. The subdivision, ideally, should target tile size that is small enough to identify the correct local tilt angles throughout the image. But a smaller tile will have less signal-to-noise ratio and becomes insignificant in 3D reconstruction. So the size of the tile should be chosen such that there is enough signal in the image. To reduce the Fourier artifacts that arise due to the cut, the tiles are forced to have overlapping Gaussian smoothed edges. Once the image is properly divided into tiles, each of these tiles are considered as individual images (Figure 5.1) and parameters related to tilt geometry and defocus are recalculated followed by other steps that lead to the generation of the final map (Figure 5.1). This approach is computationally demanding; to increase the efficiency, recalculation of parameters such as defocus can be search limited with an initial guess that equals the value corresponding to the whole image. The implication of using tiles is that a lot more data (final projection maps) that has locally optimized parameters is generated. The signal in each of these maps might be low, but averaging a large number of them, when 3D merging, leads to better reconstructions.

5.2.3 CTF correction strategy

Correction of the Contrast Transfer Function (CTF) of the electron microscope is necessary in order to restore structural information, especially at higher resolutions, that would otherwise be lost during the image processing and merging steps. In the absence of beam-tilt and in case of parallel illumination, the electron microscopy projection of the biological structure in the image is convoluted in real-space with the point-spread function (PSF) of the microscope, which is equivalent to a multiplication of the Fourier transformation of the image with a real-valued CTF function. In case of beam-tilt or non-parallel illumination, the PSF in real space has resolution-dependent delocalization features, or the CTF in Fourier-space becomes a complex-valued function. The effects of this are not further discussed here.

The real-valued CTF shows oscillatory rings, called Thon rings [Thon, 1966], which refer to the maxima of the CTF, which are interrupted by zero-crossings of the CTF. Their diameter depends on the applied defocus under which the image was recorded. In case of a tilted sample, that defocus varies across the image, as quantified by $TLTAXIS$ and $TLTANG$. A reliable

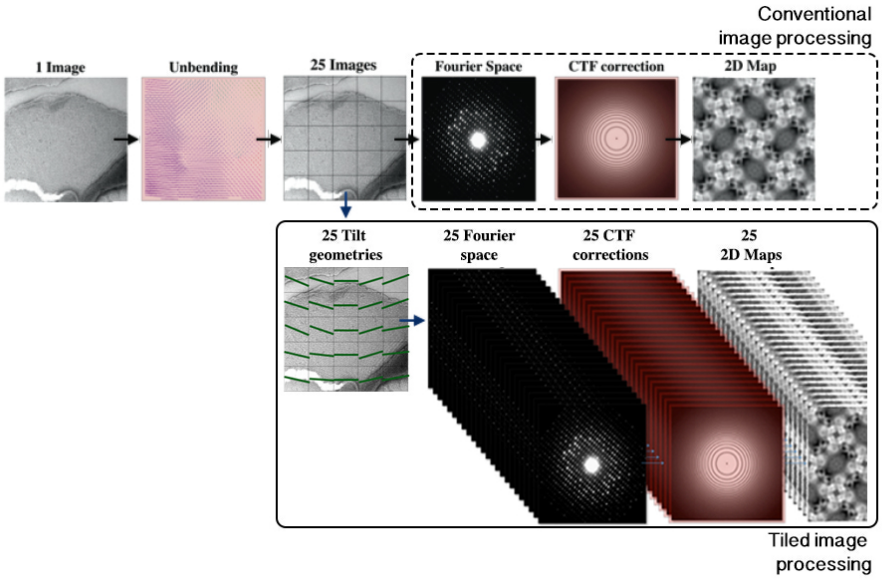

FIGURE 5.1. **Tiled image processing scheme:** When crystals are not flat the parameters like tilt-geometries and defocus vary along the image. To reduce this problem, images are divided into various overlapping tiles and the tiles are individually processed to get many 2D maps instead of one.

measurement of the tilt geometry and also of the magnification is therefore mandatory to be able to fully correct for the effect of the varying defocus.

The tilt geometry is in a first step determined by evaluation of the defocus gradient, as described in detail in [Arheit et al., 2013]. This measurement takes the current definition of the pixel size into account. If for example that pixel size was quantified 1% too small, then the defocus measurement in the corners of the image will be assigned to locations too far apart from each other, which results in an underestimation of the tilt angle ($TLTANG$). As a result, the determined 3D reconstruction would be too short in the z direction, and too wide in the x and y directions.

The tilt geometry is refined in a second step, based on the distortions of the measured 2D crystal lattice, and its deviation from the non-tilted 2D crystal lattice. This will only give reliable measurements for specimens at higher tilts (i.e., $TLTANG > 25°$). In a third step, the tilt geometry is refined during merging, by comparing the amplitude and phase data from each image with the current 3D reconstruction. This measurement of the tilt geometry can be separately done for different parts of the image by dividing it into tiles, as discussed in the previous section.

All these tilt geometry refinement steps are unable to detect or eliminate the consequences of a wrong pixel size. As long as data are evaluated as amplitudes and phases as a function of Miller indices, the errors in the pixel size are not detectable. The advantage of this is that data from different microscopes, recorded with different pixel sizes, can easily be combined. However, the

disadvantage is that an isotropically magnified 3D reconstruction cannot easily be obtained: Final maps are often too wide in x and y, and as a consequence too short in z, or the opposite. Only, when real-space single particle methods are used to combine datasets of tilted 2D crystals into a 3D reconstruction, then an isotropically magnified reconstruction can be constructed. Alternatively, the isotropic scaling of the final 3D reconstruction can be recognized, if sufficient resolution is reached to fit the pitch of alpha-helical structures in the final map to expected biological values. This, however, requires a final 3D resolution of better than 4.5 Å.

5.2.3.1 CTF correction methods

CTF correction can be done by simple phase-flipping (phases of Fourier pixels on odd-numbered Thon rings are incremented by 180°, so that the phases are corrected but the amplitude oscillations in the original data remain), or by CTF multiplication (the Fourier pixels are multiplied with the CTF pattern ranging from -1 to +1, so that the phases are corrected but the amplitude oscillations in the original data are now even more exaggerated), or by Wiener filtration (the Fourier pixels are multiplied by $\frac{CTF}{CTF^2+N^2}$ so that the phases are corrected, and the amplitudes are partly re-established to their correct values. Here, N is a noise term that depends on the SNR of that image segment. A value of $N = 0.3$ gives conservative results in practice.).

5.2.3.2 TTF correction

Henderson et al. introduced the correction of the "tilted transfer function" (TTF), by first unbending the 2D crystal images, then Fourier transforming the unbent image, and convoluting the Fourier transform for each lattice spot with a pattern that represents the expected split spot profile at that location [Henderson et al., 1986]. Only after convolution, the amplitude and background values are evaluated. This so-called TTF correction effectively eliminates all effects of the defocus gradient across the image. Effects of beam tilt have to be addressed during 3D merging later. Effects of non-parallel illumination (i.e., coma) cannot be corrected with this method. Effects of a varying tilt geometry throughout the image (e.g., from a bent 2D crystal plane) also cannot be addressed with this method.

5.2.3.3 CTF correction in stripes before unbending

We have developed software to correct the effect of the varying CTF in the real-space image before unbending. This is done by correcting the image with a static CTF profile by multiplication in Fourier space, and extracting only a narrow stripe in the direction of the tilt axis at the image regions, where that CTF agrees with the local defocus. Assembling various such stripes eventually produces the fully, locally CTF corrected output image. The number and the width of the stripes is thereby calculated as a function of the tilt angle and the desired resolution: The higher the target resolution, the more narrow and more frequent are the stripes of independently

CTF-corrected image segments. Any effect of beam tilt is not considered, and would have to be addressed during 3D merging.

5.2.3.4 CTF correction before or after unbending?

CTF correction can be done before 2D crystal unbending, or after unbending, or in a combination of both. CTF correction before unbending has the advantage that delocalized features from extended point spread functions in the real-space image are moved to their correct locations before the crystal unbending moves them around. If unbending is instead done first, followed by CTF correction later, the unbending step risks to cut the ripples of the PSF, thereby loosing high-resolution data. For badly-ordered 2D crystals, this problem could become limiting. CTF correction before unbending by Wiener filtration, on the other hand, reduces the SNR in the image, so that the unbending step cannot as reliably determine the crystal order defects.

5.2.3.5 Hybrid CTF correction

We have implemented a so-called "Hybrid CTF correction" algorithm, where the original image is corrected in two different versions in stripes for the varying CTF across the image: Once by CTF multiplication, and a second time by CTF Wiener filtration. The first has a maximized SNR of the biological structures, and is ideal for determination of the crystal defects and the unbending profile. This unbending procedure determined on the CTF-multiplied image is then instead applied to the CTF Wiener-filtered image. This results in a Wiener-filtered and then unbent image, for which the unbending profile was determined at optimal contrast.

5.2.4 Movie-mode unbending

2D crystal images show different local movements within regions of a single 2D crystal during imaging (Figure 5.2). We observed local relative movements of up to 40 Å within micrometer-sized 2D crystal regions during the exposure required to record a movie (typically featuring a total dose of 40 electrons/Å^2 distributed over 40 frames). This observation underlines the need for per-frame movie-mode image processing for high-resolution electron crystallography.

The fundamental idea of movie-mode unbending is instead to process each frame of a movie individually and thereby correct for beam-induced crystal distortions that occurred while the image stack was recorded. This involves (i) correctly exploiting the smooth motion of consecutive frames, (ii) accounting for radiation damage during the increasing exposure, (iii) dealing with the extremely low SNR of one movie-frame, and finally (iv) preventing overfitting. Again, the use of global factors alone is not sufficient.

The classical unbending procedure is briefly described here followed by the explanation of two alternative movie-mode unbending algorithms, as schematically detailed in Figure 5.3. The algorithm starts with the conventional unbending of the whole-frame drift-corrected and aver-

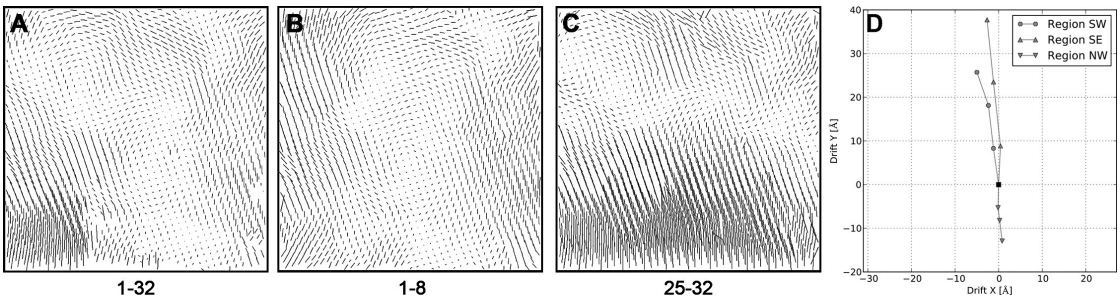

FIGURE 5.2. **Electron dose dependent variation of distortion-vector ERROR-fields showing the necessity of beam-induced motion-correction:** (A) Unbending profile (4k × 4k pixels) obtained by processing the average image generated by real-space averaging of 32 movie-frames (out of the recorded 40 frames, after discarding the first two and the last 6 frames). For display purposes, the motion vectors have been elongated ten times. By instead only averaging eight subsequent frames, we obtained a new movie consisting of only four super-frames, showing the crystal at different exposure times (averaging frames 1-8, 9-16, 17-24, and 25-32, after discarding the first two and the last 6 frames). These four resulting averaged super-frames were then individually unbent with the algorithm described as MovieB. The distortion-vector ERROR field of the first average (frames 1-8) is shown in (B), the one for the fourth average (frames 25-32) in (C). (D) Drift-profiles quantifying the averaged local movements over the whole sequence of super-frames relative to the first frame average. Fifty neighboring trajectories were averaged for each quadrant of the images. The drift of the northeast quadrant of the crystal was omitted because of visualization difficulties due to negligible local drift (< 2 Å). The lower area (southern quadrants) of the crystal is drifting upwards during the exposure, whereas the movements of the upper part are smaller and in another direction. An approach that corrects for sample movements at frame level by translationally aligning entire frames is not able to correct for such inhomogeneous and electron dose-dependent local crystal deformations.

aged single image, using the conventional Unbend2 algorithm. During this step, an unbending reference (termed "Ref." in Figure 5.3a) and also an unbending profile are determined.

5.2.4.1 Classical unbending procedure

The central step in the processing of one single image of a 2D crystal is correcting crystal imperfections, termed unbending [Arheit et al., 2013]. A Fourier-filtered reference is generated based on the crystallographic lattice determined in reciprocal space, and cross-correlated with the micrograph. Peaks in the resulting cross-correlation profile (localized by the MRC program $Quadserch$) correspond to crystallographic unit-cell locations. The MRC program $CCUnbend$ is subsequently used to translationally adjust small patches (e.g., 25×25 pixels in size) of the micrograph to maximize the regularity of the crystal in order to achieve high-resolution projection maps. The image unbending is usually refined over several rounds, resulting in an improvement

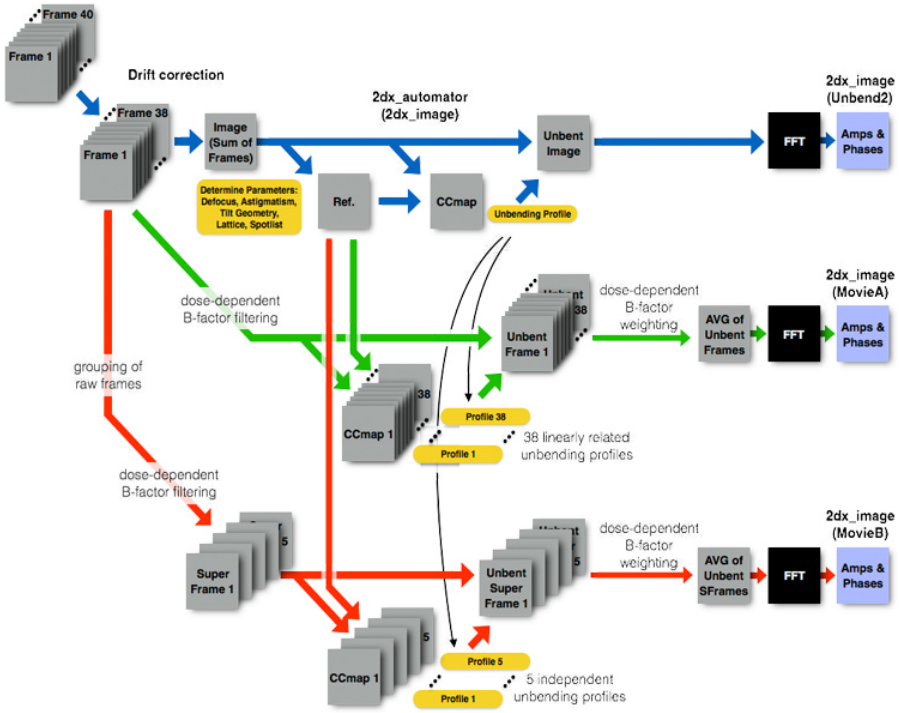

FIGURE 5.3. **Movie-mode unbending algorithms:** The recorded image stack of 40 frames is whole-frame drift corrected. Here, the first two frames are typically discarded due to elevated drift. (A) The remaining 38 frames are averaged and the single, resulting image is conventionally processed by unbending with 2dx_automator (top branch), resulting in the dataset termed "Unbend2" result. (B) A movie-mode processing algorithm termed MovieA is then applied to the whole-frame drift-corrected stack. MovieA unbends each of the remaining 38 frames individually, using as unbending reference the reference from the Unbend2 branch (labeled "Ref."). In order to be less sensitive to noise, the 38 unbending profiles for the 38 movie frames are established by assuming that each 2D crystal unit cell can only drift along a linear trajectory of constant speed during the entire movie. This constraint allows unbending each of the 38 frames individually, resulting in the final dataset termed "MovieA". (C) An alternative movie-mode processing algorithm termed MovieB is also applied to the remaining 38 movie frames. This approach consists of grouping the frames into so-called super-frames, e.g., by combining groups of 7 original frames into one super-frame, resulting in 5 super-frames. These then provide sufficient signal-to-noise ratio to allow the determination of individual unbending profiles for each super-frame. The 5 super-frames are then unbend, and the data combined, resulting in the final dataset termed "MovieB". Both, MovieA and MovieB "learn" from the unbending profile in the Unbend2 run. Also, both movie-algorithms apply electron-dose dependent B-factor filtering of high-resolution terms in each frame, which is later corrected for during combination into a merged dataset for this movie.

and sharpening of the computed diffraction spots. To avoid malicious noise accumulation or the domination of reference bias, the raw image is never unbent multiple times, but instead a so-called distortion-vector field or "ERROR field" is continuously improved. The ERROR field obtained in the previous round of unbending is used as the starting solution for the current round of refinement. Generally, after three rounds of refinement, the final ERROR field is applied to unbend the raw micrograph in one step. The Fourier-transform of the unbent image is then evaluated to obtain the amplitude and phase values at the lattice reflection sites, and the data are CTF-corrected. If only global drift correction factors (x and y shifts) were applied to each frame before the averaged raw image was generated, this unbending procedure would give a lower-resolution result, since all local sample movements within the 2D crystals are ignored.

5.2.4.2 Algorithm: MovieA

A first movie-processing algorithm termed "MovieA" is then attempting to unbend each movie-frame individually (Figure 5.3b). This, however, generally fails for finely dose-fractionated image frames, because the remaining signal-to-noise ratio of individual frames no longer reliably allow the determination of the unbending profile. Here, we implemented an algorithm that starts from the unbending profile of the averaged image (Unbend2 profile), and searches for linear trajectories for each lattice node, along which these would have drifted with constant speed during the frames. The set of drift vectors is further compared with the drift vectors of neighboring crystal unit cells: if one drift-vector significantly deviates from that of its closest neighbors, this vector and its corresponding image patch are deleted from the dataset. Deletion of such an image patch is done by replacing it with a Gaussian blob with smooth edges onto all frames.

This linear-movement constraint allows determining interpolated unbending profiles for each of the movie frames, which are then executed, and the resulting unbent frames are averaged, Fourier-transformed, and evaluated for their amplitudes and phases. To account for electron-beam induced resolution loss, individual frames are B-factor resolution-wise filtered before processing, and the final, unbent and averaged map is corrected for that B-factor filtration before evaluation, as also done in RELION [Scheres, 2014] and Unblur [Grant and Grigorieff, 2015], and further detailed later.

5.2.4.3 Algorithm: MovieB

A second, alternative unbending algorithm, termed "MovieB" is also applied to the whole-frame drift-corrected movie (Figure 5.3c). In this algorithm, the electron-dose dependent B-factor filtered movie frames are grouped into fewer so-called super-frames, by, e.g., grouping each 7 raw frames into one super-frame. The resulting movie is composed of the much fewer super-frames, each of which now has an improved signal-to-noise ratio. These super-frames can then be individually unbent, using nevertheless the high-contrast "Ref." from Unbend2, and as starting template the unbending profile from the Unbend2 run. The resulting, individually unbent frames, are then

combined in Fourier space, corrected for the B-factor filtration, and evaluated, resulting in a set of amplitudes and phases termed MovieB.

5.2.4.4 Implementation details

In the above described algorithms for MovieA (correlated unbending profiles) or for MovieB (higher-contrasted super-frames), several parameters such as defocus, tilt geometry, crystal lattice, as well as the reference map for cross correlation with each movie frame, are taken from the first processing run termed Unbend2. The program $2dx\_quadserch$ was extended to be able to iteratively refine the determined ERROR field. When processing the first frame of a movie stack, we use the ERROR-field generated by the script "Unbend II" as the starting ERROR field for refinement. For all subsequent frames, the ERROR field generated while processing frame $(n-1)$ is used as the starting ERROR field for the peak localization when unbending frame (n). This approach exploits the smooth correlation between the crystal distortions among subsequent movie-frames to ensure a continuous and physically comprehensible motion-correction. Finally the MRC program $CCUnbend$ is used to correct each movie frame according to its corresponding ERROR field by shifting small image patches. The unbent images are then averaged, yielding one combined output image. Using the same global reference image for all frames ensures that the unbent frames are in register, which is a prerequisite for the final real-space averaging step. The MRC program $MMBoxA$ is finally employed to evaluate the averaged unbent frames, and to produce one APH-file from the averaged frames. Among other things, this APH-file contains amplitude, phase and SNR information for all computed diffraction spots. After correcting for CTF-effects, a 2D projection map is generated and finally the resulting APH-file can be used for 3D merging.

5.2.5 Accounting for resolution dependent radiation damage

As demonstrated in detail for catalase crystals by Baker et al. [Baker et al., 2010], electron beam damage is a crucial limit to high-resolution in cryo-EM. Based on the electron dose-dependent fading of diffraction spots, they showed how the optimal electron dose depends on the targeted resolution. For instance, to record data with an optimal SNR, a target resolution of 3 Å requires a cumulative electron dose of 11 electrons per Å^2, while a target resolution of 27 Å requires a total dose of 22 electrons per Å^2. Generally, a higher cumulative electron dose destroys the high-resolution details, but amplifies low-resolution features, such as overall shape and position of the particles.

DED movie-mode data acquisition allows dose fractionation, i.e., the distribution of a high electron dose over a large number of movie-frames. In this work, we recorded data with a cumulative dose of 40 electrons/Å^2 distributed over 40 movie-frames. Averaging a certain number of movie-frames during image processing allows average images corresponding to various desired electron doses to be generated. In practice, this has made it possible to assess the impact of

electron beam damage on different amino acids [Allegretti et al., 2014]. Nevertheless, such a-posteriori averaging of movie-frames still suffers from the trade-off between the optimal electron dose required to obtain the low and high-resolution information present in the images. Investigations of the dose-dependent fading of computed diffraction spots of thin 3D catalase crystals with 2dx were done in various studies [Baker et al., 2010; Bammes et al., 2010]. We conducted the same measurements of dose-effects for lipid membrane 2D crystals (Appendix B Figure B.1) to verify that the previous findings for thin 3D crystals are applicable here. Based on the previous studies and our measurements, we determined optimal low-pass filters that vary with the accumulated electron dose. This assures that all structure frequencies contribute to the resulting projection map at their optimal, dose-dependent SNR.

The determined B-factors establish that for the first few frames, all spatial frequencies contribute fully to the average, whereas for the later frames, where some high-resolution components of the structure have suffered from radiation damage, only the lower frequencies contribute to the average. The cut-off frequency $r(N)$ of the low-pass filters, expressed in absolute frequency units within the interval $[0, 0.5]$, was chosen such that $r(N) = Aexp(BN)$, where N is the frame number. The coefficients A and B are chosen according to the decay reported by Baker et al. [Baker et al., 2010]. Based on the assumption that for our dataset each movie-frame corresponded to an electron dose of approximately 1 electron/Å^2, we set $A = 0.8$ and $B = -0.05$. Although the parameters by Baker et al. [Baker et al., 2010] were determined for a different kind of crystal, our experiments ((Appendix B Figure B.1)) confirm that they are a good approximation for the application presented here. This procedure improves the stability and reliability of frame-wise crystal unbending by ensuring that all information present in the image frames is optimally available for processing. This approach was also done in single particle projects [Scheres, 2014], and also allows extension to significantly higher electron doses, as also performed elsewhere in the context of single particles [Grant and Grigorieff, 2015].

Sequential low-pass filtering of movie-frames prior to frame-wise unbending is an efficient way to computationally optimize the electron dose for each resolution range. Application of an appropriate weighting scheme while finally averaging the damage compensated frames is required to ensure correct sampling in Fourier space and to not disturb the subsequent 3D merging. This allows EM movies to be recorded with a higher cumulative dose than usual to ensure that no low-resolution information is missed.

5.2.6 Prevention of overfitting

5.2.6.1 When grouping frames into super-frames

The tendency to mistake noise for interpretable structural elements can be major problem of iterative algorithms used in cryo-EM. This so-called overfitting arises from the combination of the low SNR generally present in cryo-EM images and over optimistic resolution estimations for the reference used as template in different stages of the data processing. When we applied the

above algorithm to all movie-frames of an image-stack consecutively (electron dose of ~1 electron per Å^2 per frame or lower) we observed a serious overfitting issue indicated by discontinuous distortion-vector-fields and artificial ripples in the resulting projection maps (Figure 5.4). Due to the low signal present in each frame, the cross correlation profile lacked distinct correlation peaks, which significantly reduced the reliability of the MRC program $Quadserch$ to track the correct crystal unit cell locations. Increasing the ambiguity of cross correlation peaks can only be achieved by increasing the SNR of the raw data or the reference image. Using a larger reference would give a higher SNR for the cross-correlation map. However, cross-correlation with a reference that is too large reduces the possibility to track fine crystal distortions, i.e., any distortions that are smaller than the reference dimensions. On the other hand, increasing the SNR of the frames by using a higher electron dose per frame leads to beam-induced blurring within the frames caused by sample instabilities in the EM. Thus, a compromise has to be made. Here, in the algorithm termed "MovieB", we chose to average a given number of consecutive movie frames and process the resulting sub-frame averages like a movie. Such frame averages overcome the SNR-induced limitations described above. However, averaging multiple sub-frames and thus reducing the "electron dose fractionation" limits the possibility to capture all beam-induced motion. Nevertheless, the situation can be improved by applying a global frame-drift correction to each low SNR frame prior to the averaging step, in order to compensate for global stage drift and homogeneous beam-induced sample movement.

This poses the question of how many frames or what electron dose per Å^2 should optimally be averaged and processed together. We tested the movie-mode unbending algorithm with all conceivable numbers of averaged sub-frames and using the calculated parameter $QVal$ [Gipson et al., 2007a] to assess the obtained quality (Figure 5.4A); a higher $QVal$ value indicates that the image has more and/or sharper diffraction spots. In addition, we inspected the distortion ERROR fields and the projection maps obtained to see if overfitting could be visually detected (Figure 5.4C-E). Each of the movies analyzed consisted of 40 frames with a cumulative electron dose of 40 electrons/Å^2. As cryo-EM samples have the tendency to move most at the beginning of the exposure, we completely omitted the first two frames. Furthermore, the last six frames were only included in the initial high-SNR average calculated after global drift correction of the individual frames. To avoid the effects of beam-induced sample damage, these six frames were not otherwise used. Hence, we fully processed 32 frames of the movies with a cumulative electron dose of ~34 electrons/Å^2, including the two omitted frames at the beginning of each movie. This procedure complies with the settings previously used for movie-frame processing of single particle cryo-EM samples [Allegretti et al., 2014; Bai et al., 2013]. Note that ensuring equal divisibility of the data for the analysis meant that the total number of frames included varied slightly. On analyzing the effect of averaging different numbers of frames before movie-mode unbending, we observed three different regimes where the performance and reliability of the latter procedure differed significantly (Figure 5.4A). There were signs of overfitting when only a small number (1

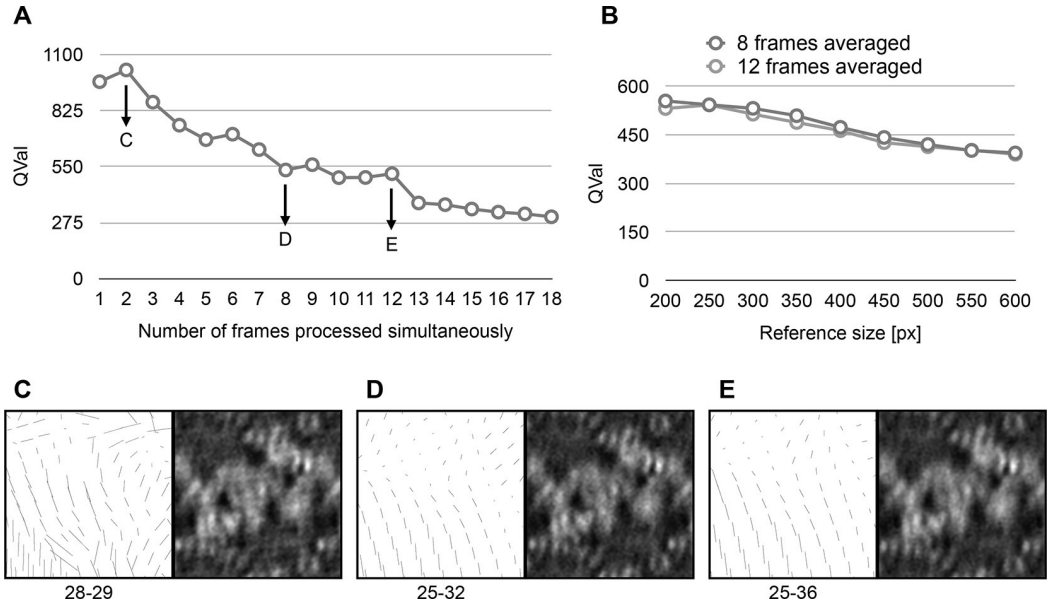

FIGURE 5.4. **Development of movie-frame unbending for the MovieB algorithm, using the MloK1 test dataset:** For this test dataset, classical processing resulted in a $QVal$ of 232.2. (A) Relationship between the number of averaged movie-frames and the measured $QVal$. During drift-correction at frame level, the two first frames were removed and thus omitted from the movie-mode unbending. Three different regimes were found: overfitting regime when 1-7 frames were averaged, indicated by artificially high $QVals$; working range of the processing procedure when 8-12 frames were averaged; and stiffness region when 13-18 subframes were averaged, where the detection of beam-induced motion-correction is limited due to large number of averaged frames. (B) Impact of the reference size on the measured $QVal$ analyzed for two different averaging schemes. (C-E) Visual comparison of the distortion-vector ERROR field (left) and the resulting projection map (right) when processing averages consisting of 2 frames (C), 8 frames (D), or 12 frames (E) were processed. The chaotic ERROR field in (C) is accompanied by striation artifacts in the image. (D) shows an optimal approach. (E) shows increased blurring in the image, due to a too smooth ERROR field.

to 7) of frames were averaged and processed, and the procedure was no longer able to resolve the beam-induced motion accurately enough if too many (13 to 18) frames were averaged. Averaging 8 to 12 frames gave optimal results. Movie-mode unbending of the resulting movies comprised of 3 or 4 averaged frames did not produce any signs of overfitting and still allowed beam-induced crystal alterations to be reduced. Although our observations were consistent over the whole MloK1 test dataset, the optimal batch size presumably depends on the sample as well as on the imaging conditions (structural contrast in the biological structure, acceleration voltage and applied defocus of the TEM, pixel size and type of utilized detector). It must be stressed that although the final movie used for movie-mode unbending was only comprised of 4 high SNR

frame averages, the 40 individual frames originally recorded were essential to allow global drift-corrections to be made over a fine dose raster. This important correction would not be possible if just 4 higher dose, and thus higher SNR frames were initially recorded per movie.

A similar experiment to the above was performed to determine the optimal reference size. As expected, Figure 5.4B confirms that the use of a larger reference leads to a lower $QVal$. From analyzing the $QVal$ measurements for different reference sizes and visually inspecting the distortion-vector ERROR fields, we conclude that for our dataset a reference size of 300 × 300 pixels (~ 3× ~ 3 unit-cells) prevented overfitting and allowed beam-induced sample deformations to be accurately corrected.

5.2.6.2 When constraining unbending profiles for frames

As an alternative to grouping frames into super-frames, we also developed an algorithm to determine unbending profiles for each single original movie frame. This was challenging due to the low SNR of individual frames, which made the reliable determination of lattice distortions impossible. We therefore developed an approach, termed "MovieA", where the unbending profiles are constrained by assuming a linear trajectory for each crystal lattice node. This is done by computing the cross-correlation maps of each single frame with the global reference pattern called "Ref." in Figure 5.3A. These, e.g., 38 cross-correlation maps are then inspected at each position of the unbending profile node position that was determined by the Unbend2 processing. For the close vicinity of each such node position, all possible combinations of linear movements through the cross-correlation maps are tested, until the one with maximized total contrast in all cross-correlation maps is found. This results in a linear movement vector for each crystal unit cell. These vectors are then compared with those of adjacent crystal unit cells, to identify outliers. Those outliers are then removed from the vector list, and the corresponding image segments in all frames are replaced by Gaussian-edged smooth patches.

Both algorithms, MovieA and MovieB, have advantages for certain image types. If frame-internal sample movements are linear, then MovieA is ideal. If instead, such movements are altering direction during dose-fractionated movie recording, then MovieB is the better compromise. A combination of both approaches (linear interpolation at the single frame level of movements determined on super-frames) is possible, but was not yet implemented.

The final algorithms for MovieA and MovieB, including frame averaging, optimal low-pass filtration, and sub-frame-average movie-mode crystal unbending, are illustrated in Figure 5.3.

5.3 Results and discussions

Cryo-EM images of 2D crystals of the cAMP-modulated potassium channel MloK1 (130 × 130 Å unit cell, $P42_12$ symmetry, vitrified on ultrathin carbon film supported by holey carbon film) were used to test the presented algorithms. This four-fold symmetric ion channel undergoes conforma-

tional changes upon cyclic adenosine monophosphate (cAMP) binding [Kowal et al., 2014]. Here, we used the cryo-EM data recorded in the presence of cAMP (open channel conformation, PDB Model: 4CHV).

5.3.1 Data acquisition and classical image processing

We recorded over 500 dose-fractionated movie-sequences, using a FEI Titan Krios equipped with a Gatan K2 summit detector (without energy filtration), operated in super-resolution electron counting mode, yielding movies with 8k × 8k frames. Images of crystals with a nominal sample tilt of up to 50° were recorded. The microscope was operated in low-dose mode at a nominal magnification of 22,500× at screen level, resulting in an effective magnification of ~37,000× on the detector. The resulting physical pixel size was 1.30 Å on sample level, respectively 0.65 Å for the super-resolution pixels. Movies consisting of 40 frames were recorded over 16 seconds total exposure, resulting in a 0.4 second exposure for each frame. The total electron dose per movie was ~40 electrons/Å^2, respectively ~1 electron/Å^2 per frame. Micrograph defocus varied between -0.75 and -4.3 μm. To avoid undercounting [Li et al., 2013], the electron dose rate was set to 5 electrons per physical pixel per second (respectively 1.25 electrons per super-resolution pixel per second). The images were corrected for frame-drift on-the-fly and automatically processed by 2dx_automator as detailed in [Scherer et al., 2014b]. The best 346 movies were used for 3D merging, including tilt-geometry refinement by means of the MRC program *Origtilt*.

5.3.2 CTF correction

CTF was corrected in stripes before unbending using phase flipping. The TTF correction and other approaches involving CTF correction before and after unbending using Wiener filter, CTF multiplication were tried, but the best results were obtained using phase flipping in stripes before unbending, as it corrects the phases and at the same time produces least amount of artifacts in the amplitudes.

5.3.3 Improvements

The best 346 movies were processed as described above, using Unbend2, MovieA and MovieB routines followed by 5×5 tiling of the images and recalculation of tilt geometry and defocus values at each tile. A new “final map” was produced from each of these tiles. All of these tiles with significant signal (a total of 6361 tiles) were considered for the final 3D reconstruction. Figure 5.5 shows the quality improvement due to movie-mode unbending for different crystals featuring different tilt angles. The impact of super-frame motion correction on a resulting crystallographic unit cell is shown in Figure 5.6. The correspondingly improved quality of the 3D density map in terms of visible details and resolved densities is shown in Figure 5.7. This structure is detailed in Chapter 7.

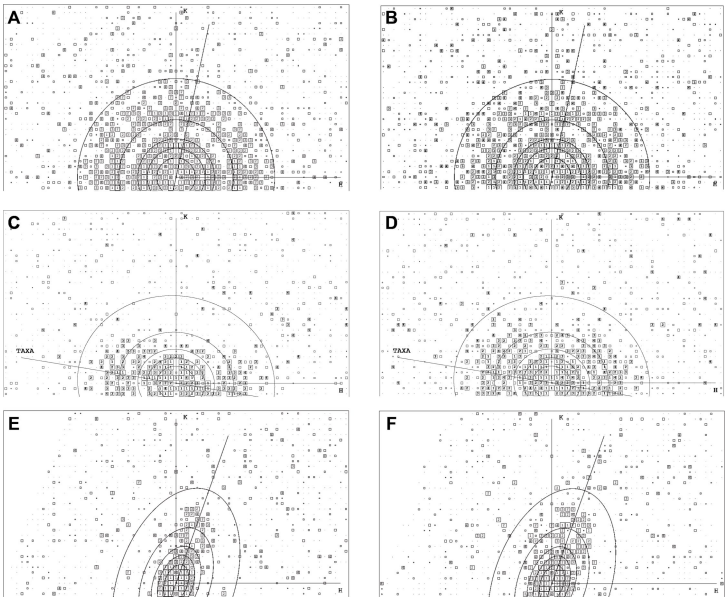

FIGURE 5.5. **Canonical IQ-plots obtained without and with movie-mode unbending applied to crystals with different tilt angles:** The Nyquist frequency of these plots is at 4 Å; the resolution circles are at 36 Å, 24 Å, 18 Å, 12 Å and 7 Å. (A) IQ-plot of a non-tilted 2D crystal without movie-mode unbending, i.e., unbending with Unbend2 of the drift-corrected sum of all movie frames. (B) IQ-plot of the same exposure as in (A) but after movie-mode unbending. (C) IQ-plot of a 20° tilted crystal without movie-mode unbending and (D) IQ-plot after movie-mode unbending. IQ-plot of a 50° tilted crystal (E) without movie-mode processing and (F) after unbending with. For movie-mode IQ plots, the best of MovieA and MovieB was considered. It can be seen that the IQ-plots after movie-mode processing show significantly more spots and also spots at higher resolution, especially orthogonally to the tilt axis (labeled with $TAXA$).

5.3.4 Algorithmic alternatives

Averaging batches of sequential movie frames to reduce the risk of overfitting is the key point of the presented algorithm. The drawback is that processing these averages produced distortion-vector ERROR fields that are a compromise for the averaged frame. The distortion-vector ERROR plots calculated for different averaged frames differed significantly from one averaged frame to the next. Due to the discrete frames that contributed to each averaged frame, these differences did not reflect smooth underlying physical movements. An alternative would be to compute so-called "rolling averages" of the frames, where each frame would contribute to multiple average frames. The average built for frame (n) would then also include down-weighted contributions from frames $(n-2)$, $(n-1)$ and frames $(n+1)$, $(n+2)$, etc., which could be used with a Gaussian weighting scheme centered on frame (n). The determined ERROR field of each average could then be applied to the single central frame of the rolling average only. Preliminary experiments with this method

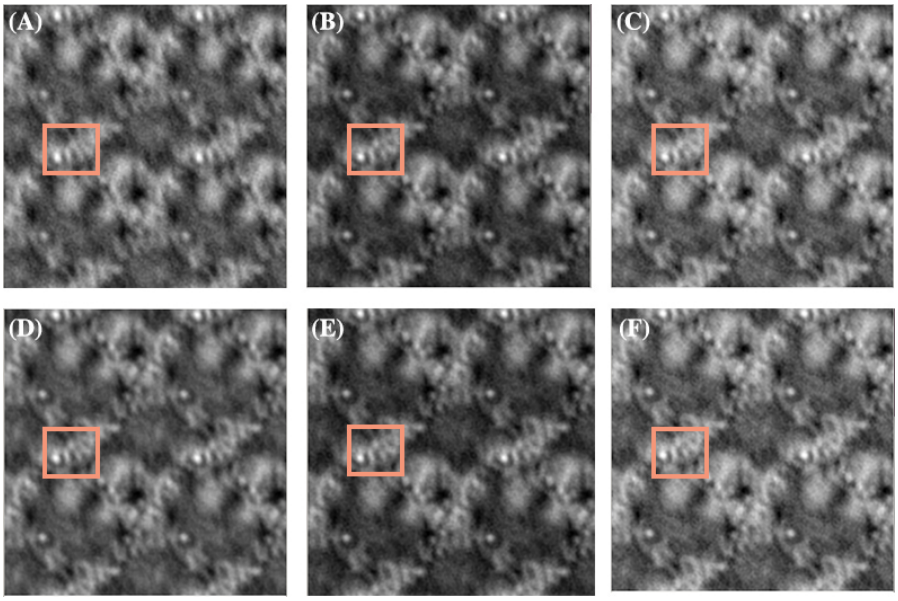

FIGURE 5.6. **Movie-mode unbending applied to a untilted crystal compared to classical processing using different drift correction software MotionCorr [Li et al., 2013] and MotionCor2 [Zheng et al., 2016]:** (A) Projection map obtained by drift correction with MotionCorr and classical processing using Unbend2. (B) Projection map produced by drift correction with MotionCorr and movie-mode unbending using the MovieA algorithm. (C) Projection map produced by drift correction with MotionCorr and movie-mode unbending using the MovieB algorithm. (D) Projection map obtained by drift correction with MotionCor2 and classical processing using Unbend2. (E) Projection map produced by drift correction with MotionCor2 and movie-mode unbending using the MovieA algorithm. (F) Projection map produced by drift correction with MotionCor2 and movie-mode unbending using the MovieB algorithm. The tilt axis is roughly horizontal. Inferred from the densities visible, the movie-mode processing resulted in higher resolution than the classical unbending. For instance, two helices in the marked square are separated in (B) and (C), but not in (A). MotionCor2 produces better results than MotionCorr and the movie-mode unbending still improves the overall sharpness of the image.

applied to the presented test dataset did not yield better results than the algorithm described before, possibly because rolling average images might not have been sufficiently dominated by the central frame to produce a valid ERROR field for that frame. At the extremely low SNR of the individual frames recorded here, computing ERROR fields that are valid for just one frame failed.

5.4 Conclusion

The described algorithms represent procedures tailored to achieve high resolution for 2D crystal images. Tiled image processing enables to improve the tilt geometries over the image. Movie-

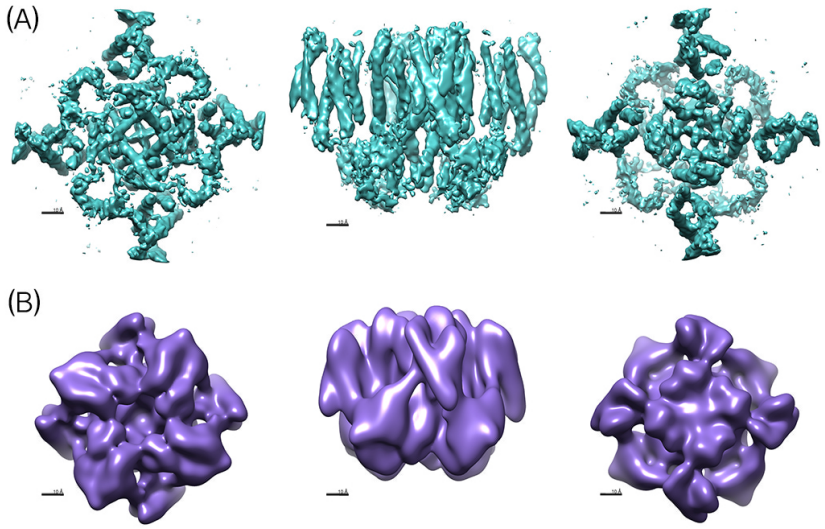

FIGURE 5.7. **Comparison of MloK1 3D-density maps:** (A) Top and side views of the 3D map generated using 2D crystal images obtained from FEI Titan Krios equipped with a Gatan K2 summit direct electron detector (without energy filtration) and subsequent application of the algorithms stated in this work, and (B) Top and side views of the 3D map from previous works [Kowal et al., 2014] obtained using films.

mode unbending offer an efficient and generic approach to correct for beam-induced translational motion within the dose-fractionated image frames, which previously limited the quality of 3D reconstruction obtained. We prevented overfitting by either constricting unit cell movements to linear trajectories only, or by averaging multiple drift-corrected movie frames into super-frames. We also employed dose-dependent resolution filters in forms of B-factors to ensure reliable processing. We carefully investigate the properties of the two key parameters of the new algorithm namely the "number of frames to average" and "reference size". Application of the new software to a real-world dataset significantly improved the results. The resolution attained in this project might be limited by (i) limited sample flatness, (ii) inhomogeneous conformations of individual proteins within the crystals [Rangl et al., 2016], and (iii) presence of a large missing cone due to limited sample tilt (Appendix B Figure B.3).

Furthermore we applied the unbending method to a different type of 2D crystals featuring a higher degree of internal order and flatness. Remarkably the movie-mode unbent computed diffraction patterns were of the same quality than the ones produced by electron diffraction (Appendix B Figure B.2). We previously presented a single particle approach for the analysis of 2D crystals to overcome resolution loss due to limited sample flatness [Scherer et al., 2014a]. Implementation of a movie-mode single particle method is now needed to enable full 3D tracking of the 2D crystals and correction for the physical movements of the membrane proteins forming

them.

CHAPTER 6

RETRIEVAL OF MISSING AMPLITUDES AND PHASES IN 2D ELECTRON CRYSTALLOGRAPHY

The following chapter is a part of the submitted manuscript:

Image processing techniques for high-resolution structure determination from badly ordered 2D crystals
*Nikhil Biyani**, Sebastian Scherer*, Ricardo Righetto, Julia Kowal, Mohamed Chami and Henning Stahlberg.
* *equal contribution*

in

Journal of Structural Biology.

Contribution:
Conceptualization, development and programming of the algorithm.

Abstract

The density maps generated by 2D electron crystallography are not perfect. They are modulated by the contrast transfer function of the microscope and suffer from the low signal-to-noise ratio of the images and radiation damage of the sample. Although these issues can now be tackled, mainly due to the development of direct electron detector devices, a few other challenges remain unsolved. The sample tilt angle achievable while collecting data, is typically limited to 60 degrees. This leads to a missing conical region in 3D Fourier space known as the “missing cone”. In real space, the missing cone makes the densities look elongated in the vertical direction. In addition, data can also be missing in other regions, depending on the tilt sampling. Here we report an iterative method that applies known constraints in the real and reciprocal space. A constrained real volume produces a new reciprocal volume, which in turn when constrained yields a new real volume. The constraints are iteratively applied in orthogonal real and reciprocal space until a convergence. A simple 3D reconstruction from weighted back-projection is used as the starting point of the iterations. The results show that reliable data is filled into the missing cone and that the overall resolution of the map is improved.

Keywords:
Electron crystallography; missing cone; data retrieval; shrinkwrap algorithm

6.1 Introduction

Two-dimensional (2D) electron crystallography of fully-ordered protein layers can determine the structure of the biomolecules present to a resolution of 1.9 Å [Gonen et al., 2005]. The thin 2D crystals imaged are generally comprised of membrane proteins embedded in lipids. They are maintained at cryo-temperatures in the transmission electron microscope (TEM) and examined, in the horizontal position and then when tilted at a range of angles along various tilt axes. In each case, either a diffraction pattern (diffraction mode) or a 2D projection of the electron density profile (imaging mode) is recorded. The goal is to obtain a density profile of the three-dimensional (3D) object [Schenk et al., 2005; Stahlberg et al., 2015], which can then be used to model atoms and obtain an approximate biomolecular composition [Adams et al., 2010; Alford et al., 2015; Jones et al., 1991; McRee, 1999]. Diffraction patterns only provide the amplitudes of the Fourier transform of the object; the phases need to be reconstructed by alternative methods [Fienup, 1982]. Images are 2D density profiles, and have to be corrected for the contrast transfer function of the microscope [Fernando and Fuller, 2007; Mallick et al., 2005; Mindell and Grigorieff, 2003]. The imaging mode allows crystal defects to be corrected by so-called 'unbending' procedures [Stahlberg et al., 2015]. Afterwards, the unbent data is merged in Fourier space using the Central Projection Theorem, and the target 3D density profile (3D map) is reconstructed by inverse Fourier transform.

The extent to which a sample can be tilted in the electron beam is limited to about 60 degrees. This is because the thickness of the irradiated layer increases with the tilt angle, decreasing the transmitted electron beam so that there is hardly any signal at higher tilt angles. Other factors such as sample movements and varying defocus also complicate the situation. As a consequence, slices with tilt angles beyond this limit, are missing from the reconstructed 3D Fourier space. Together, these missing slices correspond to a conical volume known as the "missing cone". The problem is illustrated in Figure 6.1. In real space, the missing cone means that reconstructed densities are elongated in the vertical (Z) direction. Data can also be missing in other Fourier space regions, depending on the tilt sampling. An infinite number of sample tilts would be required to completely fill the 3D space.

Filling the data in the missing cone is a signal recovery problem, where the missing spots in Fourier space are to be recovered using a priori information about the object under consideration. Phase retrieval, another signal recovery problem, has attracted a lot of interest [Fienup, 1982; Saldin et al., 2001; Wedberg and Stamnes, 1999; Yan et al., 2011]. In this case, the phase of a complex-valued function with known modulus has to be estimated. Many phase retrieval methods rely on Fienup's approach [Fienup, 1978], where known constraints are applied iteratively in the object space and its Fourier space. Bauschke et. al. [Bauschke et al., 2002] showed that the approaches used by Fienup, namely the error reduction algorithm, the basic input-output algorithm and the hybrid input-output algorithm, can be mathematically modeled as convex optimization problems. This approach was used by Barth et. al. [Barth et al., 1989] to retrieve

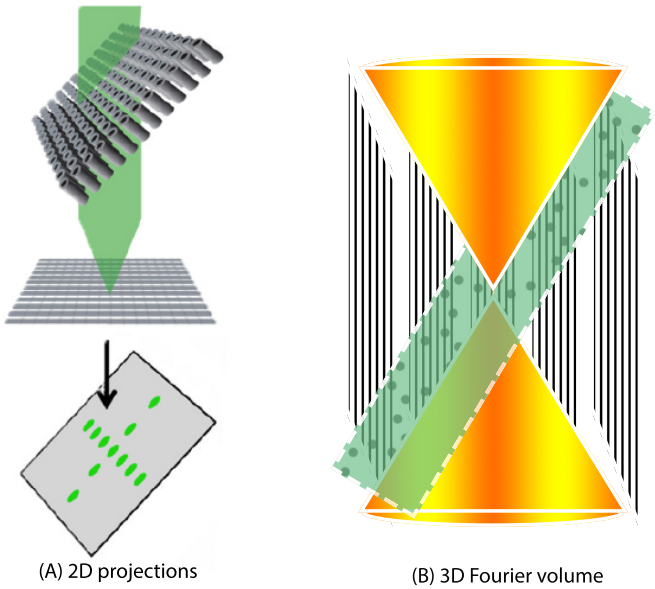

FIGURE 6.1. **Depiction of the "missing cone":** In 2D electron crystallography, images of 2D crystals are recorded in non-tilted and tilted positions. The Fourier transforms of these projections are merged to form a 3D Fourier volume. As the tilt angle of the crystals is limited, there are slices missing in Fourier space. Together, these missing slices form a conically shaped region in the 3D Fourier transform called the "missing cone". (A) Fourier transform of a projection recorded from a crystal tilted by 45 degrees. (B) The missing data shown as a yellow cone in 3D Fourier transform; the green plane corresponds to A.

phases in electron microscopy (EM). In 2D electron crystallography imaging, the problem is slightly different to phase retrieval, since the amplitudes and phases are known for part of the signal and the rest need to be estimated.

The work by Gipson et. al., [Gipson et al., 2011] presents an iterative approach called the projective constraints optimization (PCO) that addresses this challenge to fill in missing amplitudes and phases. The method relies on iteratively applying known constraints in real and Fouirer space. It also provides a transform to convert the uniformly spaced lattice lines in real space to the non-uniform reciprocal space lattice lines, replacing the traditional lattice line fitting [Agard, 1983]. Uncoupled amplitudes and phases are used as the raw data, and truncated singular value decomposition is applied to transform between the object space and irregularly sampled Fourier space with fractional steps and individual point-wise weighting.

In this work we establish the convex optimization problem to fill in missing amplitudes and phases in the 3D Fourier space generated by 2D electron crystallography images of a regular grid, i.e., a 2D protein crystal. Unlike PCO or traditional lattice like fitting, we employ weighted back-projection to obtain the first reconstruction using density images, and then use this data in an iterative approach to retrieve missing amplitudes and phases. In addition, we

introduce the possible constraints in real and reciprocal spaces including a modified version of the shrinkwrap algorithm introduced by Marchesisni et. al. [Marchesini et al., 2003] for X-ray image reconstruction.

We test our method on a simulated dataset generated for a protein structure, where we remove a cone of data from the Fourier transformed object and try to recover the lost information using our algorithm. Discrete Fourier transforms are employed to transform between the spaces in each iteration. We also apply the algorithm to an experimental 2D electron crystallography dataset. In principle, our approach can be independently used to retrieve missing amplitudes and phases in other electron microscopy techniques, such as single-particle reconstruction and electron tomography. A C++ software that incorporates this algorithm is available and can be downloaded free of cost.

6.2 Theory

6.2.1 Problem statement

A Fourier transform of a real finite 3D object provides a function of infinite extent, but the data that can be recorded by microscopes is always limited; analysis of the recorded data would lead to a non-perfect reconstruction of the object. The goal is, then, to retrieve the missing signal using a priori information about the object.

Let the object s live in functional space S mapped from 3D euclidean space $\mathbb{R}^3$ to a complex space $\mathbb{Z}$, i.e., $S : \mathbb{R}^3 \rightarrow \mathbb{Z}$, or in other terms, for any, $t \in \mathbb{R}^3$, there exists a function, $f(t) \in \mathbb{Z}$. A set of n reflections $r_i \in \mathbb{Z}$ at spots $t_i \in \mathbb{R}^3$ with known amplitudes and phases is collected via experiments and is known. Let this set of known reflections be called as, $K \subseteq S$.

$$K = \{t_i \rightarrow r_i, \forall i = 1,2,\ldots,n\} \tag{6.1}$$

Using this set, the first constraint set F that satisfies the Fourier domain constraints can be formulated as follows:

$$F = \{s \in S : K \subseteq \mathbb{F}(s)\} \tag{6.2}$$

where $\mathbb{F}(s)$ denotes the Fourier transform of s. Note that the set providing the Fourier transform $\{\mathbb{F}(s)\}$ also lives in functional space S.

To pose the constraints in object space, we assume that the support of object s is contained in set $D \subset \mathbb{R}^3$. Let 1_D denote the characteristic function of D and let 1_D^- be its complement set. Now a set O that specifies the constraints in object space can be written as follows:

$$O = \{s \in S : s \cdot 1_D^- = 0\} \tag{6.3}$$

The problem is to find object s, or its Fourier transform $\mathbb{F}(s)$ in the intersection of the sets, such that:

$$s \in F \cap O \tag{6.4}$$

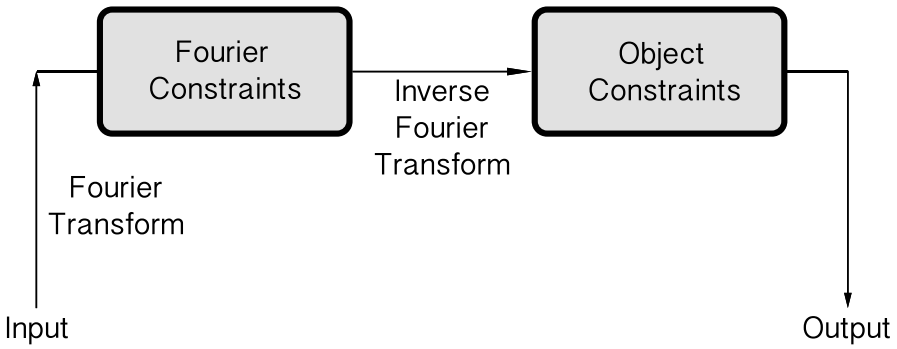

FIGURE 6.2. **A schema of iteration to develop the sequence of solutions:** Each iteration of the algorithm proceeds with application of the Fourier constraints to the Fourier transformed image followed by the inverse Fourier transformation and application of the object space constraints.

6.2.2 Algorithm

The approach is to develop a sequence of possible solutions by enforcing the known constraints. At a given point in the sequence, first the constraints in the Fourier domain are fulfilled and then the constraints in the object space. This results in a new term of the sequence. The schema of each iteration is shown in Figure 6.2.

The produced term of the sequence is an intersection of the required constraints from Fourier and object space. It should be noted that the terms of the sequence change less as the iterations progress. In other words, the error is reduced and the result converges to a stable solution. Hence, the sequence can be iteratively developed until a convergent solution is found. The proof of convergence of such algorithms can be found elsewhere [Combettes and Trussell, 1990; Gerchberg and Saxton, 1969].

Projection operators are used to apply the constraints to sets F and O introduced in the previous section. The projection operator that applies object constraints, $\wp_O$, can proximinally [Deutsch, 1980] be obtained by setting all elements in the current set that do not lie in the support D to zero. When applied, the projection operator for Fourier constraints, $\wp_F$, will just replace the reflections in Fourier space by the set of known reflections K. Thus, the expressions to progress the sequence given the current term s_n can be written as follows:

$$s_n^* = \mathbb{F}^{-1}(\wp_F(\mathbb{F}(s_n)) \tag{6.5}$$

$$s_{n+1} = \wp_O(s_n^*) \tag{6.6}$$

It should be noted that the schema provided here is based on Fienup's error reduction approach [Fienup, 1978]. Other variants with basic input output and hybrid input output can also be applied.

6.2.3 Extracting the known reflection set

It is essential to have a correct set of reflections to use in the iterative algorithm. As outlined above, in 2D electron crystallography, images of 2D crystals are recorded not only with the crystal sheet perpendicular to the beam, but also at various tilt angles. The image data collected from a series of non-tilted 2D crystals is merged to obtain an initial estimate of the horizontal (XY) plane of the Fourier transformed object. The image data from tilted crystals is merged onto this plane using the Central Projection Theorem, which in turn fills the values in the vertical (Z) axis of the Fourier transformed object. For a certain $t \in \mathbb{R}^3$, several possible reflections $r_i \in \mathbb{Z}, i = 1,2,\ldots,n$ can exist, originating from the same or different images. Recall that for any object $s \in S : \mathbb{R}^3 \rightarrow \mathbb{Z}$, has a bijective mapping. Thus, one needs to calculate a reflection $r \in \mathbb{Z}$ from all possible reflections, r_i. Here it should be noted that each of these r_i has a certain Figure of Merit (FOM), $w_i \in [0,1]$, which corresponds to the signal-to-noise ratio (SNR) of the reflection or, in other words, how accurately the reflection was recorded.

The weighted average of all the possible reflections described in the following equation can be used to calculate the final reflection.

$$r = \frac{\Sigma_{i=1}^{n} w_i r_i}{\Sigma_{i=1}^{n} w_i} \tag{6.7}$$

However, the amplitude of the final reflection should be corrected by multiplying it by the average FOM value of all possible reflections. This is done to decrease the intensities of spots that have a lower SNR. The FOM values are averaged in a special way [Blow and Crick, 1959; Sim, 1959, 1960]. For example, two spots with an FOM of 0.7 should finally result in an average with an FOM of more than 0.7, as the probability of attaining a certain value of r increases. To average the FOMs, we first convert them to $XARG$ values mapped by the modified Bessel functions of the first kind and given by the following equation:

$$w_i = \frac{J_1(a_i)}{J_0(a_i)} \tag{6.8}$$

where, J_k is the modified Bessel function of the first kind with order k, and a_i is the $XARG$ value. Once we have determined the $XARG$ values corresponding to the FOM values, we average them in the following way:

$$\bar{w} = \frac{J_1(\Sigma_{i=1}^{n} a_i)}{J_0(\Sigma_{i=1}^{n} a_i)} \tag{6.9}$$

In this article we refer this procedure as the *weighted back-projection*.

6.2.4 Getting the support in Object space

An approximation of all the data points (voxels) in object space that are expected to have non-zero values, defines the support of the object. This support set can be developed using the constraints on the density values that a particular object under consideration could achieve. Some of these constraints are demonstrated below.

6.2.4.1 Membrane slab

The target objects of electron crystallography are often 2D crystals of membrane proteins, i.e., sheet-like structures with a repeating unit. This protein sheet has a well-defined boundary in the vertical (Z) axis. One can exploit this fact and restrict the support to a certain length on the Z axis.

6.2.4.2 Real valued non-negative densities

The nature of the problem implies that the densities obtained at any instance should always be real-valued and non-negative. Consequently, all negative densities can be removed from the support.

6.2.4.3 Modified shrinkwrap optimization

The shrinkwrap optimization updates the support using the density at the current iteration [Marchesini et al., 2003]. An envelope is created by applying a low pass filter to the current volume. A low density threshold is applied to this filtered version to update the support. This assumes that the target objects are continuous and that all the real features can be contained within the blurred low pass filtered envelope. Whatever remains outside the envelope is considered to be noise. The threshold is data set dependent and should be chosen so that the noise is avoided without the loss of true features.

We introduce a modified version of this shrinkwrap optimization where instead of using a binary mask we use a weighted masking with two different density thresholds ϵ_l and ϵ_h, with $\epsilon_l < \epsilon_h$. Using the above procedure we create two sets D_l and D_h defining the support of the object, where D_l corresponds to the set with threshold ϵ_l and D_h corresponds to the set with threshold ϵ_h. When applied in this case, the projection operator $\wp_O$ would yield the following result:

$$\wp_O(s_n(t)) = \begin{cases} s_n(t); & \forall t \in D_l \cup D_h \& s_n(t) > \epsilon_h \\ 0; & \forall t \in D_l \cup D_h \& s_n(t) < \epsilon_l \\ \frac{s_n(t)-\epsilon_l}{\epsilon_h-\epsilon_l}; & \forall t \in D_l \cap D_h \end{cases} \tag{6.10}$$

This means that all the densities lying in the region above ϵ_h are kept intact, while the densities lying below ϵ_l are deleted and the rest are linearly scaled from ϵ_h to 0. Using the modified shrinkwrap optimization, one can chose thresholds and minimize the errors that occur with the assumptions of traditional binary masking.

6.3 Materials and methods

The method was tested on various simulated and experimental datasets. In each case some information was missing. We tried to recover this using the algorithm described above.

6.3.1 Simulated dataset

A representative membrane protein structure from the Protein Data Bank (PDB) 4CHW [Kowal et al., 2014] was used for the simulations. This atomic model was converted to an electron density volume using EMAN2 [Tang et al., 2007]. The resulting volume was considered to be the ground truth. To generate a test data set, specific amplitudes and phases were removed from the Fourier transform of the ground truth volume. The algorithm was then applied to the remaining volume. The constraints included known reflections in reciprocal space and non-negative density and shrinkwrap refinement in real space. For the shrinkwrap optimization we used 10Å as the higher resolution limit and applied a single threshold value at 6% of the maximum density of the present volume in each iteration round. The information recovered by the application of the algorithm was compared to the data initially removed from the ground truth.

6.3.2 Experimental dataset

We also tested our approach on an experimental cryo-EM dataset recorded from naturally occurring 2D crystals of bacteriorhodopsin (purple membranes). Purple membranes were isolated from Halobacterium salinarum (ET 1001) as described by Oesterhelt and Stoeckenius [Oesterhelt and Stoeckenius, 1974]. 1μl of purple membrane sample at 1 mg/ml was adsorbed to a carbon film, embedded in 3.5% trehalose using the symmetric carbon sandwich technique as described by Gyobu et al. [Gyobu et al., 2004], and plunge-frozen in liquid nitrogen.

The frozen grids were transferred to an FEI Polara microscope operated at an acceleration of 300kV. The sample was kept at -180°C. Movie-mode images with 40 frames were recorded at a total dose of 40 electrons per Å^2 using a Gatan K2 Summit direct electron detector. In each case, the recorded frames were drift corrected and averaged using MOTIONCORR [Li et al., 2013]. The non- tilted and tilted sample (0 to 45°) was imaged; 50 movie-mode images were collected in total. The averaged drift-corrected images were processed with the 2dx software package (http://2dx.org) [Gipson et al., 2007a,b; Zeng et al., 2007]. Within 2dx, images were corrected for crystal disorder without the use of any external software. Defocus and astigmatism were determined by CTFFIND3 [Mindell and Grigorieff, 2003]. The tilt geometry was initially

determined by the defocus gradient, initially refined based on the lattice parameters and later based on comparisons of the single images with the merged 3D volume. 3D merging was done with 2dx_merge using ORIGTILT [Crowther et al., 1996]. 2D crystallographic point group P3 symmetry was applied during merging. Only 33 of the recorded movie-mode images were used to obtain the final reconstruction. The tilt and resolution was deliberately restricted in order to assess the performance of the algorithm. A final set of reflections was collected by weighted back-projection.

The algorithm described above was applied to this merged dataset. The constraints used in object space included non-negative real densities, a membrane slab width of 62 Å and the modified shrinkwrap optimization described above. For the shrinkwrap optimization the volume was first low pass filtered at 10 Å with the higher and lower density thresholds set at 11% and 8% of the maximum density value respectively, in the present volume. The data was recovered only in a specific vertical conical region with apex angle of 140°, keeping the rest intact. To stop the recovered reflections from increasing unrealistically, they were decreased by a factor of 0.3 in each round of iteration.

We compared the results with the 1.78 Å atomic model of bacteriorhodopsin determined by X-ray crystallography (PDB entry 3NS0 [Borshchevskiy et al., 2011]) to assess the algorithm. Note that this X-ray model was only used to evaluate the quality of our data; it was not used during the processing at any time.

6.3.3 Quality evaluation

As one of the measures to evaluate the quality of the obtained data, we used the spectral Fourier Shell Correlation (FSC) curves to compare the two volumes. These curves depict how well things correlate in various frequency shells of the Fourier volume [Harauz and van Heel, 1986]. Correlation values are in the range [0,1]. Randomly generated features result in a correlation value of zero on average [Patwardhan et al., 2012]. Higher correlation values are obtained if the volumes compared have the same information in one or more frequency ranges. We also used the Cylindrical Ring Correlation (CRC) to describe the correlation in 2D [Gipson et al., 2011]. CRC calculates the Fourier ring correlation for each horizontal 2D slab of 3D Fourier space between two datasets. CRC produces a 2D plot with the resolution in the XY-direction on the horizontal axis and the resolution in the Z direction (height) on the vertical axis.

6.4 Results and discussions

6.4.1 Retrieval of a missing plane

In this experiment, we removed a single 2D plane from the Fourier transform of the ground truth object. The $Z = 0$ plane was selected as it has a special significance in electron crystallography; it is the result of merging the images of the non-tilted 2D crystal, and also serves as the first

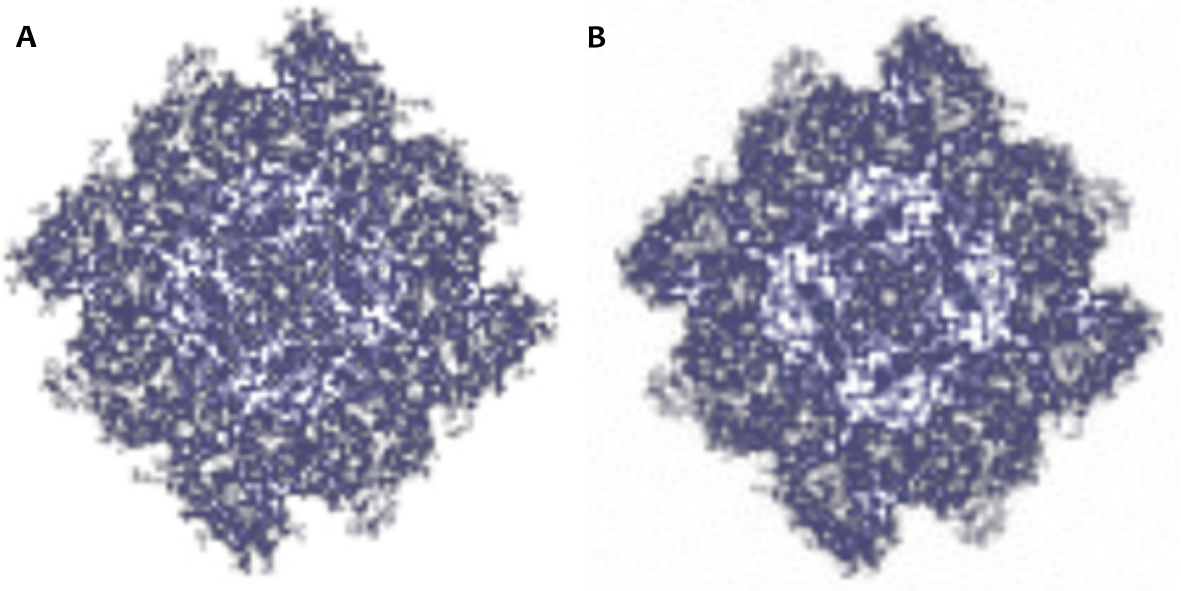

FIGURE 6.3. **Comparison of the ground truth and the recovered planes in real space:** (A) Ground truth $Z = 0$ plane that was removed. (B) $Z = 0$ plane recovered by application of the algorithm.

point in the 3D merging procedure. Once the $Z = 0$ plane had been removed, we applied the algorithm outlined above to try to reconstruct it. Figure 6.3 shows a real space comparison of the reconstruction and the ground truth. The shape and intrinsic properties of the ground truth plane are preserved in the recovered plane.

The FSC curve for the $Z = 0$ plane of the ground truth and the recovered Fourier space data is shown in Figure 6.4. There is good overall correlation, which indicates that the method works well when applied to recover one of the most important planes of the 3D Fourier space.

6.4.2 Retrieval of a missing cone

In the next experiments, we extended the region removed and cut out a cone instead of a plane from the Fourier space data. We used the remaining data as the known reflections set for the algorithm. Furthermore, we varied the cone angle (the angle between cone's generatrix and it's axis) from 30 degrees up to 80 degrees to fully test the capability of the algorithm. The FSC curves obtained when the ground-truth cone cut and the cone recovered by our algorithm were compared are shown in Figure 6.5. These show that while the low-resolution data can be recovered up to a resolution of 10 Å, even with an 80 degree cut, the recovery of high-resolution information depends on the amount of missing data.

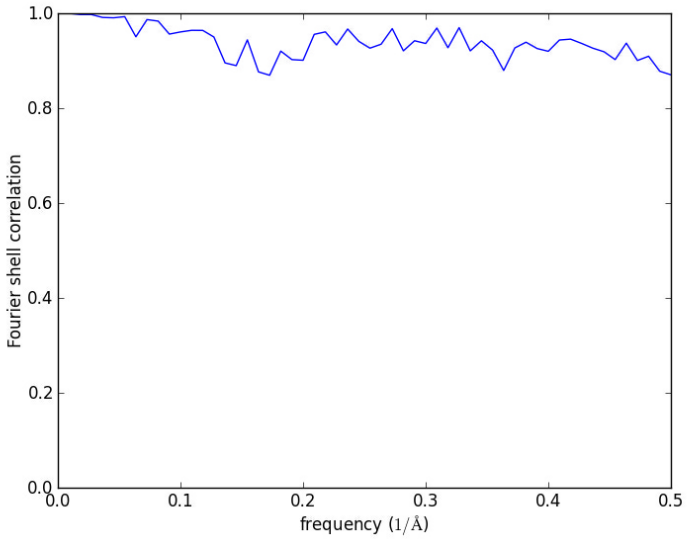

FIGURE 6.4. **FSC of the recovered plane with ground truth plane:** FSC plot between the original ground truth $Z = 0$ plane that was removed before refinement and the recovered $Z = 0$ plane shows that the recovered information has good correlation with the expected values.

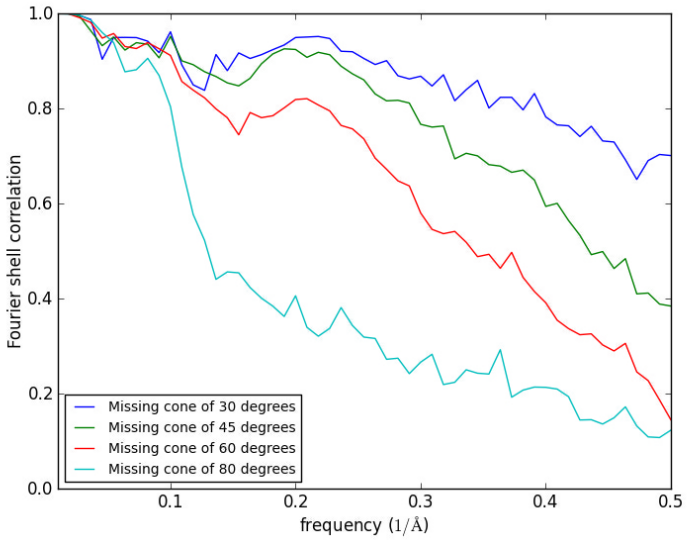

FIGURE 6.5. **FSC of the cut cones with ground truth cones:** Plot of FSC between cut ground truth cones and recovered cones of various angles. In general the low resolution data is preserved even for high cuts.

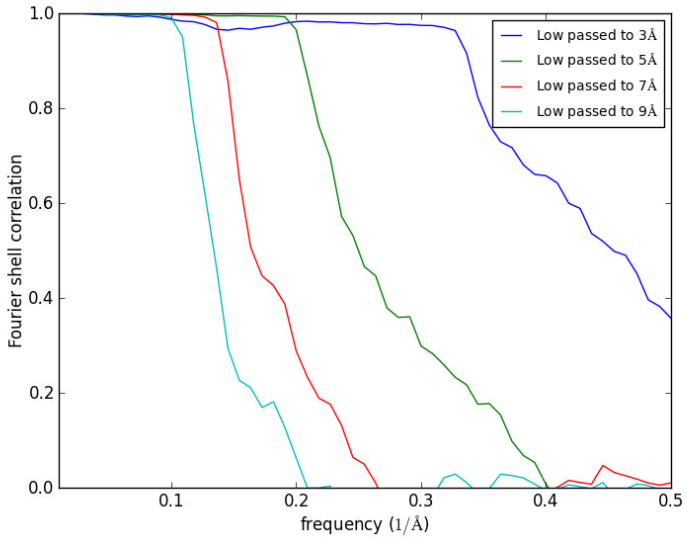

FIGURE 6.6. **Evaluation of the performance of our method at high-resolution data:** The ground truth Fourier space data was cutoff at various frequencies as indicated and the algorithm was applied. The plot shows the FSC curves obtained when the ground truth (unfiltered) and the recovered Fourier volumes were compared.

6.4.3 Performance at high resolution

To evaluate the performance of the algorithm at high resolutions, we low pass filtered the ground truth density volume to various frequencies, and applied the iterative algorithm to recover data lying beyond the cutoff frequency. Comparison of the reconstructed volumes with the original unfiltered volume shows that we can partially reproduce missing high resolution data. However, the frequency up to which we can recover data depends on the cutoff frequency. Figure 6.6 explains this relationship in detail. It shows the FSC curves obtained by comparing the recovered and unfiltered original ground truth Fourier space volumes. The correlation curves do not fall instantly at the cutoff frequency, indicating that the data recovered at higher resolution agrees with the original data to a certain extent, depending on the cutoff frequency; in general there is a good correlation for about 1 Å in addition to the cutoff frequency (in Å). This implies that using the algorithm described improves the resolution of the reconstructed volume, if the data is noise-free and the recorded data has no errors.

6.4.4 Experimental dataset

An experimental dataset was recorded from 2D crystals of bacteriorhodopsin using an FEI Polara equipped with a Gatan K2 Summit camera (see Material and Methods). Only 33 images in total were used to reconstruct the volume. This set included images of samples tilted by up to 45

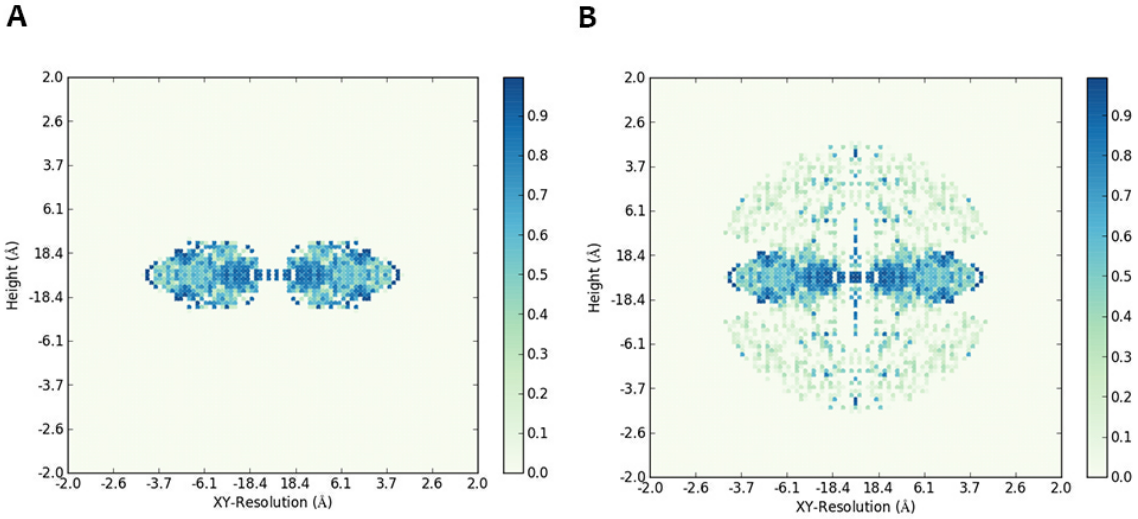

FIGURE 6.7. **Cylindrical ring correlation plots of bacteriorhodopsin:** (A) The bacteriorhodopsin volume reconstructed from the raw data and (B) refined bacteriorhodopsin volume obtained by application of the algorithm, compared to the density map of the atomic model 3NS0 filtered to a resolution of 3Å. The plots show the XY-resolution on the horizontal axis and the height of the reconstruction on the vertical axis. The correlation values are color-coded according to the bar shown to the right of each plot. The darker the spot, the higher the correlation. The data present in the raw volume was restricted both in terms of resolution and vertical height. The data recovered by application of the algorithm also has a good correlation with the atomic model.

degrees, i.e., less than the maximum possible. The data was intentionally limited to test the performance of the algorithm. Reflections were present in the missing cone after the algorithm had been applied. To check the correctness of the recovered data, we compared the result with the atomic model of bacteriorhodopsin 3NS0 by CRC. CRC provides a 2D plot describing the correlation between two volumes at the XY-resolution and height of a particular spot in Fourier space. As shown in Figure 6.7(A), the volume reconstructed from the raw data was limited in height as well as in resolution. After the application of the algorithm we notice from Figure 6.7(B) that there are many more peaks that appear in the CRC. This indicates that the reflections that appear as an output of the algorithm also correlate with the atomic model. The extent of correlation of the new reflections, though, is not as high as the original data. The high correlation on the vertical axis is an artifact that arises because the real space volume was not periodic. The correctness of the produced data depends on the quality and quantity of the input provided.

6.5 Conclusions

Electron density maps generated by 2D electron crystallography lack certain data in reciprocal space. Here, we present an easy to implement iterative algorithm to generate the missing data in Fourier space. The algorithm relies on constraints enforced in orthogonal object and reciprocal space. For example, a known set of reflections can be used as a constraint in reciprocal space, and the shrinkwrap algorithm and non-negative densities can be used as constraints in object space. Any volume that satisfies all of the constraints simultaneously is a possible solution of the system. The projection operators used to apply the constraints in object space simply set the value of the voxels not in the support to zero, and the projection operator used to apply the constraints in reciprocal space replaces the estimated by the known set of reflections. Retrieval of the missing data is observed when the algorithm is applied to both simulated and experimental dataset. In simulated experiments, missing cones were reliably generated depending on the extent of cut and some amount of higher resolution data was also produced. Application of the algorithm to a tilt-limited and resolution-limited experimental dataset, reduced the amount of missing data. The reliability of the densities generated, was demonstrated by comparison with a known structure. An open source C++ implementation of this algorithm is available on github.

CHAPTER 7

HIGH-RESOLUTION STRUCTURE OF THE MLOK1 K^+ CHANNEL

The following chapter has been submitted for publication as:

High-resolution cryo-EM structure of the cyclic nucleotide-modulated potassium channel MloK1 in a lipid bilayer.
Julia Kowal, *Nikhil Biyani*, Mohamed Chami, Sebastian Scherer, Andrzej Rzepiela, Paul Baumgartner, Vikrant Upadhyay, Crina M. Nimigean and Henning Stahlberg.

Contribution:
Image processing of the collected images and generation of the final three-dimensional density map.

Abstract

Eukaryotic cyclic nucleotide-modulated channels perform their diverse physiological roles by opening and closing their pores to ions in response to cyclic nucleotide-binding. The lack of high resolution structural information for members of this channel family has hampered a mechanistic understanding of their function. The best structural model currently available is for the cyclic nucleotide-modulated potassium channel homologue from *Mesorhizobium loti*, MloK1, which forms micrometer-large 2D crystals in the presence of lipids that only diffract to ~10 Å. Using cryo-electron microscopy (cryo-EM) and newly developed computational methods, we have determined a three-dimensional (3D) map of full-length MloK1 in the presence of cAMP at sub-5Å isotropic 3D resolution. The cryo-EM structure presented provides a clear picture of the arrangement of the cyclic nucleotide-binding domains with respect to both the pore and the putative voltage sensor domains when cAMP is bound, and reveals a potential gating mechanism in the context of the lipid-embedded channel.

Keywords:
MloK1, MlotiK1, potassium channel, CNBD, cryo-electron microscopy, cytoplasmic domains

7.1 Introduction

Hyperpolarization-activated cyclic nucleotide-modulated (HCN) and cyclic nucleotide-gated (CNG) channels are members of the voltage-gated potassium channel superfamily. In photoreceptor cells and olfactory receptor neurons, CNG channels mediate the passage of cations across the membrane to generate an electrical signal in response to light- or odorant-induced changes of intracellular levels of cyclic nucleotides. Mutations in these channels result in severe, untreatable degenerative retinal diseases or olfactory dysfunction[Michalakis et al., 2006; Nache et al., 2016], respectively. HCN channels are responsible for the pacemaking activity of heart and brain, and defects lead to cardiac and brain disorders[Craven and Zagotta, 2006].

Significant knowledge exists from years of electrophysiological studies, sequence homologies with voltage-gated potassium channels whose structures are available, and X-ray structures of isolated domains. Only very recently, high-resolution structures of two members of CNG and HCN channel families were solved with single particle cryoEM [Lee and MacKinnon, 2017; Li et al., 2017].Like all known members of the voltage-gated ion channel superfamily, HCN and CNG channels are tetramers. Each monomer has six transmembrane helices (S1 to S6), a pore region between S5 and S6, and an S1-S4 voltage sensor domain (VSD). A cyclic nucleotide binding domain (CNBD) is attached to the end of the last transmembrane domain, S6, via a C-linker. This hexahelical, ~80 amino acid (aa)-long region is believed to be involved in coupling cyclic nucleotide binding to channel opening. The VSD is connected to the pore region via an S4-S5 linker. The S4-S5 linker, proposed to couple voltage signaling through the VSD to ion channel opening in voltage-gated ion channels [Long et al., 2005b], is an α helix that lies parallel to the membrane [Long et al., 2005a, 2007; Payandeh et al., 2011] and facilitates the “swapped” configuration of the pore domains and VSDs. Interestingly, the recently published structures of human HCN1 [Lee and MacKinnon, 2017] and C. elegans TAX-4 CNG [Li et al., 2017] have a “non-swapped” arrangement of the pore domain and VSDs, in which each voltage sensor interacts only with the pore domain of the same subunit, similar to what has been observed in the structures of BK channels and EAG channels [Hite et al., 2015; Whicher and MacKinnon, 2016]. The previously published low-resolution structures of the prokaryotic potassium channel MloK1 [Chiu et al., 2007; Kowal et al., 2014], indicated that the voltage sensors interact with an adjacent subunit, similar to Kv and voltage-dependent Na+ and Ca2+ channels [Chiu et al., 2007]. This domain swapped VSD suggests that the MloK1 S4-S5 linker functions as a mechanical lever through which conformational changes in VSD lead to channel gating.

MloK1 shares most of its architectural features with its eukaryotic counterparts, with the exception of its pore-domain/VSD arrangement that is in a “swapped” conformation, and its C-linker that is considerably shorter than that of related channels (~20 amino acid residues). While the similarities highlight the powerful insights to be drawn about the eukaryotic channels from an MloK1 structure, the differences indicate a potentially interesting departure, from a functional point of view, between these channels in different species. MloK1 has been studied

by cryo-EM before; the available 7-12 Å-resolution structures in the presence and absence of cAMP were obtained by cryo-electron crystallography of 2D crystals formed in lipid bilayers [Kowal et al., 2014]. Despite the low resolution, these structures provide important information about the architecture, the domain disposition and the conformational changes that occur upon ligand binding. They show that, in a lipid environment, MloK1 shares most of the architectural features of voltage-gated potassium channels in the transmembrane regions, and that the CNBDs undergo a large-scale domain movement upon ligand binding. However, many important details necessary for finer mechanistic inferences are not discernible. For example, the loops connecting the transmembrane helices with one another and with the CNBDs are not resolved, casting uncertainty on whether the CNBDs interact directly with the voltage sensors or are simply close-by. Similarly, the low resolution does not allow precise measurement of the intracellular pore opening created by the S6 helices, and does not deliver a detailed picture of the selectivity filter. Due to lack of resolution, both the exact orientation of the CNBDs with respect to each other and to the S6 helices remain unclear.

Here, we present the first full-length MloK1 structure at a resolution of better than 5 Å. This was solved by cryo-electron crystallography from 2D crystals formed in lipid bilayers. The high resolution allows us to glean many more insights into the molecular architecture of such channels and their mechanism of function, and provides answers to some of the questions listed above. Due to their similarities, some of the observations about the gating mechanism can be extended to the eukaryotic family of cyclic nucleotide-modulated channels. On the other hand, the structural and functional differences between MloK1 and the eukaryotic channels provide a rich ground for forays into mechanistic insights.

7.2 Materials and methods

7.2.1 Protein purification and 2D crystallization

Cyclic nucleotide-modulated potassium channel MloK1 was purified and crystallized in 2D in the presence of cAMP ligand as described in [Chiu et al., 2007; Kowal et al., 2014; Nimigean et al., 2004; Rangl et al., 2016]. Briefly, *E. coli* BL21(DE3) cells were transfected with the 6-His-tagged MloK1 construct and protein expression was induced with 0.2 mg/ml anhydrotetracycline for 2 h. After sonication, cell membranes were solubilized with 1.2% n-decyl-β-D-maltopyranosite (DM, Anatrace) in the working buffer containing 295 mM NaCl, 5 mM KCl, 20 mM Tris-HCl pH 8.0, 10% glycerol, 1 mM PMSF, and 0.2 mM cAMP, and stirred for 2.5 h at 4°C. The extract was centrifuged at 37,000×g and the supernatant was applied to a Co^{2+} affinity column that had been washed with buffer containing 0.2% DM and 40 mM imidazole. MloK1 was eluted with buffer containing 500 mM imidazole. To maintain the integrity of MloK1, 0.2 mM cAMP (Fluka) was present throughout the whole purification process. DM-solubilized MloK1 sample was then mixed with *E. coli* polar lipid extract (Avanti Polar Lipids) at a lipid-to-protein ratio of 0.8-1.0 and

dialyzed against detergent-free buffer (20 mM KCl, 20 mM Tris-HCl pH 7.6, 1 mM $BaCl_2$, 1 mM EDTA, 0.2 mM cAMP). Two-dimensional crystals of the lipid-embedded protein were obtained within 5 days.

7.2.2 Cryo EM grid preparation and imaging

Approximately 4 μl of the MloK1 2D crystal solution (~0.8 mg/ml) were applied to glow-discharged Quantifoil holey carbon grids (R3.5/1, Cu 400 mesh, Quantifoil Micro Tools GmbH, Grosslöbichau, Germany) coated with an additional thin amorphous carbon layer. After 3.5 second-blotting, grids were flash frozen in liquid ethane, using an FEI Vitrobot IV with the environmental chamber set at 90% humidity and 20°C. 2D crystals of MloK1 were imaged in an FEI Titan Krios TEM operated at 300 keV, and recorded by a Gatan K2-Summit direct electron detector. Images were collected manually in electron-counting mode at a nominal magnification of ×22,500 and a calibrated pixel size of 1.3 Å. Defocus varied from -0.5 to -2.0 μm. Each image was dose-fractionated to 40 frames (16 sec in total, 0.4-sec frames). The dose rate was set to ~5 counts/sec/physical-pixel (~2.8 $e^-/s/Å^2$) leading to a total dose of ~45 $e^-/Å^2$. Movie frames were aligned with MotionCorr [Li et al., 2013] and preprocessed on the fly with 2dx_automator [Scherer et al., 2014b].

7.2.3 Image processing

Over 1200 manually recorded cryo-EM real-space image stacks (termed “movies”) were whole-frame drift-corrected, using MotionCorr Version 2.1 [Li et al., 2013], and subjected to automated Fourier transforming, lattice finding, lattice spot indexing, 2D crystal masking, unbending, and map generation, all within 2dx_automator [Scherer et al., 2014b]. From these, the best 361 images were processed further with the 2dx software package [Arheit et al., 2013; Gipson et al., 2007a,b], using newly developed image processing algorithms (Chapter 5). These enabled the local correction of the contrast transfer function of the electron microscope in stripes on the original frames of the movies, prior to subsequent processing steps such as unbending. A newly-developed movie-mode 2D crystal unbending was used. The algorithm traces each individual 2D crystal unit cell through the image stack of one movie, and unbends the individual 2D crystals frames smoothly, while allowing for spline-correlated yet locally varying drift trajectories of unit cells. Unbent movie frames were then subjected to electron-dose dependent B-factor resolution filters, and movie frames were averaged into 2D maps. These were evaluated for the amplitudes, phases, and figure-of-merit (FOM) values for each Fourier reflection. Newly developed handling of FOM statistics allowed the very large number of reflections with very low signal-to-noise ratios to be included before averaging. The above process was applied to 5×5 tiles within each 4kx4k pixel movie, enabling the local refinement of the sample tilt geometry over these 25 locations within each tile. Conventional lattice line fitting was replaced by weighted backprojection, to translate the amplitude, phase and FOM values obtained into a 3D map. The resulting 3D map was refined

Crystal plane group symmetry	p4212
Crystal unit cell parameters	$a = 135.0$Å, $b = 135$Å, $\gamma = 90°$
Range of defocus	$0.75 \ldots 4.3 \mu m$
Tilt range used	$0° \ldots 55°$
In plane resolution cutoff	3.5Å
Vertical resolution cutoff	3.5Å

In full 2D crystal images:

Number of 2D crystal images in 2D crystal dataset	346
Number of MloK1 tetramers in 2D crystal dataset	>3000000
Number of observed reflections	1074513
Number of observed unique reflections	195147
Number of observed unique reflections in asymmetric unit	23834

In 5×5 sub-tile images of crystal images:

Number of 2D crystal images in sub-tile dataset	6361
Number of MloK1 tetramers in sub-tile dataset	>3000000
Number of observed reflections	6901357
Number of observed unique reflections	1388385
Number of observed unique reflections in asymmetric unit	23102

TABLE 7.1. **Statistics of the final MloK1 map:** Detailed statistics involved in the generation of final map including symmetry, number of images, defocus range, etc. are provided in this table.

by shrinkwrap optimization, which subjects the map to iterative application of constraints in real and Fourier space (Chapter 6).

The resolution of the final map is estimated as better than 5Å, documented by the visibility of alpha-helical threads and separated horizontal beta strands. To analyze the local variations in resolution of the map after iterative shrink-wrap projective constraint optimization refinement, the final map was analyzed by the program ResMap [Sievers et al., 2011], which indicates strong variations in local resolution in the range between 3.5 Å and 5 Å (Appendix C, Figure C.2). Statistics on the final map are summarized in Table 7.1.

7.2.4 Model building

The initial model was obtained using Modeller [Šali and Blundell, 1993]; in particular, the missing fragments were generated for the previously published PDB 4CHV model. This starting model was refined using the Rosetta for cryo-EM package [DiMaio et al., 2015]. The symmetry of the channel was restrained during optimization runs (performed following the package tutorial [Wang, 2015]). A model with a high fit score to the EM map and a low energy, as defined by the

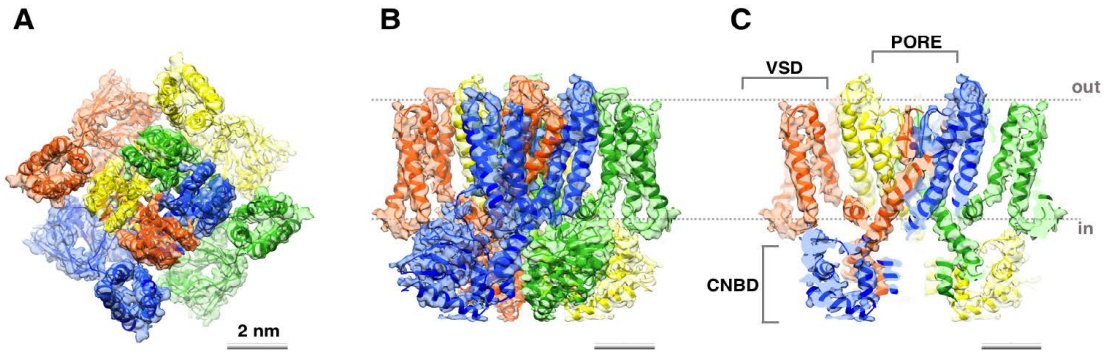

FIGURE 7.1. **Cryo-EM map of MloK1 channel tetramer with cAMP:** (A) Extracellular top view of one tetramer. The individual monomers are in different colors (scale bar, 2nm). The voltage sensor domains and the CNBDs wrap around the adjacent subunit pore domain. CNBDs are in fainter shades as they are located below the transmembrane domains (B) Side view; (C) Cross-section through middle of the channel shown in (B). The new atomic model is fitted into the density. Main channel sections are indicated on the figure. Dashed line in B and C indicates the membrane level.

Rosetta force field, was selected from 100 Rosetta models generated and refined further. Several rounds of manual refinement with Coot [Emsley et al., 2010] and global optimization with Phenix (real_space_refine method [Afonine et al., 2013]) were carried out. Secondary structure constraints were imposed to keep helices and beta sheets in form during the global optimization.

7.3 Results

7.3.1 Cryo-EM 2D Crystallography and Model Generation

Purified MloK1 protein was crystallized in the presence of its ligand, cAMP, as described in Kowal et al. [2014]. 2D crystals were adsorbed to holey carbon film grids, vitrified by plunge freezing, and cryo-EM images were recorded using a high-end FEI Titan Krios cryo-EM instrument equipped with an energy filter and a K2 Summit direct electron detector. Projection images of the micrometer-large 2D crystals of MloK1 showed them to have p4212 crystal symmetry. In computed Fourier transforms they rarely showed diffraction to better than 12 Å and the best resolution was only 10 Å. However, the very large dataset of over 1200 movies recorded, and a novel suite of image processing tools implemented in the 2dx package, allowed a 3D map to be obtained at 4.5 Å resolution from these images (Figure 7.1 and Table 7.1). The newly-developed image processing algorithms are described in detail in the methods section.

The map displays clear high-resolution features such as alpha-helical turns and pitches for the

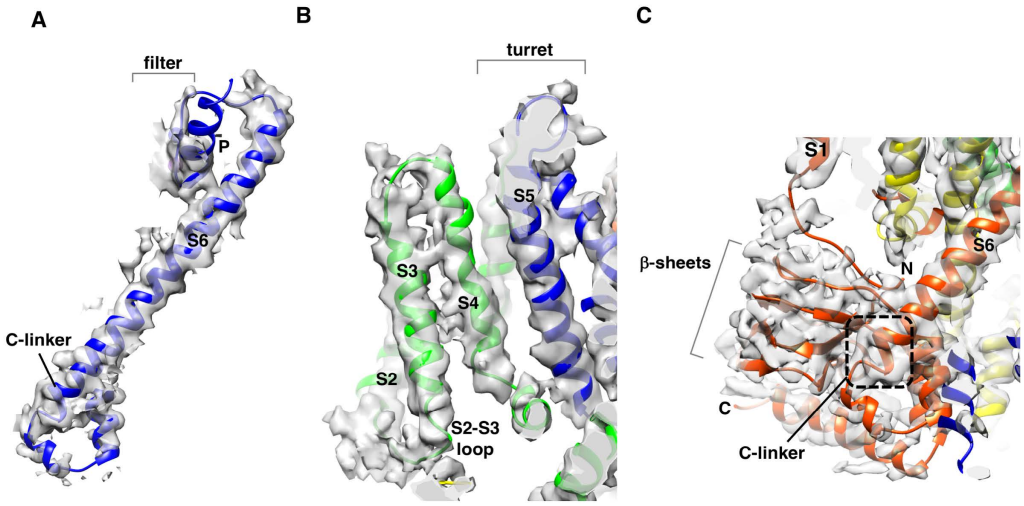

FIGURE 7.2. **Structural details of different MloK1 channel features:** (A) Long inner pore helix composed of helix S6 continued with the C-linker. Model is in blue and density in grey. (B) Densities between helices S3 and S4, labeled. Model in green for S3 and S4, blue for S5 and S6, to indicate different subunits in the tetramer, and density in grey. (C) Cross-section through the cyclic nucleotide-binding domain. β-sheets are indicated; helices and both termini of MloK1 are labeled as N and C. Color coded as in Fig. 1.

lipid-embedded helices, and resolves connecting loops and detailed features such as horizontally arranged beta-sheets in the CNBDs that unambiguously determine their orientation, although side-chain densities are only rarely observed (Figure 7.2).

In order to obtain a more accurate 3D model, we fitted the previously published MloK1 model (PDB 4CHV) into to the final cryo-EM density. Flexible fitting of this model yielded a final atomic model for the full-length MloK1 protein that is in good agreement with the cryo-EM density (Figure 7.1B). The quality of the final model is highest in the transmembrane region, where it reproduces all the helical turns and all the loops (Figure 7.2A and B). The loops within the CNBD region are not well visible, but the beta-sheets fit nicely into the map (Figure 7.2C).

7.3.2 Structural features of MloK1 and comparison with the earlier model and the structures of HCN1 and TAX-4

In the new high-resolution MloK1 map, the structures of the VSDs and CNBDs are quite similar to the X-ray structures of the transmembrane part of MloK1 [Clayton et al., 2008] (PDB 3BEH) and CNBD with cAMP [Lolicato et al., 2014] (PDB 4KL1), respectively. However, as already reported for our lower resolution structure [Kowal et al., 2014], the intracellular opening at the

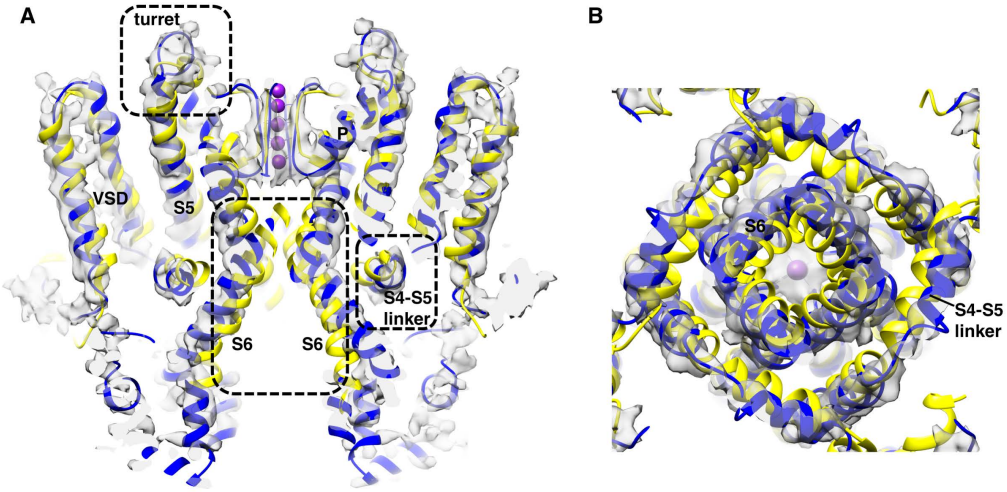

FIGURE 7.3. **Helix bundle crossing and selectivity filter:** (A) Overview of the X-ray structure of transmembrane region of MloK1 (PDB 3BEH [Clayton et al., 2008]), yellow ribbons and purple ions) and new EM (blue) models superimposed on the cryo-EM map (grey). Three areas are highlighted: S6 helix-bundle crossing, turret formed by the S5 helix and part of the P-loop, S4-S5 linker. (B) Intracellular view of a cross-section through middle of the pore shown in (A).

"putative" S6 helix bundle region (the best resolved helix in the transmembrane region) is larger in our EM structure than in the X-ray structure (Figures 7.2A, 7.5A and 7.5B). It seems that the size of the opening of the MloK1 pore at the intracellular side is not defined solely by the state of liganding (since both are determined in the presence of saturating cAMP concentrations) but it could also depend on the different crystal packing and lattice forces, as well as lipids, which are present in the 2D crystals of MloK1 used for the EM structure, but not in the X-ray structure (PDB 3BEH). Lipids may influence the degree of tilting of the pore-forming S6 helices with respect to the fourfold axis of the tetramer, and thus set the size of the intracellular opening. The same wide opening in the helix bundle crossing region was observed in the recently published full-length HCN1 and TAX-4 structures.

As also observed in the previous, lower resolution MloK1 EM structure and the X-ray structure of the transmembrane regions of MloK1, the S1-S4 voltage sensor domain wraps around the adjacent pore-forming subunit via the S4-S5 linker that connects the two. The S4-S5 linker forms a helix that lies parallel to the membrane and is implicated in the coupling between the voltage signal and the channel gate. The position of the S4-S5 linker in the MloK1 EM structure resembles more that of the crystal structure of the voltage-gated Kv1.2/Kv2.1 chimera channel (PDB 2R9R, [Long et al., 2007]) than what had been determined by X-ray crystallography in the absence of lipids for MloK1 [Clayton et al., 2008]. MloK1 in our EM map shares with Kv1.2 a

large intracellular opening that is due to the outward tilting of the S6 helices, which displace the S4-S5 linker upwards. The S3-S4 paddle region is well resolved in the MloK1 EM structure, allowing a clear identification of the helix tilts (Figure 7.2B).

The higher resolution of our new MloK1 structure reveals the connections between the ligand-binding domain and the channel pore, suggesting a potential gating mechanism. The pore-lining inner helix of MloK1 is a continuous helix composed of the S6 transmembrane domain and the C-linker, and extends way beyond the intracellular membrane boundary (Figures 7.2, 7.3). At the end of the C-linker and beginning of the CNBD, the helix breaks at a Pro residue and then turns sharply in the opposite direction a few residues later at another Pro residue. Both Pro residues are conserved in all HCN channels and MloK1 (Fig 7.3). The loop formed by the turns (which we will call a "siphon") directly connects the long inner helix to the CNBD. This suggests an attractive model for channel gating, where conformational changes at the CNBDs (relatively small movements) are efficiently transmitted to the channel pore, via the siphon and the long helix, which acts like a lever. In contrast to HCN1 and TAX-4, MloK1,Äôs siphon seems more tense and is in the less relaxed state. Additionally the two prolines present at the beginning and end of the siphon make its shape more edgy than in the CNG TAX-4 channel, which is missing prolines.

In our EM map, the liganded CNBD does not hang down at the end of the S6 helix, but points up towards the membrane to interact directly with the intracellular S2-S3 loop that connects two of the membrane-embedded helices of the VSD domain of the neighboring subunit (Figure 7.4). The U-turn in the structure is mediated by the "siphon", suggesting a mechanism of channel gating. The S2-S3 loop is well resolved in our high-resolution MloK1 structure. It makes crystal contacts with an MloK1 tetramer in the neighbouring unit cell on one side, and interacts with the CNBD of the neighboring subunit within the same tetramer on the other (Figure 7.4). In the latter case, the interacting residues are Arg69 (located at S2-S3 loop, subunit A) and Glu267 (located at CNBD, subunit B) suggesting possible salt bridge formation in the liganded channel. Furthermore, the intracellular N-terminal loop that precedes helix S1 also appears to make direct intra-subunit contact with the liganded CNBD via a possible hydrophobic interaction. A similar interaction was previously proposed for CNG channels[Gordon et al., 1997] based on electrophysiological data.

The pore turrets, i.e., the extracellular loops between the S5 transmembrane helix and the pore helix, are well-resolved and protrude away from the membrane plane in this high-resolution EM structure (Figures 7.1, 7.2, 7.5A), unlike in our previous structure and the X-ray structure where they lay flat on top of the channel (Figure 7.5). Further, the CNBD could now be accurately fit within the higher resolution EM density, constraining its orientation with respect to helix S6 and to the rest of the channel (Figure 7.3A and B).

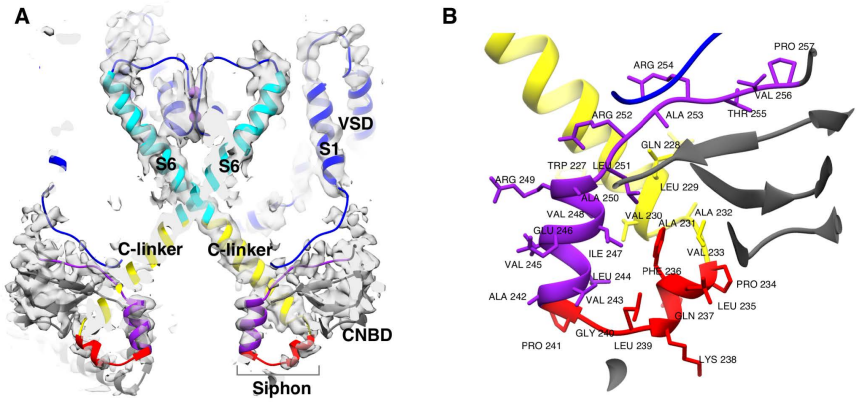

FIGURE 7.4. **MloK1 siphon and C-linker structures:** (A) Cross section through the middle of the MloK1 tetramer showing just two opposing subunits. Inner S6-helix is shown in cyan, C-linker (residues 212-233) in yellow, siphon structure (residues 234-241) in red and CNBD in purple until Pro 257 and then grey, the selectivity filter and the VSDs are blue. Density is grey. (B) Enlarged view of the "siphon" area with highlighted, labeled amino acid residues in stick representation. The side-chains are only shown for orientation purposes; the resolution is not enough for specific assignments to be made.

7.4 Discussion

We present the 5Å resolution structure of the MloK1 cyclic nucleotide-modulated potassium channel from 2D crystals in lipids and in the presence of cAMP. The high resolution allows us to glean new insights into the architecture and gating of this channel and draw comparisons with the eukaryotic counterparts.

We consider the relatively high resolution of 4.5Å obtained here from 2D crystals diffracting to not even half that resolution to be a technological feat. In order to reach this resolution, we had to partially abandon conventional 2D crystallographic image processing approaches in favor of more particle oriented masking, unbending, and image weighting methods. Due to the relatively small size (~160 kDa) of the tetrameric MloK1 complexes (particles) and their apparent structural flexibility, single particle cryo-EM imaging of detergent-solubilized particles was not successful in our hands, making cryo-EM imaging of the poorly-ordered 2D crystal the only feasible approach.

The CNBD of MloK1 is highly homologous to the CNBDs of both CNG and HCN channels, but the C-linker in the latter is much longer[Brams et al., 2014], suggesting that despite the overall similarity in architecture and individual domains, the gating of eukaryotic channels is

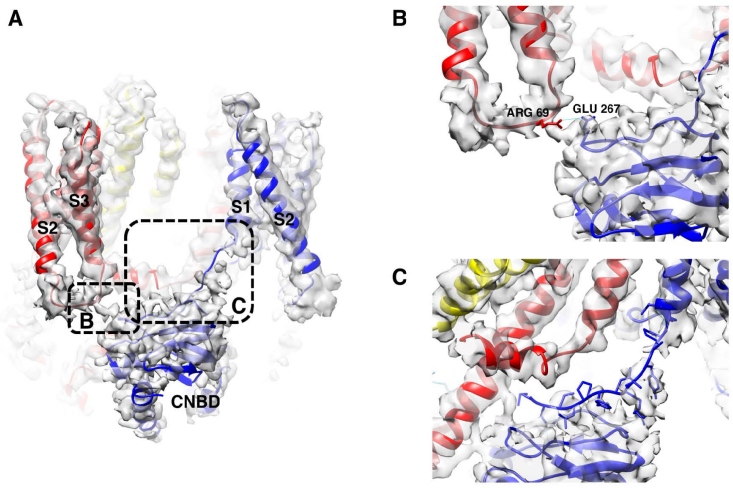

FIGURE 7.5. **Interactions between transmembrane domains and CNBDs:** (A) Overview of MloK1 CNBD's inter- and intra-subunit interactions. (B) The CNBD likely interacts with the S2-S3 loop of the adjacent subunit (red) via a salt bridge formed between Arg 69 (S2-S3 loop) and Glu 267 (CNBD). (C) The N-terminal amino acid chain (before helix S1, residues 1-15) lies on top and on the inner side of the CNBD of the same subunit (blue). The N-terminus is rich in hydrophobic amino acids (Val, Leu, Pro, Phe, Leu, Ile). Color coded as in Figure 7.1.

likely to be more complex than that of MloK1.

MloK1 shows the CNBDs connected to the S6 helix via a helix-turn-helix motif with two conserved prolines at the turns (Figure 7.3), here termed siphon. It is attached to the long inner helix that extends down far beyond the membrane boundary. The position of the siphon at the end of this lever introduces a U-turn, making it possible for the ligand-bound CNBD to get close to the membrane and make contact with the loops connecting the transmembrane helices of the voltage sensor, thus likely making the tetrameric complex more stable. It is conceivable that upon ligand unbinding, the conformational change occurring in the CNBD propagates to the siphon region, allowing a conformational switch at the level of one or both of the conserved prolines. This siphon conformational switch might cause the long lever formed by the inner helix to move and lead to a break of the observed interaction between the CNBD and the voltage sensor. This would lead to increased mobility of the CNBD, as it would be moved away from the membrane. In agreement with this idea, unliganded MloK1 CNBDs were found to be "detached" from the membrane in both our lower resolution cryo-EM MloK1 structure and by imaging the heights of unliganded and liganded MloK1 complexes by atomic force microscopy (AFM) [Kowal et al., 2014; Rangl et al., 2016]. Furthermore, the unliganded MloK1 CNBDs of bilayer-embedded full-length channels were previously found to undergo "blinking" in high-speed AFM measurements; the

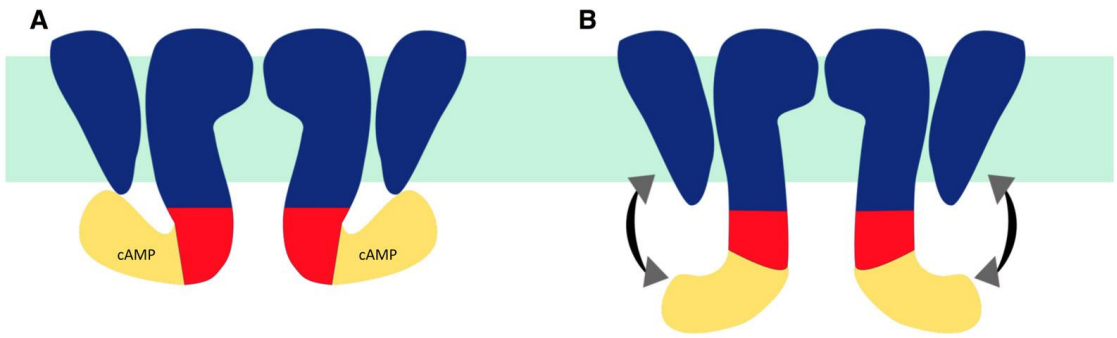

FIGURE 7.6. **Cartoon illustrating a proposed gating model in MloK1:** (A) When cAMP is bound, the "siphons" (red) are bent and the CNBDs (yellow) interact with the S2- S3 loop of the voltage sensor of the adjacent subunit, while being in direct contact with the N-terminus of its own subunit, as shown in the current structure. (B) We propose that in the absence of cAMP, a CNBD conformational change leads to a change in the siphons bringing the CNBDs in a conformation more distant from the membrane plane with a motion suggested by the arrows. Transmembrane domains are in navy, membrane in light green.

CNBDs oscillated between conformations where they were close to and far from the membrane on a millisecond time scale [Rangl et al., 2016]. All these previous findings can be rationalized now that the simple helix-turn-helix structure connecting the inner helix with the CNBD is visible in our high resolution MloK1 structure (Figure 7.3 and Figure 7.6). The proposed mechanism and function of the siphon structure allow the liganded CNBDs to interact with the voltage sensors.

Interestingly, both of the two recently determined structures of HCN1 in complex with cAMP [Lee and MacKinnon, 2017] and TAX-4 CNG in complex cGMP [Li et al., 2017] show the siphon structure observed in MloK1, but their CNBDs are in a position about 1 nm further down from the membrane plane, and rotated by 45° around the central channel axis. Moreover, the sequence forming the siphon structure in MloK1 displays strong similarity with the same region in HCN channels (but not CNG channels), suggesting a common feature in the gating mechanisms between MloK1 and HCN channels, despite the different C-linker lengths. Compared to HCN1 and TAX-4, MloK1's siphon is in a tense, less relaxed state. It is possible that this feature is important in the transmission of the nucleotide modulation signal in MloK1.

Both, the HCN1 and the CNG channels are in non-domain-swapped conformations with regard to their VSDs, which are adjacent to the S5/S6 pore-forming helices of the same monomer. In contrast, MloK1 is in the conventional domain-swapped conformation, where the VSD is adjacent to the neighboring monomer's pore-forming helices, connected by a horizontal S4/S5 linker helix. This is interesting, suggesting that the mechanism for MloK1 channel gating has features in common with the gating of voltage-gated potassium channels such as Kv1.2, which displays the domain-swapped configuration of the VSDs. Additionally, we observed that in the TAX-4 structure (PDB 5H3O) each CNBD may be within reach of the S2-S3 loop of the

neighboring subunit. Interestingly, in the HCN1 model (PDB 5U6P) the S1-S2 loop is as well close to the CNBD.

Without a high-resolution structure in the absence of ligand, it is difficult to identify the gate that opens and closes the channel pore in MloK1, despite our previous finding that the low-resolution unliganded MloK1 structure looked very similar to the liganded structure in the pore region. We can, however, state that the opening at the intracellular constriction is larger in our EM structure of the liganded MloK1 than in the X-ray structure of the MloK1 transmembrane region[Clayton et al., 2008]. The presence of lipids in our EM structure likely modifies the extent to which the inner helices are tilted in the open state, leading to a larger pore opening. We predict that the position of the inner helices will be somewhat different in the closed state of the channel due to their direct connection with the CNBDs, which seem likely to change conformation upon losing the ligand. However, whether such a movement will actually cause a constriction on the intracellular side of the pore or whether the selectivity filter is the ultimate gate remains to be seen.

PART IV

CONCLUSION

CHAPTER 8

Final remarks

Cryo-EM is a technique in structural biology that uses the electron beam transmitted after interaction with the specimen to record its atomic structural details. The new direct electron detectors directly sense and count the electrons improving the signal to noise ratio and a fast read-out speed enables to record movies instead of images. This helps in reducing the motion effects that arise during recording. These hardware advancements when topped with the advancements in image processing algorithms like maximum likelihood methods and movie mode corrections have lead to the resolution revolution in the field of electron microscopy. The features in biological structures can now be resolved to sub-atomic resolutions by cryo-EM. This makes cryo-EM the method of choice for many structural biologists. One of the classical methods in electron microscopy is 2D electron crystallography, which is used to determine the electron density maps by imaging 2D crystals of desired biological structures (mainly membrane proteins). Electron crystallography can be used to study small membrane proteins in their native environment. It can also become handy to capture different conformational states of a protein. Obtaining highly-ordered 2D crystals is difficult and time-consuming. However, 2D crystals diffracting to only 10-12 Å can be prepared relatively conveniently in most cases. The major problems that resist high resolution in these crystals are: (i) radiation damage to crystals while recording, (ii) out of plane crystal distortions, especially for titled images, (iii) CTF correction schemes, and (iv) the problem of missing cone.

The aim of this thesis was to develop tools and techniques in cryo-EM that assists in image processing and helps in achieving high resolution in 2D electron crystallography. Software tools, namely EMKIT and Focus, facilitates the image processing in cryo-EM. EMKIT provides an easy to use C++ interface with in-built classes and methods. It provides flexibility to accomplish multidimensional image processing tasks involved in cryo-EM with focus on performance and at the same time providing the ease to write code. The library expands STL and supports multidimensionality using the Tensor and its associated classes. This multidimensionality helps to represent commonly used objects in cryo-EM including real spaces, complex half spaces, etc. Furthermore, methods such as file input/output, Fourier transformation using FFTW library, object converters, statistical calculation using iterators and Fourier filtering are implemented. Future work includes optimization of the toolkit for high performance computing including parallelization using C++11 threads, MPI and CUDA.

Focus provides a user-friendly interface between the data collection and the data processing in cryo-EM. It can use the available software resources to accomplish image processing tasks in a high throughput manner. Focus integrates convenient importing of the data into its environment, processing it through a user-defined pipeline, monitoring the imported and processed data through a web server and flexible exporting of the data. Focus also incorporates ready to use scripts that allows to accomplish image processing tasks. Because of its many features, Focus will increase the productivity of the data collection in electron microscopy significantly. Future work include integrating complete single particle reconstruction pipeline which can, at present, be run

in an automated manner without much manual interaction using packages such as FREALIGN. This would allow to generate a 3D reconstruction while recording. Adding a functionality to run high-throughput nodes on multi-node system would be quite useful and would further increase the productivity. There is also a need to accelerate some of the processes, such as Fourier cropping, using GPUs.

New methods have been developed for the 2D electron crystallography including movie-mode unbending, which performs frame-wise unbending in the recorded movie frames; refinement over sub-tiles of the frames in order to locally refine the crystal tilt geometry and electron beam tilt within different tile locations within the images; analysis of different CTF correction schemes; a shrinkwrap projective constraint optimisation refinement for approximating the Fourier data in the region of missing cone. Using the 2D crystals and the application of above stated novel methods to these crystals, a high-resolution structure of MloK1 was obtained. MloK1, a cyclic nucleotide-modulated potassium channel from *Mesorhizobium loti*, is a homologue of human HCN (Hyperpolarization-activated Cyclic Nucleotide-gated) channels important for signal transduction and pacemaking in eukaryotes. The structure, obtained in the presence of its ligand, cAMP, and in a lipidic environment, allows us to build a complete atomic model serving as a basis for understanding gating in cyclic nucleotide-modulated channels.

Supplementary information for "Focus: The interface between data collection and data processing in cryo-EM"

Mode: *2D Electron Crystallography*

Overview	View #1	View #2	View #3	View #4
Image Overview	Image before drift correction	FFT before drift correction	Image after drift correction	FFT after drift correction
Drift Overview	Image after drift correction	FFT after drift correction	Drift trajectory	Thon rings fit
Processing Overview	Thon rings fit	Unbending profile	IQ plot	Final map
Merge Overview	Final map	Reference map	Half-half map	Thon rings fit

Mode: *Single Particle*

Overview	View #1	View #2	View #3	View #4
Image Overview	Image before drift correction	FFT before drift correction	Image after drift correction	FFT after drift correction
Drift Overview	Image after drift correction	FFT after drift correction	Drift trajectory	Thon rings fit
Particles Overview	Background subtracted image	FFT after drift correction	Drift trajectory	Thon rings fit

Mode: *Drift Correction, Electron Tomography*

Overview	View #1	View #2	View #3	View #4
Image Overview	Image before drift correction	FFT before drift correction	Image after drift correction	FFT after drift correction
Drift Overview	Image after drift correction	FFT after drift correction	Drift trajectory	Thon rings fit

TABLE A.1. **Overview provided by the Project Library:** Project Library provides various overviews depending on the mode of the project. Each of these overviews contains four different thumbnails (or views) related to the image under consideration.

	All modes	Specific for mode: *2D Electron Crystallography*	Specific for mode: *Single particle*
All images	• Display coordinate information • Zoom • Adjust contrast	• View tilt axis	
Specific to real space images	• Selection based FFT	• Polygon selection	• View particles
Specific to Fourier space images	• View CTF	• Show phase origin • View peak list • Spot selection • Lattice refinement • View lattice	

TABLE A.2. ***fViewer* functions and options:** *fViewer* is a fast MRC file viewer with options and functions listed in this table.

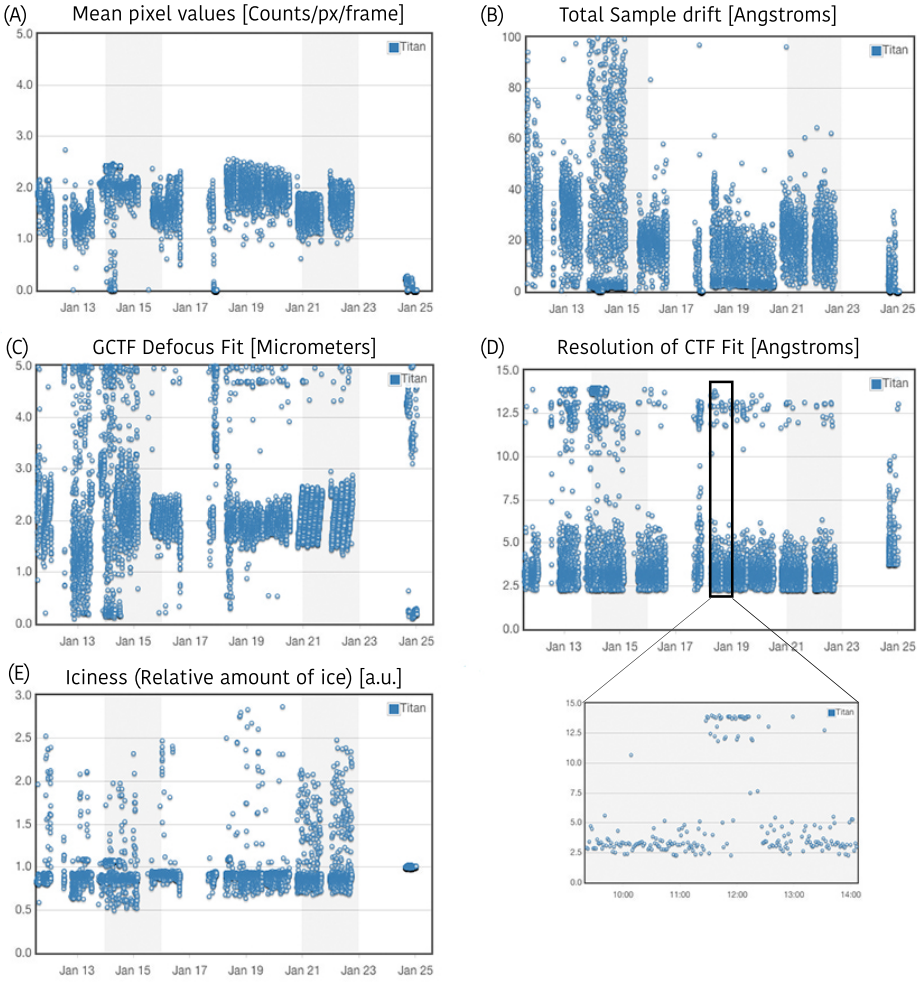

FIGURE A.1. **Time series showing parameters calculated from the recorded images:** Various parameters from the recorded images are calculated and pushed to a server. This data is then plotted over the time and shown on the remote monitoring webpage. (A) Mean pixel values; a reduced mean pixel count would mean that darker images are being recorded. (B) Total sample drift; large values correspond to higher drift and can arise from mechanical errors. (C) Defocus calculated using GCTF [Zhang, 2016]; the defocus should behave as set during automation. (D) Resolution of the CTF fit calculated by GCTF; larger values correspond to degraded quality of the recorded images. The inset shows that all images collected after 11:30 had large values. When this was noticed the data collection settings were checked again, and the resolution was in the normal range one hour after the problem first arose. (E) Iciness, i.e., the relative amount of ice in the image; if this ratio increases, more ice is being encountered in the collected images.

APPENDIX B

Supplementary information for "Image processing techniques for high resolution 2D-electron crystallography"

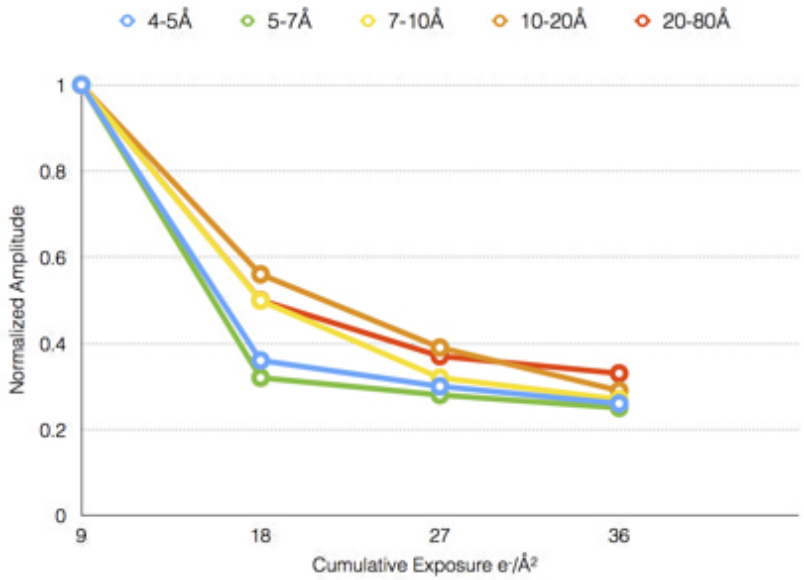

FIGURE B.1. **Dose effects studied as described in Bammes et al. [2010]:** The Fourier space was arbitrary divided into 5 "resolution intervals": 4-5, 5-7, 7-10, 10-20, and 20-80Å. For each zone the mean of all non-zero normalized Fourier amplitudes of all peaks with $IQ < 7$ was calculated. The normalized amplitude of the reflection with Miller indices (h,k) is defined as $NA_{(h,k),i} = \frac{AMP_{(h,k),i}}{AMP_{(h,k),0}}$, where $i = 0$ is the first image of an exposure series with accumulated electron dose of 9 $e^-/Å^2$, respectively for $i = 1$ the second image with accumulated dose of 18 $e^-/Å^2$. Diffraction spots of three different non-tilted crystals were analyzed. As we only measured a slightly faster dose-dependent decay of diffraction spots as previously reported by [Baker et al., 2010; Bammes et al., 2010] the previous results on thin 3D crystals can be used as reasonable approximation. Additionally movie-mode unbending provides the functionality to determine the dose-effects for any new project, which allows the future user to fine-tune the damage compensation and to further study the behavior of 2D lipid membrane crystals under the electron beam.

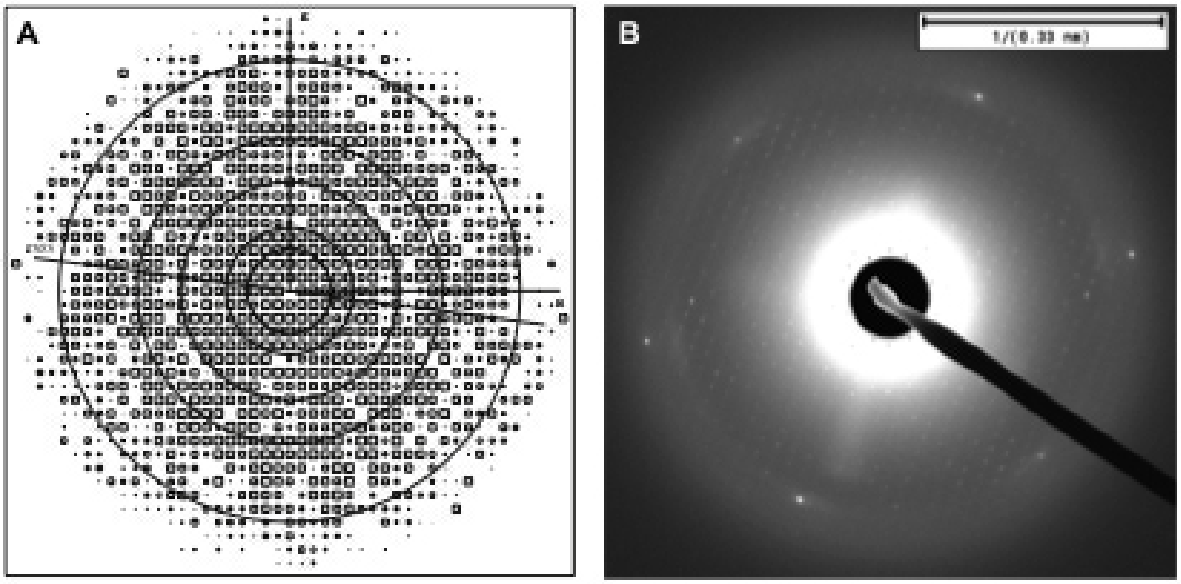

FIGURE B.2. **Comparison of a computed and a recorded diffraction pattern of the same kind of remarkably well ordered 2D crystal:** The crystals contain the bacteria outer membrane receptor FhuA with an additional compound bound to it (data unpublished). (A) Canonical IQ plot of a non-tilted movie-mode unbent image recorded on a Titan Krios equipped with a Gatan K2 summit, Nyquist frequency of the plot is a 2.68Å, the resolution circles are at 18Å, 12Å, 7Å, 5Å and 3.3Å. (B) Electron diffraction pattern of the same sample recorded CM200 equipped with a TVIPS F416 CMOS camera. Both the computed and the measured diffraction pattern show spots up to the same resolution range. Due to the different detectors used for data acquisition (movie-mode unbending required a DED, which is not suited for electron diffraction exposures) a quantitative comparison is difficult. Nevertheless, these data suggest that DEDs combined with the latest drift-correction approaches are able to record high quality data that were previously for 2D crystals only attainable by electron diffraction.

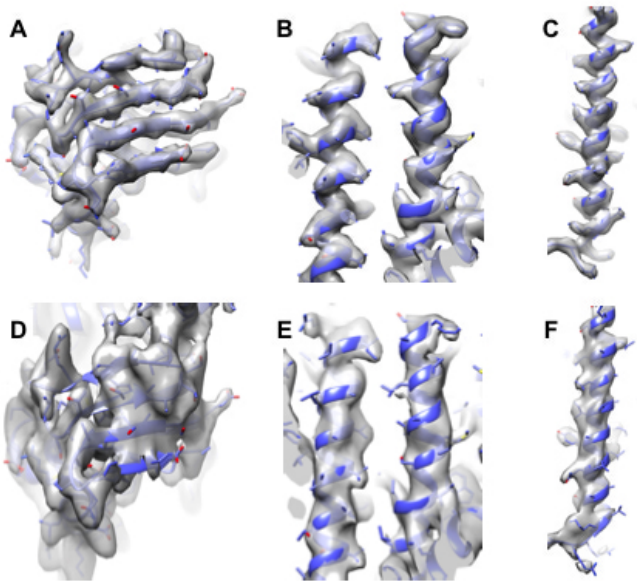

FIGURE B.3. **Impact of the missing cone to different areas of the protein structure:** We used e2pdb2mrc.py from EMAN2 [Tang et al., 2007] to convert the atomic model (PDB-4CHW) into a 5Å density map. A python script, which was augmented by image processing functions implemented in SPARX [Hohn et al., 2007], was written to simulate the effect the missing cone. Simulated density maps not affected by missing cone artifacts are shown in the top row: (A) CNDB of the ion-channel, (B) trans-membrane region of the selectivity filter and (C) S2-helix in the voltage-sensing domain. Bottom row (D-F) shows the same regions affected by a missing cone of 40°, i.e. completely sampled Fourier space up to 50° tilt. Negative effects of higher sample tilt on image quality were neglected.

APPENDIX C

SUPPLEMENTARY INFORMATION FOR "HIGH-RESOLUTION STRUCTURE OF THE MLOK1 K^+ CHANNEL"

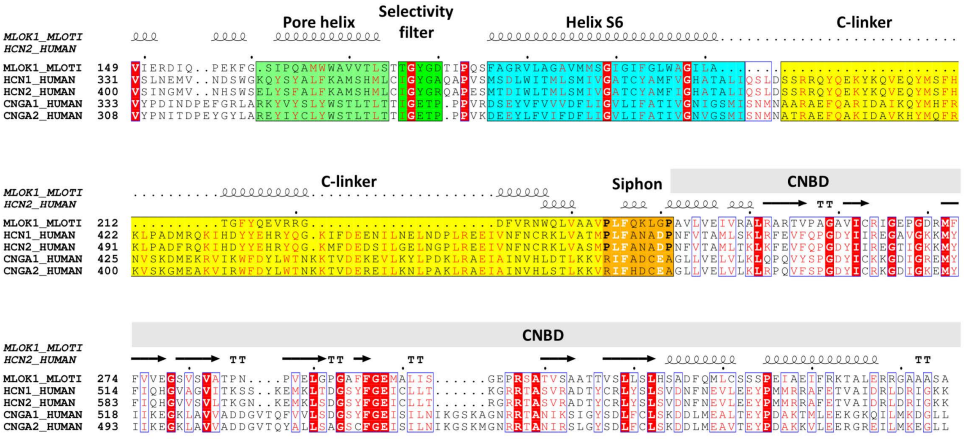

FIGURE C.1. **Sequence alignment of MloK1, HCN1, HCN2, CNGA1, and CNGA2 channels performed in Clustal Omega [Sievers et al., 2011], focusing on MloK1 residues 149-400:** Identical residues are shown in red blocks, while similar residues are colored in red font. Different block colors identify different domains labeled above: green belongs to pore helix and selectivity filter, blue to helix S6, yellow to C-linker and orange to siphon sequence. The conserved prolines in siphon sequence (orange block) are marked in bold. Secondary structure elements from X-ray structures of MloK1 transmembrane region (PDB 3BEH [Clayton et al., 2008]) and CNBD domain of HCN2 (PDB 2MPF [Lolicato et al., 2014]) are drawn above the alignment; α-helices are displayed as squiggles, β-strands are rendered as arrows and strict β-turns as TT letters. Alignment was visualized using ESPript [Robert and Gouet, 2014].

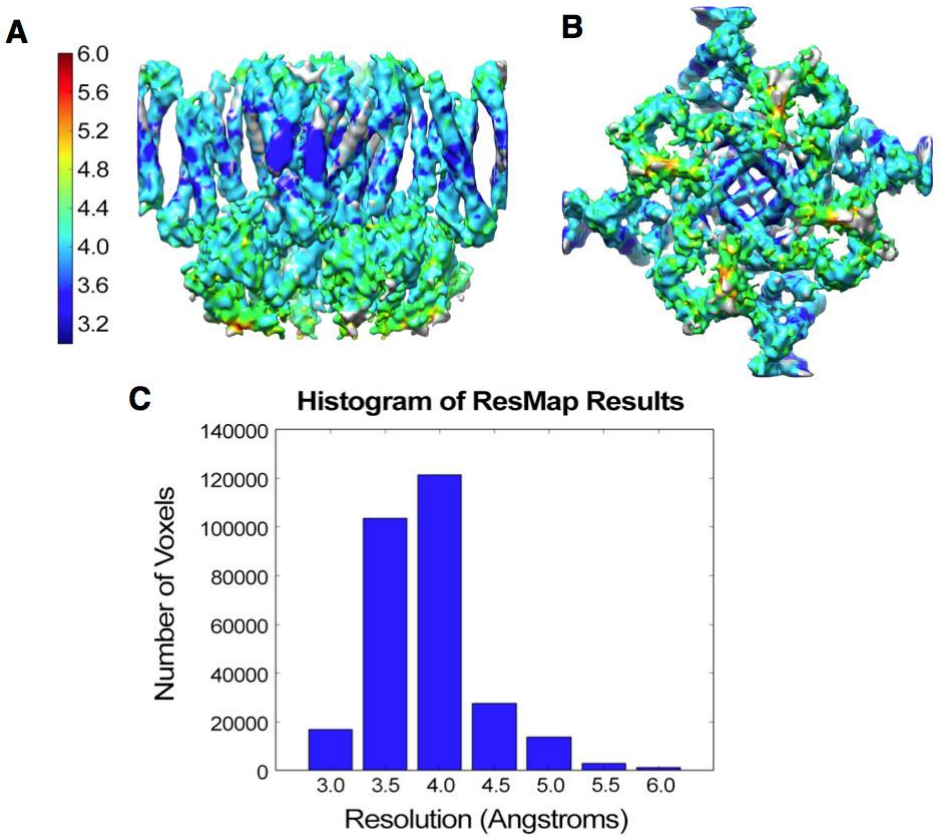

FIGURE C.2. **Analysis of local resolution with ResMap [Kucukelbir et al., 2013]:** (A) Side view of back-projected 3D reconstruction coloured with local resolution. (B) Volume showed in (A), rotated 90 degrees, intracellular view. (C) Voxel histogram with local resolutions.

BIBLIOGRAPHY

Abeyrathne, P. D., Chami, M., Pantelic, R. S., Goldie, K. N., and Stahlberg, H. (2010).
Preparation of 2D crystals of membrane proteins for high-resolution electron crystallography data collection.
In *Methods in Enzymology*, volume 481, pages 25–43. Elsevier Masson SAS.

Adams, P. D., Afonine, P. V., Bunkóczi, G., Chen, V. B., Davis, I. W., Echols, N., Headd, J. J., Hung, L. W., Kapral, G. J., Grosse-Kunstleve, R. W., McCoy, A. J., Moriarty, N. W., Oeffner, R., Read, R. J., Richardson, D. C., Richardson, J. S., Terwilliger, T. C., and Zwart, P. H. (2010).
PHENIX: A comprehensive Python-based system for macromolecular structure solution.
Acta Crystallographica Section D: Biological Crystallography, 66(2):213–221.

Afonine, P., Headd, J., Terwilliger, T., and Adams, P. (2013).
New tool:phenix.real_space_refine.
Computational Crystallography Newsletter, 4(2):43–44.

Agard, D. A. (1983).
A least-squares method for determining structure factors in three-dimensional tilted-view reconstructions.
Journal of Molecular Biology, 167(4):849.

Agard, D. A. and Stroud, R. M. (1982).
Linking regions between helices in bacteriorhodopsin revealed.
Biophysical journal, 37(3):589–602.

Alford, R. F., Koehler Leman, J., Weitzner, B. D., Duran, A. M., Tilley, D. C., Elazar, A., and Gray, J. J. (2015).
An Integrated Framework Advancing Membrane Protein Modeling and Design.
PLoS Computational Biology, 11(9):e1004398.

Allegretti, M., Mills, D. J., McMullan, G., Kühlbrandt, W., and Vonck, J. (2014).
Atomic model of the F420-reducing [NiFe] hydrogenase by electron cryo-microscopy using a direct electron detector.
eLife, 3:e01963.

Arheit, M., Castaño-Díez, D., Thierry, R., Gipson, B. R., Zeng, X., and Stahlberg, H. (2013).
Image Processing of 2D Crystal Images.
Methods in Molecular Biology, 955:171–194.

Bai, X.-C., Fernandez, I. S., McMullan, G., and Scheres, S. H. W. (2013).
Ribosome structures to near-atomic resolution from thirty thousand cryo-EM particles.
eLife, 2:e00461.

Baker, L. A., Smith, E. A., Bueler, S. A., and Rubinstein, J. L. (2010).
The resolution dependence of optimal exposures in liquid nitrogen temperature electron cryomicroscopy of catalase crystals.
Journal of Structural Biology, 169(3):431–437.

Bammes, B. E., Jakana, J., Schmid, M. F., and Chiu, W. (2010).
Radiation damage effects at four specimen temperatures from 4 to 100K.
Journal of Structural Biology, 169(3):331–341.

Bammes, B. E., Rochat, R. H., Jakana, J., Chen, D.-H., and Chiu, W. (2012).
Direct electron detection yields cryo-EM reconstructions at resolutions beyond 3/4 Nyquist frequency.
Journal of Structural Biology, 177(3):589–601.

Banaszak, L. J. (2000).
Foundations of structural biology.
Academic Press.

Barth, M., Bryan, R. K., and Hegerl, R. (1989).
Approximation of missing-cone data in 3D electron microscopy.
Ultramicroscopy, 31:365–378.

Bauschke, H. H., Combettes, P. L., and Luke, D. R. (2002).
Phase retrieval, error reduction algorithm, and Fienup variants: a view from convex optimization.
Optical Society of America, 19(7):1334–45.

Blow, D. M. and Crick, F. H. C. (1959).
The Treatment of Errors in the Isomorphous Replacement Method.
Acta Cryst., 12(1953):794–801.

Borshchevskiy, V. I., Round, E. S., Popov, A. N., Büldt, G., and Gordeliy, V. I. (2011).
X-ray-radiation-induced changes in bacteriorhodopsin structure.
Journal of Molecular Biology, 409(5):813–825.

Brams, M., Kusch, J., Spurny, R., Benndorf, K., and Ulens, C. (2014).
Family of prokaryote cyclic nucleotide-modulated ion channels.
Proceedings of the National Academy of Sciences of the United States of America, 111(21):7855–60.

Brilot, A. F., Chen, J. Z., Cheng, A., Pan, J., Harrison, S. C., Potter, C. S., Carragher, B., Henderson, R., and Grigorieff, N. (2012).
Beam-induced motion of vitrified specimen on holey carbon film.
Journal of Structural Biology, 177(3):630–637.

Campbell, M. G., Cheng, A., Brilot, A. F., Moeller, A., Lyumkis, D., Veesler, D., Pan, J., Harrison, S. C., Potter, C. S., Carragher, B., and Grigorieff, N. (2012).
Movies of Ice-Embedded Particles Enhance Resolution in Electron Cryo-Microscopy.
Structure, 20(11):1823–1828.

Castaño-Díez, D., Kudryashev, M., Arheit, M., and Stahlberg, H. (2012).
Dynamo: A flexible, user-friendly development tool for subtomogram averaging of cryo-EM data in high-performance computing environments.
Journal of Structural Biology, 178(2):139–151.

Cheng, A., Henderson, R., Mastronarde, D., Ludtke, S. J., Schoenmakers, R. H., Short, J., Marabini, R., Dallakyan, S., Agard, D., and Winn, M. (2015).
MRC2014: Extensions to the MRC format header for electron cryo-microscopy and tomography.
Journal of Structural Biology, 192(2):146–150.

Chiu, P.-L., Pagel, M. D., Evans, J., Chou, H.-T., Zeng, X., Gipson, B., Stahlberg, H., and Nimigean, C. M. (2007).
The Structure of the Prokaryotic Cyclic Nucleotide-Modulated Potassium Channel MloK1 at 16 Å Resolution.
Structure, 15(9):1053–1064.

Clayton, G. M., Altieri, S., Heginbotham, L., Unger, V. M., and Morais-Cabral, J. H. (2008).
Structure of the transmembrane regions of a bacterial cyclic nucleotide-regulated channel.
Proceedings of the National Academy of Sciences of the United States of America, 105(5):1511–5.

Combettes, P. L. and Trussell, H. J. (1990).
Method of successive projections for finding a common point of sets in metric spaces.
Journal of Optimization Theory and Applications, 67(3):487–507.

Craven, K. B. and Zagotta, W. N. (2006).
CNG and HCN Channels: two peas, one pod.
Annual Review of Physiology, 68(1):375–401.

Crowther, R. A., Henderson, R., and Smith, J. M. (1996).
MRC Image Processing Programs.
Journal of Structural Biology, 116(1):9–16.

de la Rosa-Trevín, J., Otón, J., Marabini, R., Zaldívar, A., Vargas, J., Carazo, J., and Sorzano, C. (2013).
Xmipp 3.0: An improved software suite for image processing in electron microscopy.
Journal of Structural Biology, 184(2):321–328.

de la Rosa-Trevín, J., Quintana, A., del Cano, L., Zaldívar, A., Foche, I., Gutiérrez, J., Gómez-Blanco, J., Burguet-Castell, J., Cuenca-Alba, J., Abrishami, V., Vargas, J., Otón, J., Sharov, G., Vilas, J., Navas, J., Conesa, P., Kazemi, M., Marabini, R., Sorzano, C., and Carazo, J. (2016).
Scipion: A software framework toward integration, reproducibility and validation in 3D electron microscopy.
Journal of Structural Biology, 195(1):93–99.

Desfosses, A., Ciuffa, R., Gutsche, I., and Sachse, C. (2014).
SPRING - An image processing package for single-particle based helical reconstruction from electron cryomicrographs.
Journal of Structural Biology, 185(1):15–26.

Deutsch, F. (1980).
Existence of best approximations.
Journal of Approximation Theory, 28(2):132–154.

Dietrich, U., Krüger, P., Gutberlet, T., and Käs, J. A. (2009).
Interaction of the MARCKS peptide with PIP2 in phospholipid monolayers.
Biochimica et Biophysica Acta (BBA) - Biomembranes, 1788(7):1474–1481.

DiMaio, F., Song, Y., Li, X., Brunner, M. J., Xu, C., Conticello, V., Egelman, E., Marlovits, T. C., Cheng, Y., and Baker, D. (2015).
Atomic-accuracy models from 4.5-Å cryo-electron microscopy data with density-guided iterative local refinement.
Nature Methods, 12(4):361–365.

Doerr, A. (2015).
Single-particle cryo-electron microscopy.
Nature Methods, 13(1):23–23.

Dolder, M., Engel, A., and Zulauf, M. (1996).
The micelle to vesicle transition of lipids and detergents, in the presence of a membrane protein: towards a rationale for 2D crystallization.
FEBS Letters, 382:203–208.

Dubochet, J. (2012).
Cryo-EM–the first thirty years.
Journal of microscopy, 245(3):221–4.

Dubochet, J. and McDowall, A. (1981).
Vitrification of pure water for electron microscopy.
Journal of Microscopy, 124(3):3–4.

Egelman, E. H. (2007).
The iterative helical real space reconstruction method: Surmounting the problems posed by real polymers.
Journal of Structural Biology, 157(1):83–94.

Emsley, P., Lohkamp, B., Scott, W. G., and Cowtan, K. (2010).
Features and development of Coot.
Acta Crystallographica Section D, 66(4):486–501.

Engel, A., Hoenger, A., Hefti, A., Henn, C., Ford, R. C., Kistler, J., and Zulauf, M. (1992).
Assembly of 2-D membrane protein crystals: Dynamics, crystal order, and fidelity of structure analysis by electron microscopy.
Journal of Structural Biology, 109(3):219–234.

Faruqi, A. R. and Subramaniam, S. (2000).
CCD detectors in high-resolution biological electron microscopy.
Quarterly Reviews of Biophysics, 33(1):1–27.

Fernández, J. (2008).
High performance computing in structural determination by electron cryomicroscopy.
Journal of Structural Biology, 164(1):1–6.

Fernández, J., Li, S., and Crowther, R. (2006).
CTF determination and correction in electron cryotomography.
Ultramicroscopy, 106(7):587–596.

Fernandez-Leiro, R. and Scheres, S. (2016).
A pipeline approach to single-particle processing in RELION.
bioRxiv.

Fernando, K. V. and Fuller, S. D. (2007).
Determination of astigmatism in TEM images.
Journal of Structural Biology, 157(1):189–200.

Fienup, J. R. (1978).

Reconstruction of an object from the modulus of its Fourier transform.
Optics letters, 3(1):27–9.

Fienup, J. R. (1982).
Phase retrieval algorithms: a comparison.
Applied optics, 21(15):2758–69.

Förster, F. and Hegerl, R. (2007).
Structure Determination In Situ by Averaging of Tomograms.
In *Methods in cell biology*, volume 79, pages 741–767.

Frank, J. (1975).
Averaging of low exposure electron micrographs of non-periodic objects.
Ultramicroscopy, 1(2):159–162.

Frank, J. (2006).
Three-dimensional electron microscopy of macromolecular assemblies.
Oxford University Press.

Frank, J. (2017).
Advances in the field of single-particle cryo-electron microscopy over the last decade.
Nature Protocols, 12(2):209–212.

Fujiyoshi, Y. (1998).
The structural study of membrane proteins by electron crystallography.
Advances in Biophysics, 35:25–80.

Fujiyoshi, Y. (2011).
Electron crystallography for structural and functional studies of membrane proteins.
Journal of electron microscopy, 60(suppl 1):S149–59.

Gerchberg, R. W. and Saxton, W. O. (1969).
A Practical Algorithm for the Determination of Phase from Image and Diffraction Plane Pictures.
Optik, 2(352):237–246.

Gipson, B., Zeng, X., and Stahlberg, H. (2007a).
2dx_merge: Data management and merging for 2D crystal images.
Journal of Structural Biology, 160(3):375–384.

Gipson, B., Zeng, X., Zhang, Z. Y., and Stahlberg, H. (2007b).
2dx - User-friendly image processing for 2D crystals.
Journal of Structural Biology, 157(1):64–72.

Gipson, B. R., Masiel, D. J., Browning, N. D., Spence, J., Mitsuoka, K., and Stahlberg, H. (2011).
Automatic recovery of missing amplitudes and phases in tilt-limited electron crystallography of two-dimensional crystals.
Physical Review E, 84(1):011916.

Glaeser, R., McMullan, G., Faruqi, A., and Henderson, R. (2011).
Images of paraffin monolayer crystals with perfect contrast: Minimization of beam-induced specimen motion.
Ultramicroscopy, 111(2):90–100.

Gonen, T., Cheng, Y., Sliz, P., Hiroaki, Y., Fujiyoshi, Y., Harrison, S. C., and Walz, T. (2005).
Lipid-protein interactions in double-layered two-dimensional AQP0 crystals.
Nature, 438(7068):633–638.

Gordon, S. E., Varnum, M. D., and Zagotta, W. N. (1997).
Direct Interaction between Amino- and Carboxyl-Terminal Domains of Cyclic Nucleotide-Gated Channels.
Neuron, 19(2):431–441.

Grant, T. and Grigorieff, N. (2015).
Measuring the optimal exposure for single particle cryo-EM using a 2.6 Å reconstruction of rotavirus VP6.
eLife, 4:e06980.

Grigorieff, N. (2007).
FREALIGN: High-resolution refinement of single particle structures.
Journal of Structural Biology, 157(1):117–125.

Grigorieff, N. (2013).
Direct detection pays off for electron cryo-microscopy.
eLife, 2:e00573.

Grigorieff, N. (2016).
Frealign: An Exploratory Tool for Single-Particle Cryo-EM.
In *Methods in Enzymology*, volume 579, pages 191–226.

Gyobu, N., Tani, K., Hiroaki, Y., Kamegawa, A., Mitsuoka, K., and Fujiyoshi, Y. (2004).
Improved specimen preparation for cryo-electron microscopy using a symmetric carbon sandwich technique.
Journal of Structural Biology, 146(3):325–333.

Hagen, W. J., Wan, W., and Briggs, J. A. (2017).

Implementation of a cryo-electron tomography tilt-scheme optimized for high resolution subtomogram averaging.
Journal of Structural Biology, 197(2):191–198.

Harauz, G. and van Heel, M. (1986).
Exact filters for general geometry three dimensional reconstruction.

Henderson, R., Baldwin, J., Downing, K., Lepault, J., and Zemlin, F. (1986).
Structure of purple membrane from halobacterium halobium: recording, measurement and evaluation of electron micrographs at 3.5 Å resolution.
Ultramicroscopy, 19(2):147–178.

Henderson, R., Baldwin, J. M., Ceska, T. A., Zemlin, F., Beckmann, E., and Downing, K. H. (1990).
Model for the structure of bacteriorhodopsin based on high-resolution electron cryo-microscopy.
Journal of Molecular Biology, 213(4):899–929.

Henderson, R. and Unwin, P. (1975).
Three-dimensional model of purple membrane obtained by electron microscopy.
Nature, 257(5521):28–32.

Herman, G. T. and Frank, J., editors (2014).
Computational Methods for Three-Dimensional Microscopy Reconstruction.
Applied and Numerical Harmonic Analysis. Birkhäuser Basel.

Hirai, T., Murata, K., Mitsuoka, K., Kimura, Y., and Fujiyoshi, Y. (1999).
Trehalose embedding technique for high-resolution electron crystallography: application to structural study on bacteriorhoposin.
Journal of Electron Microscopy, 48(5):653–658.

Hite, R. K., Schenk, A. D., Li, Z., Cheng, Y., and Walz, T. (2010).
Collecting Electron Crystallographic Data of Two-Dimensional Protein Crystals.
In *Methods in Enzymology*, volume 481, pages 251–282.

Hite, R. K., Yuan, P., Li, Z., Hsuing, Y., Walz, T., and MacKinnon, R. (2015).
Cryo-electron microscopy structure of the Slo2.2 Na+-activated K+ channel.
Nature, 527(7577):198–203.

Hohn, M., Tang, G., Goodyear, G., Baldwin, P., Huang, Z., Penczek, P. A., Yang, C., Glaeser, R. M., Adams, P. D., and Ludtke, S. J. (2007).
SPARX, a new environment for Cryo-EM image processing.
Journal of Structural Biology, 157(1):47–55.

Huiskonen, J. T., Hepojoki, J., Laurinmäki, P., Vaheri, A., Lankinen, H., Butcher, S. J., and Grünewald, K. (2010).
Electron cryotomography of Tula hantavirus suggests a unique assembly paradigm for enveloped viruses.
Journal of virology, 84(10):4889–97.

Ilari, A. and Savino, C. (2008).
Protein Structure Determination by X-Ray Crystallography.
In *Methods in molecular biology (Clifton, N.J.)*, volume 452, pages 63–87.

Jaitly, N., Brubaker, M. A., Rubinstein, J. L., and Lilien, R. H. (2010).
A Bayesian method for 3D macromolecular structure inference using class average images from single particle electron microscopy.
Bioinformatics, 26(19):2406–2415.

Jap, B. K., Zulauf, M., Scheybani, T., Hefti, A., Baumeister, W., Aebi, U., and Engel, A. (1992).
2D crystallization: from art to science.
Ultramicroscopy, 46(1-4):45–84.

Jeckelmann, J. M., Harder, D., Mari, S. A., Meury, M., Ucurum, Z., Müller, D. J., Erni, B., and Fotiadis, D. (2011).
Structure and function of the glucose PTS transporter from Escherichia coli.
Journal of Structural Biology, 176(3):395–403.

Jones, T. A., Zou, J. ,., Cowan, S. W., and Kjeldgaard, M. (1991).
Improved methods for building protein models in electron density maps and the location of errors in these models.
Acta Crystallographica Section A, 47(2):110–119.

Kimanius, D., Forsberg, B. O., Scheres, S. H., and Lindahl, E. (2016).
Accelerated cryo-EM structure determination with parallelisation using GPUs in RELION-2.
eLife, 5:e18722.

Kimura, Y., Vassylyev, D. G., Miyazawa, A., Kidera, A., Matsushima, M., Mitsuoka, K., Murata, K., Hirai, T., and Fujiyoshi, Y. (1997).
Surface of bacteriorhodopsin revealed by high-resolution electron crystallography.
Nature, 389(6647):206–211.

Kowal, J., Chami, M., Baumgartner, P., Arheit, M., Chiu, P.-L. L., Rangl, M., Scheuring, S., Schröder, G. F., Nimigean, C. M., and Stahlberg, H. (2014).
Ligand-induced structural changes in the cyclic nucleotide-modulated potassium channel MloK1.
Nature communications, 5:3106.

Kremer, J. R., Mastronarde, D. N., and McIntosh, J. (1996).
Computer Visualization of Three-Dimensional Image Data Using IMOD.
Journal of Structural Biology, 116(1):71–76.

Kucukelbir, A., Sigworth, F. J., and Tagare, H. D. (2013).
Quantifying the local resolution of cryo-EM density maps.
Nature Methods, 11(1):63–65.

Kühlbrandt, W. (1992).
Two-dimensional crystallization of membrane proteins.
Quarterly reviews of biophysics, 25(1):1–49.

Kühlbrandt, W. (2003).
Two-Dimensional Crystallization of Membrane Proteins: A Practical Guide.
In *Membrane Protein Purification and Crystallization*, pages 253–284.

Kühlbrandt, W. (2014a).
Cryo-EM enters a new era.
eLife, 3:e03678.

Kühlbrandt, W. (2014b).
The Resolution Revolution.
Science, 343(6178):1443–1444.

Lander, G. C., Stagg, S. M., Voss, N. R., Cheng, A., Fellmann, D., Pulokas, J., Yoshioka, C., Irving, C., Mulder, A., Lau, P.-W., Lyumkis, D., Potter, C. S., and Carragher, B. (2009).
Appion: an integrated, database-driven pipeline to facilitate EM image processing.
Journal of structural biology, 166(1):95–102.

Lebeau, L., Lach, F., Vénien-Bryan, C., Renault, a., Dietrich, J., Jahn, T., Palmgren, M. G., Kühlbrandt, W., and Mioskowski, C. (2001).
Two-dimensional crystallization of a membrane protein on a detergent-resistant lipid monolayer.
Journal of molecular biology, 308(4):639–47.

Lee, C.-H. and MacKinnon, R. (2017).
Structures of the Human HCN1 Hyperpolarization-Activated Channel.
Cell, 168(1):111–120.e11.

Leith, A., Baxter, W., and Frank, J. (2012).
Use of SPIDER and SPIRE in image reconstruction.
In *International Tables for Crystallography*, chapter 19.8, pages 620–623.

Lepault, J. (1985).
Cryo-electron microscopy of helical particles TMV and T4 polyheads.
Journal of microscopy, 140(Pt 1):73–80.

Levy, D., Chami, M., and Rigaud, J. L. (2001).
Two-dimensional crystallization of membrane proteins: The lipid layer strategy.
FEBS Letters, 504(3):187–193.

Li, M., Zhou, X., Wang, S., Michailidis, I., Gong, Y., Su, D., Li, H., Li, X., and Yang, J. (2017).
Structure of a eukaryotic cyclic-nucleotide-gated channel.
Nature, 542(7639):60–65.

Li, X., Mooney, P., Zheng, S., Booth, C. R., Braunfeld, M. B., Gubbens, S., Agard, D. A., and Cheng, Y. (2013).
Electron counting and beam-induced motion correction enable near-atomic-resolution single-particle cryo-EM.
Nature methods, 10(6):584–590.

Li, X., Zheng, S., Agard, D. A., and Cheng, Y. (2015).
Asynchronous data acquisition and on-the-fly analysis of dose fractionated cryoEM images by UCSFImage.
Journal of Structural Biology, 192(2):174–178.

Liu, Z., Gutierrez-Vargas, C., Wei, J., Grassucci, R. A., Ramesh, M., Espina, N., Sun, M., Tutuncuoglu, B., Madison-Antenucci, S., Woolford, J. L., Tong, L., and Frank, J. (2016).
Structure and assembly model for the Trypanosoma cruzi 60S ribosomal subunit.
Proceedings of the National Academy of Sciences of the United States of America, 113(43):12174–12179.

Lolicato, M., Bucchi, A., Arrigoni, C., Zucca, S., Nardini, M., Schroeder, I., Simmons, K., Aquila, M., DiFrancesco, D., Bolognesi, M., Schwede, F., Kashin, D., Fishwick, C. W. G., Johnson, A. P., Thiel, G., and Moroni, A. (2014).
Cyclic dinucleotides bind the C-linker of HCN4 to control channel cAMP responsiveness.
Nature Chemical Biology, 10(6):457–462.

Long, S. B., Campbell, E. B., and MacKinnon, R. (2005a).
Crystal Structure of a Mammalian Voltage-Dependent Shaker Family K+ Channel.
Science, 309(5736).

Long, S. B., Campbell, E. B., and MacKinnon, R. (2005b).
Voltage Sensor of Kv1.2: Structural Basis of Electromechanical Coupling.
Science, 309(5736).

Long, S. B., Tao, X., Campbell, E. B., and MacKinnon, R. (2007).
Atomic structure of a voltage-dependent K+ channel in a lipid membrane-like environment.
Nature, 450(7168):376–382.

Lučić, V., Rigort, A., and Baumeister, W. (2013).
Cryo-electron tomography: The challenge of doing structural biology in situ.
Journal of Cell Biology, 202(3):407–419.

Ludtke, S. (2016).
Single-Particle Refinement and Variability Analysis in EMAN2.1.
In *Methods in Enzymology*, volume 579, pages 159–189.

Ludtke, S., Tang, G., and Woolford, D. (2009).
3-D TEM Reconstructions with EMAN2.
Microscopy and Microanalysis, 15(S2):1524–1525.

Lyumkis, D., Brilot, A. F., Theobald, D. L., and Grigorieff, N. (2013).
Likelihood-based classification of cryo-EM images using FREALIGN.
Journal of Structural Biology, 183(3):377–388.

Mallick, S. P., Carragher, B., Potter, C. S., and Kriegman, D. J. (2005).
ACE: Automated CTF estimation.
Ultramicroscopy, 104(1):8–29.

Marchesini, S., He, H., Chapman, H. N., Hau-Riege, S. P., Noy, a., Howells, M. R., Weierstall, U., and Spence, J. C. H. (2003).
X-ray image reconstruction from a diffraction pattern alone.
Physical Review B, 68:5.

Mariani, V., Schenk, A. D., Philippsen, A., and Engel, A. (2011).
Simulation and correction of electron images of tilted planar weak-phase samples.
Journal of Structural Biology, 174(2):259–268.

Marsh, D. (1996).
Lateral pressure in membranes.
Biochimica et Biophysica Acta - Reviews on Biomembranes, 1286(3):183–223.

Marsh, D. (2007).
Lateral pressure profile, spontaneous curvature frustration, and the incorporation and conformation of proteins in membranes.
Biophysical journal, 93(11):3884–3899.

Mastronarde, D. N. (2005).

Automated electron microscope tomography using robust prediction of specimen movements.
Journal of Structural Biology, 152(1):36–51.

McLeod, R. A., Kowal, J., Ringler, P., and Stahlberg, H. (2016).
Robust image alignment for cryogenic transmission electron microscopy.
Journal of Structural Biology, In Press.

McRee, D. E. (1999).
XtalView/Xfit–A versatile program for manipulating atomic coordinates and electron density.
Journal of structural biology, 125(2-3):156–65.

Merk, A., Bartesaghi, A., Banerjee, S., Falconieri, V., Rao, P., Davis, M. I., Pragani, R., Boxer, M. B., Earl, L., Milne, J., and Subramaniam, S. (2016).
Breaking Cryo-EM Resolution Barriers to Facilitate Drug Discovery.
Cell, 165(7):1698–1707.

Michalakis, S., Reisert, J., Geiger, H., Wetzel, C., Zong, X., Bradley, J., Spehr, M., Hüttl, S., Gerstner, A., Pfeifer, A., Hatt, H., Yau, K.-W., and Biel, M. (2006).
Loss of CNGB1 protein leads to olfactory dysfunction and subciliary cyclic nucleotide-gated channel trapping.
The Journal of biological chemistry, 281(46):35156–66.

Milazzo, A.-C., Cheng, A., Moeller, A., Lyumkis, D., Jacovetty, E., Polukas, J., Ellisman, M. H., Xuong, N.-H., Carragher, B., and Potter, C. S. (2011).
Initial evaluation of a direct detection device detector for single particle cryo-electron microscopy.
Journal of Structural Biology, 176(3):404–408.

Mindell, J. A. and Grigorieff, N. (2003).
Accurate determination of local defocus and specimen tilt in electron microscopy.
Journal of Structural Biology, 142(3):334–347.

Mitsuoka, K., Hirai, T., Murata, K., Miyazawa, A., Kidera, A., Kimura, Y., and Fujiyoshi, Y. (1999).
The structure of bacteriorhodopsin at 3.0 Å resolution based on electron crystallography: implication of the charge distribution.
Journal of molecular biology, 286(3):861–82.

Miyazawa, A., Fujiyoshi, Y., and Unwin, N. (2003).
Structure and gating mechanism of the acetylcholine receptor pore.
Nature, 423(6943):949–955.

Murata, K., Mitsuoka, K., Hirai, T., Walz, T., Agre, P., Heymann, J. B., Engel, A., and Fujiyoshi, Y. (2000).
Structural determinants of water permeation through aquaporin-1.
Nature, 407(6804):599–605.

Nache, V., Wongsamitkul, N., Kusch, J., Zimmer, T., Schwede, F., and Benndorf, K. (2016).
Deciphering the function of the CNGB1b subunit in olfactory CNG channels.
Scientific reports, 6:29378.

Nicastro, D., Schwartz, C., Pierson, J., Gaudette, R., Porter, M. E., and McIntosh, J. R. (2006).
The Molecular Architecture of Axonemes Revealed by Cryoelectron Tomography.
Science, 313(5789).

Nickell, S., Förster, F., Linaroudis, A., Net, W. D., Beck, F., Hegerl, R., Baumeister, W., and Plitzko, J. M. (2005).
TOM software toolbox: acquisition and analysis for electron tomography.
Journal of Structural Biology, 149(3):227–234.

Nimigean, C. M., Shane, T., and Miller, C. (2004).
A cyclic nucleotide modulated prokaryotic K+ channel.
The Journal of general physiology, 124(3):203–10.

Noble, A. J. and Stagg, S. M. (2015).
Automated batch fiducial-less tilt-series alignment in Appion using Protomo.
Journal of Structural Biology, 192(2):270–278.

Oesterhelt, D. and Stoeckenius, W. (1974).
Isolation of the cell membrane of Halobacterium halobium and its fractionation into red and purple membrane.
Methods in Enzymology, 31(C):667–678.

Patwardhan, A., Carazo, J.-M., Carragher, B., Henderson, R., Heymann, J. B., Hill, E., Jensen, G. J., Lagerstedt, I., Lawson, C. L., Ludtke, S. J., Mastronarde, D., Moore, W. J., Roseman, A., Rosenthal, P., Sorzano, C.-O. S., Sanz-Garcia, E., Scheres, S. H. W., Subramaniam, S., Westbrook, J., Winn, M., Swedlow, J. R., and Kleywegt, G. J. (2012).
Data management challenges in three-dimensional EM.
Nature structural & molecular biology, 19(12):1203–1207.

Payandeh, J., Scheuer, T., Zheng, N., and Catterall, W. A. (2011).
The crystal structure of a voltage-gated sodium channel.
Nature, 475(7356):353–358.

Philippsen, A., Engel, H.-A., and Engel, A. (2007).
The contrast-imaging function for tilted specimens.
Ultramicroscopy, 107(2):202–212.

Punjani, A., Rubinstein, J. L., Fleet, D. J., and Brubaker, M. A. (2017).
cryoSPARC: algorithms for rapid unsupervised cryo-EM structure determination.
Nature Methods, 14(3):290–296.

Quinn, C. M. and Polenova, T. (2017).
Structural biology of supramolecular assemblies by magic-angle spinning NMR spectroscopy.
Quarterly Reviews of Biophysics, 50:e1.

Rangl, M., Miyagi, A., Kowal, J., Stahlberg, H., Nimigean, C. M., and Scheuring, S. (2016).
Real-time visualization of conformational changes within single MloK1 cyclic nucleotide-modulated channels.
Nature Communications, 7:12789.

Rawson, S., Iadanza, M., Ranson, N., and Muench, S. (2016).
Methods to account for movement and flexibility in cryo-EM data processing.
Methods, 100:35–41.

Rémigy, H. W., Caujolle-Bert, D., Suda, K., Schenk, A., Chami, M., and Engel, A. (2003).
Membrane protein reconstitution and crystallization by controlled dilution.
FEBS Letters, 555(1):160–169.

Rigaud, J.-L., Mosser, G., Lacapere, J. J., Olofsson, A., Lévy, D., and Ranck, J.-L. (1997).
Bio-Beads: an efficient strategy for two-dimensional crystallization of membrane proteins.
Journal of structural biology, 118(3):226–235.

Robert, X. and Gouet, P. (2014).
Deciphering key features in protein structures with the new ENDscript server.
Nucleic acids research, 42(Web Server issue):W320–4.

Rose, H. H. (2008).
Optics of high-performance electron microscopes.
Science and technology of advanced materials, 9(1):014107.

Rosenbusch, J. P. (2001).
Stability of membrane proteins: relevance for the selection of appropriate methods for high-resolution structure determinations.
Journal of structural biology, 136(2):144–57.

Rossmann, M. G., Battisti, A. J., and Plevka, P. (2011).

Future prospects.
In *Advances in Protein Chemistry and Structural Biology*, volume 82, pages 101–121.

Rubinstein, J. L. and Brubaker, M. A. (2015).
Alignment of cryo-EM movies of individual particles by optimization of image translations.
Journal of Structural Biology, 192(2):188–195.

Ruskin, R. S., Yu, Z., and Grigorieff, N. (2013).
Quantitative characterization of electron detectors for transmission electron microscopy.
Journal of Structural Biology, 184(3):385–393.

Saldin, D. K., Harder, R. J., Shneerson, V. L., and Moritz, W. (2001).
Phase retrieval methods for surface x-ray diffraction.
Jounal of Physics: Condensed Matter, 13:10689–10707.

Šali, A. and Blundell, T. L. (1993).
Comparative Protein Modelling by Satisfaction of Spatial Restraints.
Journal of Molecular Biology, 234(3):779–815.

Schenk, A. D., Philippsen, A., Engel, A., and Walz, T. (2013).
A pipeline for comprehensive and automated processing of electron diffraction data in IPLT.
Journal of Structural Biology, 182(2):173–185.

Schenk, A. D., Werten, P. J. L., Scheuring, S., De Groot, B. L., Müller, S. A., Stahlberg, H., Philippsen, A., and Engel, A. (2005).
The 4.5 Å structure of human AQP2.
Journal of Molecular Biology, 350(2):278–289.

Scherer, S., Arheit, M., Kowal, J., Zeng, X., and Stahlberg, H. (2014a).
Single particle 3D reconstruction for 2D crystal images of membrane proteins.
Journal of Structural Biology, 185(3):267–277.

Scherer, S., Kowal, J., Chami, M., Dandey, V., Arheit, M., Ringler, P., and Stahlberg, H. (2014b).
2dx_automator: Implementation of a semiautomatic high-throughput high-resolution cryo-electron crystallography pipeline.
Journal of Structural Biology, 186(2):302–307.

Scheres, S. H. (2012).
RELION: Implementation of a Bayesian approach to cryo-EM structure determination.
Journal of Structural Biology, 180(3):519–530.

Scheres, S. H. (2014).
Beam-induced motion correction for sub-megadalton cryo-EM particles.
eLife, 3:e03665.

Scheres, S. H., Valle, M., Nuñez, R., Sorzano, C. O., Marabini, R., Herman, G. T., and Carazo, J.-M. (2005).
Maximum-likelihood Multi-reference Refinement for Electron Microscopy Images.
Journal of Molecular Biology, 348(1):139–149.

Schmidt-Krey, I. (2007).
Electron crystallography of membrane proteins: Two-dimensional crystallization and screening by electron microscopy.
Methods, 41(4):417–426.

Schmidt-Krey, I. and Rubinstein, J. L. (2011).
Electron cryomicroscopy of membrane proteins: Specimen preparation for two-dimensional crystals and single particles.
Micron, 42(2):107–116.

Schultz, P., Crucifix, C., and Lebeau, L. (2009).
Two-Dimensional Crystallisation of Soluble Protein Complexes.
In *Methods in Molecular Biology*, pages 353–367.

Schur, F. K. M., Obr, M., Hagen, W. J. H., Wan, W., Jakobi, A. J., Kirkpatrick, J. M., Sachse, C., Kräusslich, H.-G., and Briggs, J. A. G. (2016).
An atomic model of HIV-1 capsid-SP1 reveals structures regulating assembly and maturation.
Science, 353(6298):506–8.

Sievers, F., Wilm, A., Dineen, D., Gibson, T. J., Karplus, K., Li, W., Lopez, R., McWilliam, H., Remmert, M., Söding, J., Thompson, J. D., and Higgins, D. G. (2011).
Fast, scalable generation of high-quality protein multiple sequence alignments using Clustal Omega.
Molecular systems biology, 7:539.

Signorell, G. A., Kaufmann, T. C., Kukulski, W., Engel, A., and Rémigy, H. W. (2007).
Controlled 2D crystallization of membrane proteins using methyl-β-cyclodextrin.
Journal of Structural Biology, 157(2):321–328.

Sigworth, F. (1998).
A Maximum-Likelihood Approach to Single-Particle Image Refinement.
Journal of Structural Biology, 122(3):328–339.

Sigworth, F. J. (2016).
Principles of cryo-EM single-particle image processing.
Microscopy, 65(1):57–67.

Sim, G. A. (1959).
The distribution of phase angles for structures containing heavy atoms. II. A modification of the normal heavy-atom method for non-centrosymmetrical structures.
Acta Crystallographica, 12(10):813–815.

Sim, G. A. (1960).
A note on the heavy-atom method.
Acta Crystallographica, 13(6):511–512.

Smyth, M. S. and Martin, J. H. (2000).
X ray crystallography.
Molecular pathology, 53(1):8–14.

Sonoda, Y., Newstead, S., Hu, N. J., Alguel, Y., Nji, E., Beis, K., Yashiro, S., Lee, C., Leung, J., Cameron, A. D., Byrne, B., Iwata, S., and Drew, D. (2011).
Benchmarking membrane protein detergent stability for improving throughput of high-resolution x-ray structures.
Structure, 19(1):17–25.

Stahlberg, H., Biyani, N., and Engel, A. (2015).
3D reconstruction of two-dimensional crystals.
Archives of Biochemistry and Biophysics, 581:68–77.

Stokes, D. L., Rice, W. J., Hu, M., Kim, C., and Ubarretxena-Belandia, I. (2010).
Two-Dimensional Crystallization of Integral Membrane Proteins for Electron Crystallography.
In *Methods in Molecular Biology*, pages 187–205.

Subramaniam, S. and Henderson, R. (2000).
Molecular mechanism of vectorial proton translocation by bacteriorhodopsin.
Nature, 406(6796):653–657.

Suloway, C., Pulokas, J., Fellmann, D., Cheng, A., Guerra, F., Quispe, J., Stagg, S., Potter, C. S., and Carragher, B. (2005).
Automated molecular microscopy: The new Leginon system.
Journal of Structural Biology, 151(1):41–60.

Tang, G., Peng, L., Baldwin, P. R., Mann, D. S., Jiang, W., Rees, I., and Ludtke, S. J. (2007).
EMAN2: An extensible image processing suite for electron microscopy.
Journal of Structural Biology, 157(1):38–46.

Tani, K., Mitsuma, T., Hiroaki, Y., Kamegawa, A., Nishikawa, K., Tanimura, Y., and Fujiyoshi, Y. (2009).
Mechanism of Aquaporin-4's Fast and Highly Selective Water Conduction and Proton Exclusion.

Journal of Molecular Biology, 389(4):694–706.

Terwilliger, T. C., Stuart, D., and Yokoyama, S. (2009).
Lessons from Structural Genomics.
Annual Review of Biophysics, 38(1):371–383.

Thon, F. (1966).
Zur Defokussierungsabhängigkeit des Phasen- kontrastes bei der elektronenmikroskopischen Abbildung.
Z . Naturforsdig, 21a:476–478.

Unwin, N. (2005).
Refined structure of the nicotinic acetylcholine receptor at 4 Å resolution.
Journal of Molecular Biology, 346(4):967–989.

Unwin, N. and Fujiyoshi, Y. (2012).
Gating movement of acetylcholine receptor caught by plunge-freezing.
Journal of Molecular Biology, 422(5):617–634.

van Heel, M., Portugal, R., Rohou, A., Linnemayr, C., Bebeacua, C., Schmidt, R., Grant, T., and Schatz, M. (2012).
Four-dimensional cryo-electron microscopy at quasi-atomic resolution: IMAGIC 4D.
pages 624–628.

Veesler, D., Campbell, M. G., Cheng, A., Fu, C.-y., Murez, Z., Johnson, J. E., Potter, C. S., and Carragher, B. (2013).
Maximizing the potential of electron cryomicroscopy data collected using direct detectors.
Journal of Structural Biology, 184(2):193–202.

Vink, M., Derr, K., Love, J., Stokes, D. L., and Ubarretxena-Belandia, I. (2007).
A high-throughput strategy to screen 2D crystallization trials of membrane proteins.
Journal of Structural Biology, 160(3):295–304.

Wade, R. (1992).
A brief look at imaging and contrast transfer.
Ultramicroscopy, 46(1-4):145–156.

Wang, H. (2015).
Cryo-electron microscopy for structural biology: current status and future perspectives.
Science China Life Sciences, 58(8):750–756.

Wedberg, T. C. and Stamnes, J. J. (1999).
Comparison of phase retrieval methods for optical diffraction tomography.
Pure and Applied Optics: Journal of the European Optical Society Part A, 4:39–54.

Whicher, J. R. and MacKinnon, R. (2016).
Structure of the voltage-gated K+ channel Eag1 reveals an alternative voltage sensing mechanism.
Science, 353(6300):664–669.

Yan, A., Wu, X., and Liu, H. (2011).
Robustness of phase retrieval methods in x-ray phase contrast imaging: A comparison.
Medical Physics, 38(9):5073.

Yu, G., Li, K., Huang, P., Jiang, X., and Jiang, W. (2016).
Antibody-Based Affinity Cryoelectron Microscopy at 2.6-Å Resolution.
Structure, 24(11):1984–1990.

Zeng, X., Gipson, B., Zheng, Z. Y., Renault, L., and Stahlberg, H. (2007).
Automatic lattice determination for two-dimensional crystal images.
Journal of Structural Biology, 160(3):353–361.

Zhang, K. (2016).
Gctf: Real-time CTF determination and correction.
Journal of Structural Biology, 193(1):1–12.

Zheng, S., Palovcak, E., Armache, J.-P., Cheng, Y., and Agard, D. (2016).
Anisotropic Correction of Beam-induced Motion for Improved Single-particle Electron Cryomicroscopy.

Zheng, S. Q., Keszthelyi, B., Branlund, E., Lyle, J. M., Braunfeld, M. B., Sedat, J. W., and Agard, D. A. (2007).
UCSF tomography: An integrated software suite for real-time electron microscopic tomographic data collection, alignment, and reconstruction.
Journal of Structural Biology, 157(1):138–147.